ESTABLISHING A HIGH-ACCURACY, DUAL-WAVELENGTH MUELLER PULSED LIDAR TESTBED

by

Nathaniel James Field

A dissertation submitted in partial fulfillment
of the requirements for the degree

of

Doctor of Philosophy

in

Electrical Engineering

MONTANA STATE UNIVERSITY
Bozeman, Montana

August 2025

©COPYRIGHT

by

Nathaniel James Field

2025

All Rights Reserved

DEDICATION

To my big crazy family, who gave me the audacity to be as confident as I am and who are always there to loudly support me (even when I'd rather they weren't).

To my incredible and far-flung network of forever friends, who are willing to put up with my own brand of chaos and keep me grounded.

To my mentors and colleagues, who are almost always ready to dive in and help solve a problem that's got me stuck, and who inspire me to stay curious yet practical.

ACKNOWLEDGEMENTS

This material (AFRL-2025-1717) is based on research sponsored by Air Force Research Lab under agreement number FA8650-21-1-1176. The U.S. Government is authorized to reproduce and distribute reprints for Governmental purposes notwithstanding any copyright notation therein. The views and conclusions contained herein are those of the authors and should not be interpreted as necessarily representing the official policies or endorsements, either expressed or implied, of Air Force Research Lab or the U.S. Government.

VITA

Nathaniel James Field was born in Bozeman, MT in 1994 to Clint and Traci Field. Raised just next door in Belgrade, Nate was lucky to have many experiences with science and engineering concepts at Montana State University beginning as early as elementary school. He graduated from MSU with a BS in Electrical Engineering in 2016, having had the great benefit of undergraduate research experience working with Dr. Wataru Nakagawa. He then took a job with L3Harris Technologies as an optical and photonics test engineer. It was exciting to work on weather satellites in both Indiana and New York, but ultimately Montana called him home.

Wanting primarily to teach engineering, he decided to pursue his MS in Optics and PhD in Electrical Engineering back at MSU in fall 2018. He received his MS in Optics in spring 2020, based primarily on research performed during a summer senior internship with Lockheed Martin Coherent Technologies. During his graduate school program, he had the great benefit of engaging in the very same outreach that he had enjoyed as a child. Nate hopes he is able to continue building on the decades of symbiotic relationships between the Gallatin valley at-large and its thriving optics and photonics community.

TABLE OF CONTENTS

1. INTRODUCTION 1

1.1 Literature Review 1
1.1.1 Polarimetric Remote Sensing 1
1.1.2 Polarimetric BRDF 4
1.2 Objectives 7
1.2.1 Design & Build Optimal PSG & PSA systems 7
1.2.2 Develop (Near-)Monostatic P-BRDF Measurement Procedures 7
1.2.3 Design & Build Mueller Lidar (DMPL) Testbed 8
1.2.4 Calibrate & Validate DMPL Testbed 8

2. SIMPLE NEAR-MONOSTATIC MUELLER POLARIMETER 9

2.1 Contribution of Author and Co-Author 9
2.2 Manuscript Information 10
2.3 Abstract 11
2.4 Introduction 11
2.5 Background 12
2.6 Instrument Design 14
2.6.1 Example Design 14
2.6.2 System Analysis 16
2.7 Operating Procedure and Data Analysis 19
2.7.1 Optomechanical Alignment 19
2.7.2 Control and Analysis Software 21
2.7.3 Data Collection Procedure 21
2.7.4 Data Structure and Analysis 23
2.8 Example Material Measurements 25
2.9 Discussion 26

3. REFLECTANCE RELATIVE CALIBRATION 31

3.1 Constraining the BRDF 31
3.1.1 Geometric Considerations 33
3.1.2 Lambertian Reference Surfaces 35
3.1.3 Reflectance Relative Calibration Function, K 35
3.2 Procedure 36
3.2.1 Calibration Procedure Summary 37
3.3 Experimental Validation 38
3.3.1 Alternate Reflectance Normalization Procedure 38
3.3.2 Data Collection 41

TABLE OF CONTENTS – CONTINUED

3.3.3 Data Comparisons 42
3.4 Discussion 45

4. NON-RANGING MATERIAL P-MBRDF CHARACTERIZATION 47

4.1 Methods 47
4.2 Lambertian References 47
4.3 Urban Materials 54

5. DICHROIC MUELLER PULSED LIDAR (DMPL) TESTBED 58

5.1 Contribution of Author and Co-Author 58
5.2 Manuscript Information 59
5.3 Abstract 60
5.4 Introduction 60
5.5 System Design 62
5.5.1 Key Components 63
5.5.2 Polarimetric Accuracy 64
5.5.3 Automation and Measurement Rate 67
5.5.4 Variable Scene Distances 68
5.6 Calibration & Validation 69
5.6.1 Reflectance Calibration 69
5.6.2 Ranging Validation 72
5.6.3 Polarimetric Validation 74
5.6.4 Global Rotation Tolerance 82
5.7 Discussion & Conclusions 82

6. CONCLUSION 84

6.1 Summary of Research Objectives & Achievements 84
6.2 Contributions to the Field 85
6.3 Implications & Applications 85

REFERENCES CITED 87

APPENDICES 93

APPENDIX A : ANALYSIS SCRIPT 94
APPENDIX B : CONTROL SOFTWARE ARCHITECTURE 104
APPENDIX C : PHOTOMETRIC CALCULATIONS 111
APPENDIX D : DMPL OPERATING PROCEDURE 115

LIST OF TABLES

Table Page

1. Table 1 Developed System Parts and Approximate Costs..... 16
2. Table 2 Developed System Specifications 18

LIST OF FIGURES

Figure Page

1. Figure 1 Mueller P-mBRDF of a red clay brick taken with an earlier iteration of the DMPL with a continuous laser source and functioning as a simple polarimeter. 6

2. Figure 2 Overhead image of the simple polarimeter, with the transmitter optics labelled in red and the receiver optics labelled in blue. This figure is a partial reproduction of a figure in [1]. 15

3. Figure 3 Overhead diagram depicting the geometric separation angle, the surface-normal 0° reference setup, and the general orientation of positive and negative viewing/illumination angles. 20

4. Figure 4 The red clay brick sample on a horizontal rotation stage. Two set screws make it easy to return the brick to the same position repeatably, and to more accurately determine the invidence/viewing angle, θ_v, relative to the polarimeter. This figure is a partial reproduction of a figure in [1]. 28

5. Figure 5 An image of the sample brick surface about the measurement location (left) and the resulting P-mBRDF measurement (right). 29

6. Figure 6 An image of the sample tar-fiberglass shingle surface about the measurement location (left) and the resulting P-mBRDF measurement (right). 30

7. Figure 7 A representation of a bistatic active remote sensing system. The FOV solid angle, Ω_{FOV}, is represented by the blue shaded region, and the solid angle subtended by the sample's projected illuminated area, Ω_{ill}, is represented by the red shaded region. Also of note, for bistatic systems with large separation angles, θ_Δ, should place their transmitter or receiver normal to the panel. 34

LIST OF FIGURES – CONTINUED

Figure Page

8. Figure 8 Overview of the Lambertian reference calibration method applied to a monostatic lidar system (or other active remote sensing system). The calibrating measurement (top) of the Lambertian reference with known reflectance, ρ_{cc}, is performed with the reference panel at normal incidence to the lidar optical path. The sample measurements (bottom) can then be taken at any measured incidence angle. The measured V_{ref} value would be used with Eqs. 34 and 36 in this case, turning the measured signal voltage, V_{sig}, into a BRDF value, f_r^m, at the given viewing angle, $\theta_v = \theta_i$. 39

9. Figure 9 A plot of $f_r(\theta_v)$ for a 99% Spectralon® panel. The trend away from an ideal Lambertian response at increasing θ_v is as expected, and the reference method produced normalized results closer to the expected reflectance near normal θ_v and within the tolerance of the normalized results. 42

10. Figure 10 A plot of $f_r(\theta_v)$ for a 10% Spectralon® panel. At these lower ρ_{cc} values, the BRDF actually increases at larger θ_v, perhaps due to an increased prevalence of single-scattering events [2]. 43

11. Figure 11 The simple near-monostatic Mueller polarimeter. The overhead view is labelled with system components and the red clay brick sample is shown on the sample rotation stage used to control θ_v. 48

12. Figure 12 The P-mBRDF measurement geometry, not to scale. A 0° incidence/viewing angle is defined when the surface normal of the target is 2° from the optical paths of both the transmitter and receiver. Rotating counterclockwise (surface normal toward the receiver) is the negative angular direction, while rotating clockwise (surface normal toward the transmitter) is the positive angular direction. 48

13. Figure 13 An image of the sample Spectralon surface (left) and the resulting P-mBRDF measurement over a fine scan of θ (right). 49

14. Figure 14 Average RMS error of measurements as compared to ideal Lambertian mBRDF by reference nominal reflectance. 50

LIST OF FIGURES – CONTINUED

Figure Page

15. Figure 15 Plot of Spectralon reference mBRDF returns as compared to the ideal for a Lambertian reflector of the reference panel's nominal reflectance. These data are calculated using a relative reflectance calibration as described in Ch. 3. 51

16. Figure 16 A second, broader set of measurements of a 99% Spectralon reference, which can be compared to the former measurement shown in Fig. 13. The blue line shows positive θ values while the red line shows negative values. 51

17. Figure 17 P-mBRDF measurements of a 50% Spectralon reference. The blue line shows positive θ values while the red line shows negative values. 52

18. Figure 18 P-mBRDF measurements of a 30% Spectralon reference. The blue line shows positive θ values while the red line shows negative values. 52

19. Figure 19 P-mBRDF measurements of a 10% Spectralon reference. The blue line shows positive θ values while the red line shows negative values. 53

20. Figure 20 The polarizance, as represented by the magnitude of m_{01} or m_{10}, as a function of nominal panel reflectance. 53

21. Figure 21 An image of the sample brick surface about the measurement location (left) and the resulting P-mBRDF measurement (right). 54

22. Figure 22 An image of the sample plain, unpainted sheetrock surface (left) and the resulting P-mBRDF measurement (right) 56

23. Figure 23 An image of the sample milled steel surface (left) and the resulting P-mBRDF measurement (right). 56

24. Figure 24 An image of the sample tar roofing shingle which includes fiberglass insulation (left) and the resulting P-mBRDF measurement (right). 57

LIST OF FIGURES – CONTINUED

Figure Page

25. Figure 25 The DMPL transmitter (red) and receiver (blue), mounted on an optical breadboard. This assembly weighs about 16 kg, sufficiently light and rigid to be mounted on a motorized pan-tilt mount with a full range of motion. 63

26. Figure 26 A look underneath the receiver, showing the locked rotation stage and the retractable legs used to level and better stabilize the platform. 69

27. Figure 27 Plot of K_{532} as a function of θ_i, for a handful of T_{ND} values, as well as the fitted inverse cosine curves extending to values beyond 0 to ψ. These values are for our laser tunnel setup where $\psi \approx 0.65°$. 71

28. Figure 28 Plot of Mueller coefficients in the 532-nm channel as a function of range for two cardboard samples at a range of 8.69 m and 13.1 m. Note that the Mueller coefficients are normalized to m_{00}, and in place of m_{00} an arbitrary signal strength is plotted instead. Range values for which the signal is at or below the noise threshold are masked out of the plots. All plots share the same x-axis scale and limits, and only the upper-left plot has different y-axis scale and limits. 73

29. Figure 29 Plot of Mueller coefficients for a 99% reflective Spectralon® sample from -60° to 60° in steps of 5°. Note that the very small values of the coefficients are 0 to within the system error. No data are shown for range-angle combinations where there was no detectable return signal above the noise. Each plot shares the same x- and y-axis scale and limits. 75

LIST OF FIGURES – CONTINUED

Figure Page

30. Figure 30 Plot of Mueller coefficients in the 532-nm channel as a function of range for three partially illuminated samples: a plant at 8.23 m, cardboard at 9.75 m, and aluminum at 11.89 m. The peak signal for each sample is shown with a vertical dotted line, and the unambiguous range resolution around those peaks are denoted with colored vertical lines: green (plant), blue (cardboard), and red (aluminum). Note that the Mueller coefficients are normalized to m_{00}, and in place of m_{00} an arbitrary signal strength is plotted. All plots share the same x-axis scale and limits, and only the upper-left plot has different y-axis scale and limits. 76

31. Figure 31 Plot of Mueller coefficients in the 1064-nm channel as a function of range for three partially illuminated samples: a plant at 8.23 m, cardboard at 9.75 m, and aluminum at 11.89 m. The peak signal for each sample is shown with a vertical dotted line, and the unambiguous range resolution around those peaks are denoted with colored vertical lines: green (plant), blue (cardboard), and red (aluminum). Note that the Mueller coefficients are normalized to m_{00}, and in place of m_{00} an arbitrary signal strength is plotted. All plots share the same x-axis scale and limits, and only the upper-left plot has different y-axis scale and limits. 77

32. Figure 32 The front panel for the DMPL control software. The default number of average shots is 12. Other default channel and sampling rate options are set and not regularly changed. 105

33. Figure 33 The first third of the DMPL control software block diagram. This section initializes the rotation controllers and the digitizer. 106

34. Figure 34 The middle third of the DMPL control software block diagram. This section loops through the rotation values for each of the PSG and PSA states and captures the lidar returns for each state combination. If the rotation mounts need to be homed, that is performed in this section as well. 107

LIST OF FIGURES – CONTINUED

Figure Page

35. Figure 35 The last third of the DMPL control software block diagram. This section generates the save files and saves them to the selected file path. It also releases control of the rotation mounts to avoid issues in continuous runs. 108

36. Figure 36 The front panel for the lidar shot capture code, visually modified from the original GaGe capture software. 109

37. Figure 37 The actual capture procedure from the GaGe capture software used to collect the lidar returns. This section of the code was modified significantly to change the structure of the outputs to be more usable in the primary DMPL control software. 110

ABSTRACT

Polarization enhancement of remote sensing systems can improve sample discrimination and even resolution in ranged or imaged scenes. Assistive and autonomous machine vision systems benefit from the added data dimension of polarization in both passive and active remote sensor systems. While optimal transmit and receive polarization states have been discovered for atmospheric and oceanographic measurement scenarios, such optimal states have not yet been solidified for machine vision scenarios involving opaque samples in complex scenes, particularly when using monostatic or near-monostatic systems like lidars. This is, in part, due to a knowledge gap for material polarized response characterization, and the complex nature of full polarimetry needed to perform initial characterizing measurements before reaching optimal states. This work has four primary objectives: (1) to design a high-accuracy and precision polarimeter, (2) to develop a procedure for characterizing the monostatic polarized response of materials which is publicly available and easy to implement, (3) to develop simple calibration methods to establish accuracy and precision metrics, and (4) to pull the prior objectives together along with a pulsed lidar design to generate a dichroic Mueller pulsed lidar testbed. Drawing on literature and applying optical and mechanical tolerances, we developed an optimal polarimeter, then described the design, build, and operating procedure of that polarimeter for near-monostatic and monostatic measurements in a publication for easy replication by other groups with interest in the outcomes. Generalized calibration procedures are presented in this dissertation for public consumption, as well as the design, calibration, and validation of the primary instrument testbed. The final lidar testbed has mean Mueller coefficient errors of less than 1%, allowing it to operate as a characterization and validation instrument for the pursuit of optimal polarization states for enhanced machine vision scenarios.

CHAPTER ONE

INTRODUCTION

As remote sensing systems evolve, industry and military have adopted machine vision to assist in the operation of systems or even to automate systems entirely. Machine vision can exploit polarimetric optical sensing as an added dimension beyond intensity and color for applications in military sensing, automated vehicles, and atmospheric monitoring [3–8].

To assess the effects of polarization at common visible and near-infrared wavelengths (532-nm and 1064-nm, respectively), we have designed, built, and validated a dichroic Mueller pulsed lidar (DMPL). The DMPL is a lidar testbed, aimed at full-polarimetric characterization of samples at two wavelengths simultaneously, and for operation outdoors in both summer and winter conditions.

1.1 Literature Review

1.1.1 Polarimetric Remote Sensing

Polarimetric remote sensing has been used in a wide variety of applications with both passive and active systems [3, 9]. Passive remote sensor systems benefit from low power consumption due to a lack of an illumination source, but they also require significant knowledge about the background and circumstances of the image. For polarimetry, we need to know the initial polarization of light interacting with a sample for consistent measurements. While the polarization of background illumination, such as direct solar illumination or diffuse skylight illumination, can be modeled with reasonable accuracy for certain spectral bands under set conditions [10], reliance on modeled background polarization

does not provide for particularly robust sensor applications. Moreover, natural illumination sources are almost entirely randomly polarized (or "unpolarized"), which constrains the sensor to detection of only those properties of a scene which cause polarization for unpolarized incident light. Therefore, we focus our polarimetric research on active remote sensing systems – systems for which a controlled transmitter, such as a laser, illuminates the scene which the receiver or multiple receivers view. These active systems can generate a wider variety of polarized illumination states to more fully characterize a sample or scene.

One type of active remote sensing system – dual-polarization light detection and ranging (lidar) – transmits a single polarization state (typically linearly polarized) and has receivers for that state and the orthogonal state. To show the variety of dual-polarization-enhanced measurement scenarios, a small selection of applications include: detecting honeybees in flight [11], detecting vehicles concealed by foliage and other vegetation [12], detecting the thermodynamic phase of wave-clouds [13], and airborne detection of invasive lake trout below a lake's surface [14, 15]. The seminal work in dual-polarization actually began with noting changes in depolarization of clouds and melting snowflakes when observed by active remote sensing systems [16, 17]. This led to further studies on depolarization effects in the atmosphere, especially concerning ice crystals and cloud make-up [18, 19]. A push from the previous linear-only polarimetry to full Stokes measurements led to the conclusion that dual-polarization measurements were the most efficient means of characterizing atmospheric effects [20]. The standard notation and theory of dual-polarization lidar operation was published in 2008 [21] and complete theoretical explanation of polarimetric lidar derived from Stokes vectors and Mueller matrices was published four years later [22].

However, shifting our interest from atmospheric remote sensing to remote sensing of solid objects within the atmosphere, the question remains open as to the most effective transmit and receive states for polarization-enhanced active remote sensors. Stokes vectors, $\vec{S}$, and Mueller matrices, $\mathbf{M}$, classically represent electromagnetic (EM) waves' complete

polarization state and the response of the EM wave to a material, respectively. The general forms of the Mueller matrix and Stokes vector as used herein are presented in Eq. 1.

$$\vec{S_{out}} = \begin{bmatrix} S_{0,out} \\ S_{1,out} \\ S_{2,out} \\ S_{3,out} \end{bmatrix} = \mathbf{M}\vec{S_{in}} = \begin{bmatrix} m_{00} & m_{01} & m_{02} & m_{03} \\ m_{10} & m_{11} & m_{12} & m_{13} \\ m_{20} & m_{21} & m_{22} & m_{23} \\ m_{30} & m_{31} & m_{32} & m_{33} \end{bmatrix} \begin{bmatrix} S_{0,in} \\ S_{1,in} \\ S_{2,in} \\ S_{3,in} \end{bmatrix} \tag{1}$$

Dual-polarization lidars return a combination of four **M**-coefficients; the exact four returned depends on the transmitted polarization state, $\vec{S_{in}}$. As opposed to dual-polarization systems, we will use "full-polarimetric" or Mueller systems, which completely describe the change of polarization state from input to output. To retrieve all 16 **M**-coefficients, we must take 16 measurements. This is further explained in section 1.1.2.

Despite – or perhaps because of – the prevalence and broad successes of dual-polarization lidar in active optical remote sensing of the atmosphere, there has been little exploration into more fully polarimetric lidar, even as it relates to sensing solid objects. Previous research in full-polarization lidar has used so-called "Mueller matrix polarimetric imaging lidar" developed for improved detection of samples submerged in water [23] as well as in two polarimetric approaches to the detection of biological warfare agents [24, 25]. The potential depth of new information represented by this Mueller matrix active polarimetry has been noted in previous publications, along with some initial work on classifying materials using the polarization bidirectional reflectance distribution function (P-BRDF) in laboratory settings [26–29]. The Air Force Research Laboratory (AFRL) is developing a novel fully polarimetric time-of-flight lidar instrument [4, 30, 31], with the hope that it will provide more information per return signal than other systems. We still have a great deal to explore regarding optical polarization properties of objects and scenes beyond the cross-polarization return observed in dual-polarization systems. To that end, some completed work presented

here in Ch. 2 and reported publicly in [1] and [32] covers the design and validation of a simple polarimeter to promote near-monostatic characterization of a broader variety of samples.

Existing fully-polarimetric remote sensing research – for both passive and active systems – has recognized a continued lack of understanding for the significance of circular polarization states [33]. We will advance the state of polarization-enhanced remote sensing by improving the understanding of the fully-polarimetric response of materials and by developing a high-accuracy testbed which can be used to measure the range-dependent polarization effects of inclement atmospheric conditions such as precipitation, fog, or smoke.

1.1.2 Polarimetric Bidirectional Reflectance Distribution Function

When light scatters off materials, its polarization changes. Scattering off of solid, opaque objects is generally considered in terms of the reflection. In this dissertation, we will refer to such objects as samples by default, with collections of samples referred to as a scene. The amount of light reflected from a sample toward a receiver depends mainly on the angle of the incident light to the surface normal and the angle from the surface normal to the receiver; the relationship defined by the bidirectional reflectance distribution function (BRDF) [34],

$$f_r(\theta_i, \phi_i, \theta_v, \phi_v, \lambda) = \frac{dL_r(\theta_v, \phi_v; E_i)}{dE_i(\theta_i, \phi_i, \lambda)}, \tag{2}$$

where θ_i and θ_v are the azimuth angles and ϕ_i and ϕ_v are the elevation angles for the incident light and viewing geometry, respectively, λ is the wavelength of incident and reflected light (elastic scattering is assumed), L_r is the reflected radiance $[\frac{W}{m^2 sr}]$, and E_i is the incident irradiance $[\frac{W}{m^2}]$. A similar metric is the bidirectional reflectance factor (BRF), which is simply the BRDF of a surface divided by the BRDF of an ideal Lambertian surface. Since a Lambertian surface is isotropic in the viewing hemisphere, for which the projected solid

angle is π, the BRF is simply [34],

$$BRF(\omega_{\mathbf{i}}, \omega_{\mathbf{v}}, \lambda) = \pi * f(\omega_{\mathbf{i}}, \omega_{\mathbf{v}}, \lambda), \tag{3}$$

where $\omega_{\mathbf{i}}$ and $\omega_{\mathbf{v}}$ are angle vectors representing (θ_i, ϕ_i) and (θ_v, ϕ_v), respectively.

With polarized incident light, there is also a polarimetric component to this reflectance function, represented as a set of 16 BRDFs corresponding to each of the 16 **M**-coefficients. This extends f_r to a matrix, as in Eq. 4.

$$\mathbf{f^P}(\omega_{\mathbf{i}}, \omega_{\mathbf{v}}, \lambda) = \begin{bmatrix} f_{00}(\omega_{\mathbf{i}}, \omega_{\mathbf{v}}, \lambda) & f_{01}(\omega_{\mathbf{i}}, \omega_{\mathbf{v}}, \lambda) & f_{02}(\omega_{\mathbf{i}}, \omega_{\mathbf{v}}, \lambda) & f_{03}(\omega_{\mathbf{i}}, \omega_{\mathbf{v}}, \lambda) \\ f_{10}(\omega_{\mathbf{i}}, \omega_{\mathbf{v}}, \lambda) & f_{11}(\omega_{\mathbf{i}}, \omega_{\mathbf{v}}, \lambda) & f_{12}(\omega_{\mathbf{i}}, \omega_{\mathbf{v}}, \lambda) & f_{13}(\omega_{\mathbf{i}}, \omega_{\mathbf{v}}, \lambda) \\ f_{20}(\omega_{\mathbf{i}}, \omega_{\mathbf{v}}, \lambda) & f_{21}(\omega_{\mathbf{i}}, \omega_{\mathbf{v}}, \lambda) & f_{22}(\omega_{\mathbf{i}}, \omega_{\mathbf{v}}, \lambda) & f_{23}(\omega_{\mathbf{i}}, \omega_{\mathbf{v}}, \lambda) \\ f_{30}(\omega_{\mathbf{i}}, \omega_{\mathbf{v}}, \lambda) & f_{31}(\omega_{\mathbf{i}}, \omega_{\mathbf{v}}, \lambda) & f_{32}(\omega_{\mathbf{i}}, \omega_{\mathbf{v}}, \lambda) & f_{33}(\omega_{\mathbf{i}}, \omega_{\mathbf{v}}, \lambda) \end{bmatrix} \tag{4}$$

While some P-BRDF measurements have been performed with complex equipment in previous research [26, 27, 29, 35, 36], the physical reality of having transmitter and receiver on separate optical paths makes capturing cases near a monostatic geometry – where the incident and viewing angles are near or exactly aligned – prohibitively difficult. The omission of near-monostatic cases is generally considered a reasonable omission since BRDF research has focused primarily on improving passive sensing, for which the natural illumination and the receiver are necessarily on different optical paths in non-shadowed cases as well. However, active remote sensors such as lidars tend to fall into a monostatic or near-monostatic geometry. Therefore, we require additional measurements to fill these gaps in P-BRDF knowledge. To this end, we can simplify to the monostatic P-BRDF (P-mBRDF) in Eq. 5, which coincides with the most omitted portion of the P-BRDF from the previous literature.

$$\mathbf{f^{Pm}}(\omega_{\mathbf{i}}, \lambda) = \mathbf{f^P}(\omega_{\mathbf{i}}, \omega_{\mathbf{v}} = \omega_{\mathbf{i}}, \lambda). \tag{5}$$

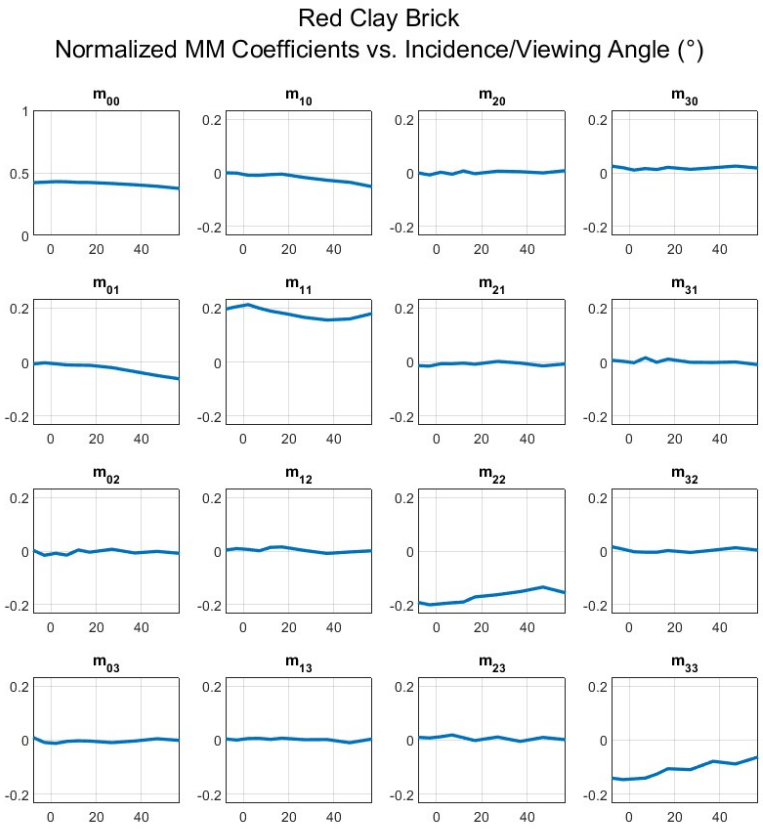


Figure 1: Mueller P-mBRDF of a red clay brick taken with an earlier iteration of the DMPL with a continuous laser source and functioning as a simple polarimeter.

These P-mBRDF data can be well-visualized in a set of 16 plots, which are common among the previously cited P-BRDF research and have been used in our completed work, as shown in Fig. 1.

As existing P-BRDF research has avoided the near-monostatic cases necessary for a lidar polarimetric material classification library, we have developed a simple polarimeter to perform P-mBRDF measurements and published some such results [1, 2] and a detailed account of the design and operation of such a device [32] with suggestions for alteration to fit specific measurement purposes. We will advance the state of active polarimetric material discrimination by providing theory and procedures to collect data, and by collecting these

data as reference samples for other stages of this research.

1.2 Objectives

The objectives of this proposal were 1) to design and build optimal polarization state generator (PSG) and analyzer (PSA) systems; 2) provide methods to fill knowledge gaps in material P-BRDF responses at or near monostatic geometries; 3) to design and build a fully-polarimetric lidar testbed operating in the visible and near-infrared; and, 4) to calibrate and validate the polarimetric lidar testbed against known samples and preliminary samples of interest, providing an operating procedure for future use.

1.2.1 Design & Build Optimal PSG & PSA systems

To achieve the other objectives in this research, we needed to build an optimal polarization state generator and analyzer. The primary optimal PSG and PSA design disucssion appears in Ch. 2 covering the initial, non-ranging polarimeter. Faster switching methods such as liquid crystal variable retarders (LCVRs) exist, but rotating polarizers and wave-plates are generally less expensive, more easily calibrated for tolerances, and more easily able to achieve any desired polarization state. The methods developed in this work will produce one optimal configuration, along with constraints which would allow for other optimal variations.

1.2.2 Develop (Near-)Monostatic P-BRDF Measurement Procedures

To improve the state of the field of opaque sample characterization by polarimetry, the second objective aims to develop, implement, and report the procedure for a simple method of monostatic (or near-monostatic) polarization bidirectional reflectance distribution function (P-BRDF). This objective is covered in Ch. 2 for the simple polarimeter, and in Ch. 4 for the calibrating, validating, and example urban material characterizations.

1.2.3 Design & Build Mueller Lidar (DMPL) Testbed

The primary deliverable for this dissertation project was the dichroic Mueller pulsed lidar (DMPL) testbed system. The initial design should include a transmitter with the above PSG illuminating a scene and a receiver with the above PSA collecting back-scattered light. Using a pulsed laser transmitter and high-speed photodetectors, we can gather ranging information as a time-of-flight lidar.

This objective is covered primarily in Ch. 5. More complex systems than this one will exist [4, 29, 31], but the simplicity of the test-bed should lend greater certainty to individual measurements and for data sets over the measurement period where the scene does not change significantly.

1.2.4 Calibrate & Validate DMPL Testbed

In order to determine the degradation of polarized returns due to inclement weather, we must also have reference scenes for which the polarized return is known under favorable environmental conditions. The simplest method is to measure reference scenes outdoors in mild weather, however this has the potential to leave many variables uncontrolled, such as wind speeds, temperatures, and relative humidity in the immediate vicinity of the measurements.

We can perform reference scene characterization in the lab instead, which has the benefit of being a more controlled environment, but the drawback of shorter measurement ranges. When measuring a scene at a shorter range, we will almost certainly need to angle the receiver optical axis slightly toward the transmitter optical axis in order to improve our geometric overlap. For some materials, such as those with more specular responses, this change in geometry may result in significant errors between a reference scene in the lab and the reference scene outdoors at a greater distance.

CHAPTER TWO

SIMPLE NEAR-MONOSTATIC MUELLER POLARIMETER

2.1 Contribution of Author and Co-Author

Manuscript in Chapter 2

Author: Nathaniel J. Field

Contributions: Conceptualization, Data acquisition and analysis, System design, build, and assessment, Writing – original draft

Co-Author: Joseph A. Shaw

Contributions: Conceptualization, Funding acquisition, Project administration, Resources, Supervision, Writing – review and editing

2.2 Manuscript Information

Nathaniel J. Field, Joseph A. Shaw

Applied Optics' Engineering and Laboratory Notes

Status of Manuscript:
____ Prepared for submission to a peer-reviewed journal
____ Officially submitted to a peer-reviewed journal
____ Accepted by a peer-reviewed journal
_X_ Published in a peer-reviewed journal

Optica Publishing Group
Submitted: 16 August 2024
Published: 26 September 2024
Vol. 63, No. 28
https://doi.org/10.1364/AO.538901

2.3 Abstract

Inferring material properties from active or passive polarimetric remote sensing requires knowledge of the polarized bidirectional reflectance distribution function (P-BRDF). To encourage and simplify the process of measuring the P-BRDF of materials in the monostatic or near-monostatic configurations seen in lidar and other active remote sensing systems, we describe the design, build, and operating procedure for a simple near-monostatic polarimeter. The described system operates at 1064 nm and with a transmitter-receiver separation of about 4°, but the design principles, alignment procedure, and measurement procedure can be directly applied to systems at other wavelengths or separation angles. Also included are the control and data analysis software for the instrument we deployed, and a small selection of retrievals from the instrument.

2.4 Introduction

Polarization represents a significant means of improving data density in combination with the more common retrieved light characteristics: intensity, spatial frequency, and spectral distributions. To date, polarization-enhanced remote sensing has focused primarily on passive methods [3] and dual-polarization lidar [9].

Polarization-enhanced lidar has been used for a wide variety of applications, especially in atmospheric and oceanic remote sensing [9]. It has also been used to improve the detection of submerged samples with sensors above the water [23]. Foliage and plant species discrimination are areas of interest in active polarimetric sample discrimination, including imaging polarimeters [37, 38], active lab-based polarimetry [35], and dual-polarization lidars [39]. There is also opportunity to improve material discrimination in complex scenes using polarimetry, as demonstrated in previous passive systems [7] and active systems [28, 40].

To more accurately identify samples in a scene, the community requires means to

characterize reference materials specific to their applications, similar to those which exist for satellite or other passive remote sensing systems. Data from previous works report material polarimetric responses by their polarized bidirectional reflectance distribution function (P-BRDF) [26, 27, 35, 36, 41]. However, of these reported P-BRDFs, only those in [36] included measurements of the monostatic configuration, the most common configuration for lidar and similar active polarimetry. These monostatic P-BRDF (P-mBRDF) returns are important for polarization-enhanced lidar with applications moving toward material discrimination.

In this paper, we describe the design, operating procedure, and data analysis methods for a simple near-monostatic polarimeter. We also show some data collected by the instrument we built, the LabView collection software we developed, and the MATLAB data analysis script used to process the raw intensity data into Mueller matrix P-mBRDF plots.

2.5 Background

For material discrimination, we are primarily interested in determining Mueller matrix, $\mathbf{M}$, values, which represent material properties. In active polarimetry, we use a polarization state generator (PSG) in combination with a light source, such as a laser, to illuminate the scene with known polarization characteristics, $\mathbf{S_G}$. Optical detectors are only directly capable of detecting the power or photon flux incident on their active surface, so a polarization state analyzer (PSA) with a known polarization response, $\mathbf{M_A}$, is used to attenuate total power as a function of the incident light's polarization state. Extended to an equation, the PSG-PSA active polarimetric system is described as

$$\mathbf{S_{det}} = \begin{bmatrix} S_{0,det} \\ S_{1,det} \\ S_{2,det} \\ S_{3,det} \end{bmatrix} = \begin{bmatrix} I_{det} \\ Q_{det} \\ U_{det} \\ V_{det} \end{bmatrix} = \mathbf{M_A S_{Rx}} = \mathbf{M_A}(\mathbf{M_{samp} S_G}), \tag{6}$$

where $\mathbf{S_{det}}$ describes the light at the detector and $\mathbf{M_{samp}}$ describes the polarization sensitive properties of the sample in the scene. As seen above, a Stokes vector can be broken down into its four components. The S_0 or I element represents the total power regardless of polarization, and is the only element measured by the detector's active area. As such, we require a minimum of 16 unique measurements to fully reconstruct an unknown $\mathbf{M_{samp}}$. This is most often accomplished by setting four PSG states and four PSA states and performing measurements for each of the unique PSG-PSA state combinations.

Optimization of polarimetry systems primarily concerns proper selection of these PSG and PSA states. As shown in previous literature, optimal PSG states are those matched to the PSA states [42, 43]. Selecting optimal PSA states is best conceptualized using the Poincaré sphere, where optimal polarization states have Poincaré coordinates which define a regular polyhedron [44, 45]; for four PSA states, this generates a regular tetrahedron.

Following the processes in previous literature, we can quantify the maximum error propagation for transmitter and receiver errors, including noise, by determining the condition number, κ, of the PSG and PSA system matrices [43, 45]. The condition number for the PSG, κ_G, represents the maximum error propagation of intensity or polarization noise in the Tx source. The condition number for the PSA, κ_A, represents the maximum error propagation of noise in the Rx detector.

To find κ for each branch of the radiometer, we use

$$\kappa(\mathbf{A}) = ||\mathbf{A}||_2 \; ||\mathbf{A}^{-1}||_2 = \frac{\sigma_{max}(\mathbf{A})}{\sigma_{min}(\mathbf{A})}, \tag{7}$$

where $||\cdot||_2$ is the L^2 norm, σ_{max} and σ_{min} are the maximum and minimum singular value decompositions, and $\mathbf{A}$ is the analysis matrix of the system's polarization elements, defined

as

$$\mathbf{A} = \begin{bmatrix} \mathbf{M_0^1} \\ \mathbf{M_0^2} \\ \mathbf{M_0^3} \\ \mathbf{M_0^4} \end{bmatrix} = \begin{bmatrix} m_{00}^1 & m_{01}^1 & m_{02}^1 & m_{03}^1 \\ m_{00}^2 & m_{01}^2 & m_{02}^2 & m_{03}^2 \\ m_{00}^3 & m_{01}^3 & m_{02}^3 & m_{03}^3 \\ m_{00}^4 & m_{01}^4 & m_{02}^4 & m_{03}^4 \end{bmatrix}, \tag{8}$$

where $\mathbf{M_0^i}$ is the first row of the combined Mueller matrix of the polarization elements for the PSG's or PSA's ith state. When A is singular (or near-singular) you may need to use the pseudo-inverse of A in Eq. 7 instead of the simple A^{-1} inverse. For an optimal configuration, the condition number of the PSG and PSA are each equal to $\sqrt{M-1}$, where M is the dimensionality of the polarization (3 for linear systems and 4 for full-polarimetric systems). Therefore, an optimal system will have $\kappa_G = \kappa_A = \sqrt{2}$ for a linear polarimetry system, or $= \sqrt{3}$ for a full-polarimetric system.

2.6 Instrument Design

2.6.1 Example Design

In this section, we walk through the design of the active polarimeter we built, and provide reasoning such that others could design similar systems at different wavelengths using the same principles. An overhead view of the system we built is shown in Fig. 2 with components labelled.

The instrument begins with a simple active radiometer: a laser transmitter (Tx) and a photodiode receiver (Rx). The system we built used a 10-mW, 1064-nm, diode-pumped solid-state laser and a ThorLabs PDA10CS2 photodiode, which is an InGaAs, variable-gain detector with a 1-mm-diameter circular active area. To reduce speckle effects, the 1-mm-diameter laser beam was expanded by a 10x beam expander; this also increased the beam divergence from about 0.5 mrad to 5 mrad. For the receiver optics, we used a single 50-mm-focal-length plano-convex lens with a 25-mm clear aperture, resulting in a full field-

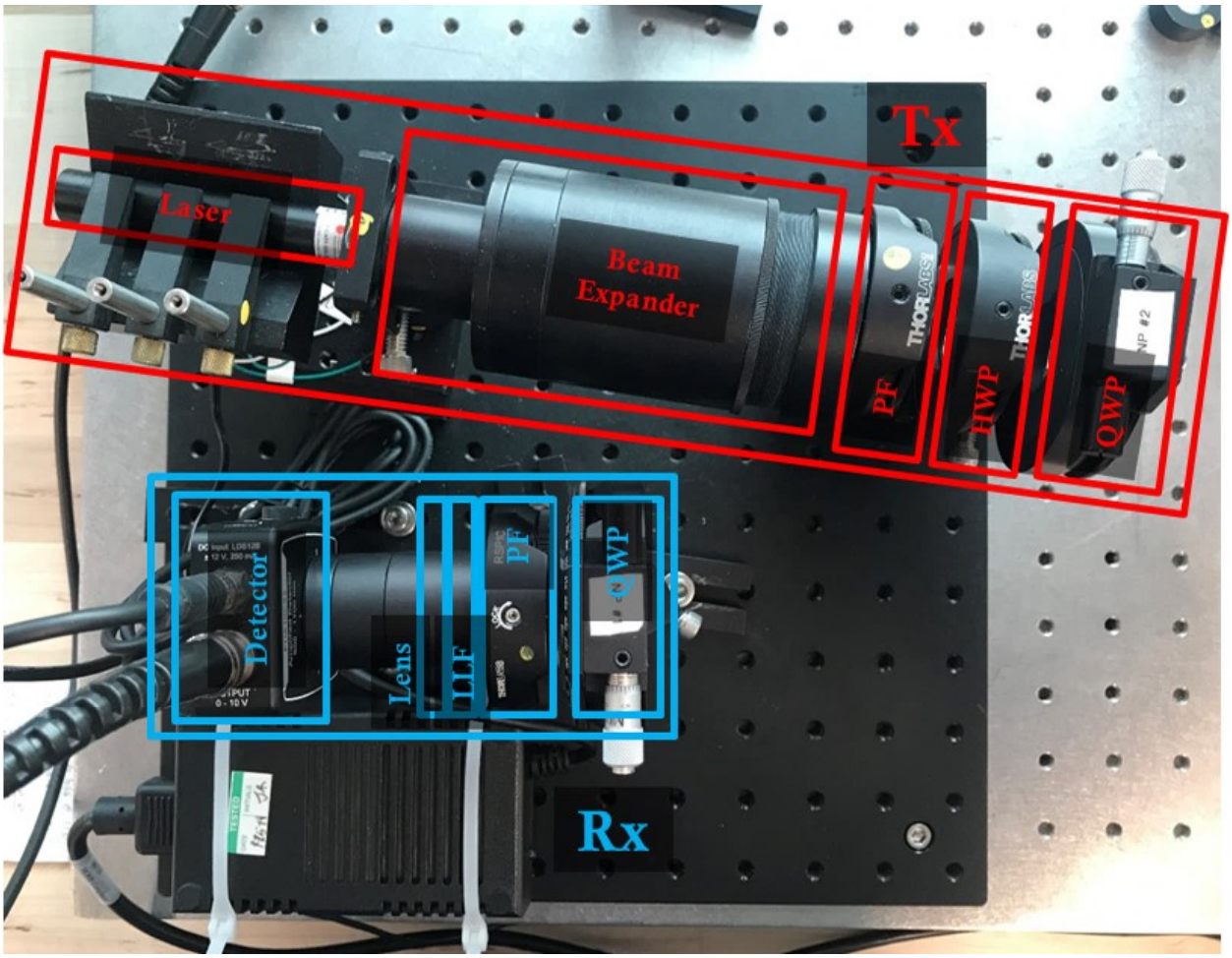


Figure 2: Overhead image of the simple polarimeter, with the transmitter optics labelled in red and the receiver optics labelled in blue. This figure is a partial reproduction of a figure in [1].

of-view (FOV), ω_{FOV}, of 10 mrad, which is about double the transmitter beam divergence. Placing the planar side toward the detector and the convex side toward the scene minimizes aberrations for the simple lens system. Finally, a 10-nm bandwidth laser-line spectral filter (LLF) for a 1064-nm central wavelength was placed on the scene side of the receiving optics to eliminate the majority of background light from the scene.

The PSG was inserted in front of the transmitter and consisted of a linear polarizing filter (PF), a half-wave retarder (HWP), and a quarter-wave retarder (QWP). The PF was locked to transmit vertical linear polarization, and the laser was rotated in its mount

until maximum transmittance through the filter was achieved. This provided a much purer initial polarization state than the laser alone, since the PF used has an extinction ratio of approximately 10^3. The HWP was set in a rotation mount, which allowed us to rotate the initial linear state to other orientation angles without attenuation. The QWP was set with its fast axis at 45° on a 90° flip-mount, allowing it to be inserted into or removed from the optical path quickly and easily.

The PSA was inserted in front of the receiver optics and consisted only of a QWP and a PF. The QWP was set to -45° on a 90° flip-mount for the same purpose as in the PSG. The PF was set in a rotation mount to allow for preferential attenuation for different linear orientation angles.

For an analog-digital converter (ADC), we used a National Instruments USB-6001 data acquisition device. For a total list of parts, excluding some minor optomechanical mounting equipment, see Table 1.

Table 1: Developed System Parts and Approximate Costs

Part	Cost, $
Laser (Edmund Optics #37-043)	350
Detector (ThorLabs PDA10CS2)	475
PF (Meadowlark DPM-100-NIR2-1) ×2	2 × 685
HWP (Meadowlark NHM-100-1064)	575
QWP (Meadowlark NQM-100-1064) ×2	2 × 575
ADC (NI USB-6001)	300
Rotation Mount (ThorLabs RSP1) × 5	5 × 100
Flip Mount (ThorLabs FM90) × 2	2 × 100
Lenses	100
total	5,020

2.6.2 System Analysis

For the purposes of compiling and potentially sharing reference measurements, it's important to know the specifications of the systems acquiring the reference data. Some critical system information includes the operating wavelength, actual geometric separation

angle between transmitter and receiver, receiver FOV, and other specifications for which we give an example summary in Table 2.

The operating wavelength is critical information as many materials exhibit reflectance and transmittance characteristics which are strongly spectrally dependent. To a lesser extent, the receiver optical bandwidth can also be useful information when considering the spectral effects on the sample characteristics. The transmitter beam diameter at the output, beam divergence, and beam diameter at the sample help inform the probability of speckle error and the total illumination area considered for samples with spatial anisotropy. The viewing solid angle, Ω_v, which should be relatively narrow for the purpose of P-mBRDF characterization, is determined by the smaller of the solid angles produced by Eq. 9 or Eq. 10.

$$\Omega_v^{FOV} = \pi \sin^2(\frac{\omega_{FOV}}{2}) \tag{9}$$

$$\Omega_v^{A} = \frac{A_s}{Z^2} = \frac{\pi D_s^2}{4Z^2} \tag{10}$$

Finally, the actual geometric separation angle between the transmitter and receiver is critical to report the actual monostatic or near-monostatic nature of the characterizing measurement.

The signal-noise ratio (SNR) for the developed system was calculated using a theoretical signal for a 10% Lambertian reflector against the detector noise equivalent power (NEP). In a lab setting, the optical power incident on the detector, P_{Rx}, follows a basic radiometric equation,

$$P_{Rx} = A_{Rx}\Omega_v L_s = \frac{\pi D_{Rx}^2}{4}\Omega_v \frac{4 I_{Tx}\rho_s T_{atm}}{\pi^2 D_s^2} = \frac{D_{Rx}^2 \Omega_v I_{Tx}\rho_s T_{atm}^2}{\pi D_s^2}, \tag{11}$$

where ρ_s is the reflectance of a Lambertian sample reflector and T_{atm} is the transmittance of the atmosphere (typically about 1 in a lab setting). For the developed system, P_{Rx} comes out to about 0.269 μW, and the maximum NEP for the detector is 0.166 μW, giving an

initial SNR of 1.62, or equivalently, 4.2 dB. The ADC has a sampling rate of 20 kS/s, so averaging over 0.5 seconds gives 10,000 samples, and improves the SNR by a factor of 100, to about 162, or equivalently, 44.2 dB.

For ease of use, the nearest-optimum states we can select are a circular state (RHC) and three linear states with orientations equally separated by 60°, which we select as 0°, 60°, and 120°. Using these states for both PSG and PSA, the condition numbers are $\kappa_G = \kappa_A \approx 2.48$. This means any output intensity noise after the clean-up polarizer, whether due to intensity or polarization instability in the laser, can propagate to the polarization measurements with a maximum magnification of 2.48. Similarly, noise in the detector can propagate to Mueller matrix element calculation with a maximum magnification of 2.48. These κ values are only about 43% greater than those for an optimal Mueller polarimeter, $\sqrt{3} \approx 1.73$.

The maximum error propagation reduces the SNR of the polarimetric results as compared to the system SNR.

$$SNR_{pol} = \frac{SNR_{sys}}{\kappa_A} \tag{12}$$

The values are summarized in Table 2.

Table 2: Developed System Specifications

Parameter	Value
Operating wavelength, λ	1064 nm
Receiver optical bandwidth, $\Delta\lambda$	$\pm$5 nm
Transmitter optical power, I_{Tx}	10 mW
Beam diameter at output, D_b	10 mm
Beam divergence, ω_{div}	5 mrad
Beam diameter at sample, D_s	13.8 mm
Distance to sample, Z	762 mm
Receiver aperture diameter, D_{Rx}	25 mm
Full FOV, ω_{FOV}	10 mrad
Tx-Rx separation angle, θ_Δ	4°
Sample rotation axis	y-axis (vertical)
System signal-noise ratio, SNR_{sys}	162 (44.2 dB)
Max error propagation, $\kappa_G = \kappa_A$	2.48
Min polarimetric SNR, SNR_{pol}	65.3 (36.3 dB)

2.7 Operating Procedure and Data Analysis

2.7.1 Optomechanical Alignment

Alignment of the polarimeter optical trains is relatively straightforward. Use multiple irises to align a beam expander or similar optics along the transmitter optical path. For the receiver, a lens tube attached to the detector containing the focusing lens at its focal length from the detector active area is typically sufficient for axial alignment. Measuring the focal length separation to within about 1% error is generally sufficient for this type of radiometry as it is non-imaging.

After inserting an LLF, or while in a dark lab, but before inserting the polarization elements, use a diffuse reflectance sample and rotate either the transmitter or receiver optical paths until you receive a maximum signal. Lock the transmitter and receiver in place and note the geometric separation angle, θ_Δ, of their optical paths. Also, note the maximum signal you achieved; this will help in polarizer alignment.

The angular geometry used in the data we gathered is summarized in Fig. 3, which is useful for similar fixed-separation systems. The reference 0° angle is where the sample surface normal is pointed halfway between the optical axes of the transmitter and receiver. Rotations of the surface normal toward the transmitter are referred to with positive angles, and rotations toward the receiver are referred to with negative angles.

Next, insert the transmitter PF with its transmission axis as horizontal as possible; most rotation mounts should allow for 1° (17.5 mrad) tolerance or better on this orientation angle. For the purposes of this procedure, horizontal orientation is 0°, vertical orientation is 90°, and 45° orientation is above horizontal and to the right of vertical when looking into the beam. If possible, rotate the laser head to maximize the power through the polarizer, as measured by the aligned receiver. Otherwise, you might consider rotating the PF to achieve max power throughput, shifting the suggested orientation angles of each of the other

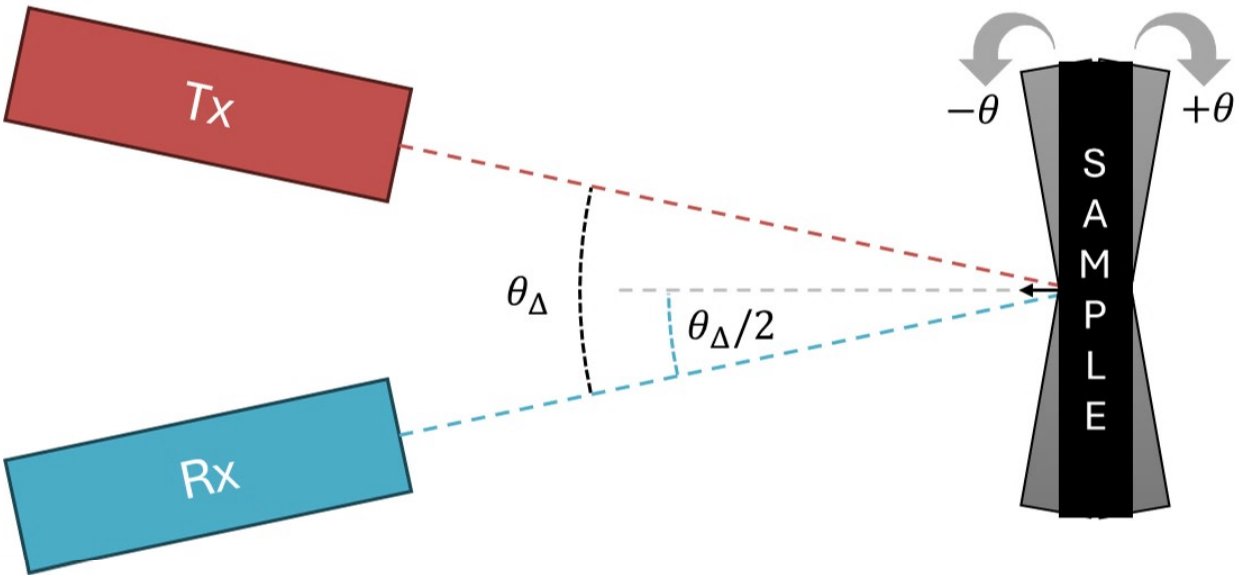


Figure 3: Overhead diagram depicting the geometric separation angle, the surface-normal 0° reference setup, and the general orientation of positive and negative viewing/illumination angles.

polarizer elements by the same amount. Lock the transmitter PF in place.

Then insert the receiver PF and rotate it until you have a minimum signal at the detector. Note the rotation angle as 90°, or otherwise at 90° from the transmitter PF orientation.

Leaving the receiver PF at this crossed orientation, insert the transmitter HWP and rotate it until you return to a minimum signal at the detector. Note this HWP orientation as the crystal axis aligned to the transmitter PF orientation (0° by default).

The transmitter QWP should be labelled with a fast-axis (sometimes referred to as the crystal axis). Insert the transmitter QWP and rotate it so that the fast axis is at about -45° from the transmitter PF orientation. Alternate the receiver PF between 0° and 90° (co- and cross-polarized with the transmitter PF) while rotating the QWP in small increments about

-45° until the co- and cross-polarized signals are equal. This produces right-hand circular (RHC) polarization. Lock the transmitter QWP in place, then flip it out of the optical path and repeat this process with the receiver QWP but at and about +45° orientation.

2.7.2 Control and Analysis Software

The control software is programmed in LabView 2019. The software relies on drivers for the Newport USB-6001, but otherwise functions using basic LabView controls. This software is available in Code 1 (Ref. [46]).

The analysis software is programmed in MATLAB 2023a. This software loads .csv files as saved by the control software, reports the Mueller matrices as figures, and records the Mueller matrices as a function of angle in new .csv files, with each row of the file in the form $[\theta_v\ m_{00}\ m_{01}\ m_{02}\ m_{03}\ m_{10}\ ...\ m_{32}\ m_{33}]$. This software is available in Code 2 (Ref. [47]).

2.7.3 Data Collection Procedure

To characterize the P-mBRDF (or a fixed Tx-Rx separation P-BRDF) of a sample, either the sample or polarimeter must be rotated with respect to the other. In many cases, a fixed polarimeter with a rotating sample provides the most simply realized setup. We mounted samples on a stage rotating about the y-axis (vertical axis). The samples were set at about 0.75 m from the front of the transmitter and receiver (see Table 2 for specific values).

When necessary, samples are prepared so they are planar. For example, a Spectralon reference or brick are rigid materials with a tall, flat face which does not need to be prepared. However, a roofing shingle or plant leaf are not rigid, and so must be attached to a backing surface such as a piece of wood in preparation. Once on a rigid surface of sufficient height, a horizontal rotation stage can be used as shown in Fig. 4 to make repeatable sample rotation much easier.

Once the sample is prepared and in place, follow the semi-time-optimized procedure here in combination with the control software noted above:

1. Set the sample at a known incidence angle.
2. Set the HWP_G to 0° and the PF_A to 0°. Flip the QWP_G and QWP_A out of the optical path.
3. In the control software, SCAN for Stage 1.
4. Flip the QWP_A into the beam path. SCAN for Stage 2.
5. Flip the QWP_G into the beam path. SCAN for Stage 3.
6. Flip the QWP_A out of the beam path. SCAN for Stage 4.
7. Rotate the PF_A to 60°. SCAN for Stage 5.
8. Flip the QWP_G out of the beam path. SCAN for Stage 6.
9. Rotate the PF_A to -60°. SCAN for Stage 7.
10. Flip the QWP_G into the beam path. SCAN for Stage 8.
11. Flip the QWP_G out of the beam path, rotate the HWP_G to -30°. SCAN for Stage 9.
12. Rotate the PF_A to 60°. SCAN for Stage 10.
13. Rotate the PF_A to 0°. SCAN for Stage 11.
14. Flip the QWP_A into the optical path. SCAN for Stage 12.
15. Rotate the HWP_G to 30°. SCAN for Stage 13.
16. Flip the QWP_A out of the optical path. SCAN for Stage 14.

17. Rotate the PF_A to 60°. SCAN for Stage 15.

18. Rotate the PF_A to -60°. SCAN for Stage 16.

19. Set the sample to a new known incidence angle and repeat steps 2-19 until you have completed your angular analysis.

In this procedure, the polarizing elements are distinguished as being part of the PSA or PSG with a subscript A or G, respectively. For example, QWP_A is the QWP in the PSA (receiver) arm of the polarimeter.

For our data collection efforts, we typically scanned from -60° to 60 °, or a smaller range on one side or the other for geometries where symmetry is expected or previously demonstrated. These angular limitations are primarily due to the illumination area overfilling some of the smaller samples as their projected area decreases.

Using this procedure, we have found that an experienced operator can complete a 16-measurement set in about 1 to 3 minutes, and a new operator can typically complete a measurement set in about 6-8 minutes. The total measurement time for a sample then depends on how many viewing/illumination angles are considered.

2.7.4 Data Structure and Analysis

The control software records measurement data as .csv files containing $N \times 17$ matrices, where N is the number of angles for which measurement sets were recorded. Each row is a 17-element matrix, with the first element giving the incidence-viewing angle, θ_v, and the remaining 16 elements giving the recorded signal (in mV) for each of the unique PSG-PSA states. The states are given in the order of vertical-vertical, vertical-60°, vertical-120°, vertical-circular, 60°-vertical, ... circular-120°, and circular-circular. This is the structure expected by the analysis software.

The data analysis is performed using linear regression to reduce processing time. The fundamental principle follows from a simple Mueller calculus equation,

$$\vec{S_{g,a}} = \begin{bmatrix} I_{g,a} \\ Q_{g,a} \\ U_{g,a} \\ V_{g,a} \end{bmatrix} = \mathbf{M_a M_{samp}} \vec{S_g}, \tag{13}$$

where $\vec{S_{g,a}}$ is the Stokes vector of light reaching the detector, $\mathbf{M_a}$ is the analysis Mueller matrix, $\mathbf{M_{samp}}$ is the unknown Mueller matrix response of the sample, and $\vec{S_g}$ is the Stokes vector of the light generated in the transmitter arm. Since the detector can only measure intensity, the equation extends out to

$$\begin{aligned} I_{g,a} = I_g(&m_{a00}m_{s00} + m_{a01}m_{s10} + m_{a02}m_{s20} + m_{a03}m_{s30}) \\ &+ Q_g(m_{a00}m_{s01} + m_{a01}m_{s11} + m_{a02}m_{s21} + m_{a03}m_{s31}) \\ &+ U_g(m_{a00}m_{s02} + m_{a01}m_{s12} + m_{a02}m_{s22} + m_{a03}m_{s32}) \\ &+ V_g(m_{a00}m_{s03} + m_{a01}m_{s13} + m_{a02}m_{s23} + m_{a03}m_{s33}), \end{aligned} \tag{14}$$

a simple linear combination equivalently represented as

$$I_{g,a} = \vec{B_{g,a}} \vec{A}, \tag{15}$$

where

$$\begin{aligned} \vec{A} = vec(\mathbf{M_{samp}}) = [&m_{s00}\ m_{s10}\ m_{s20}\ m_{s30}\ m_{s01}\ m_{s11}\ m_{s21}\ m_{s31} \\ &m_{s02}\ m_{s12}\ m_{s22}\ m_{s32}\ m_{s03}\ m_{s13}\ m_{s23}\ m_{s33}]^T \end{aligned} \tag{16}$$

and

$$\vec{B_{g,a}} = [I_g m_{a00}\ I_g m_{a01}\ I_g m_{a02}\ I_g m_{a03}$$
$$Q_g m_{a00}\ Q_g m_{a01}\ Q_g m_{a02}\ Q_g m_{a03}$$
$$U_g m_{a00}\ U_g m_{a01}\ U_g m_{a02}\ U_g m_{a03}$$
$$V_g m_{a00}\ V_g m_{a01}\ V_g m_{a02}\ V_g m_{a03}]. \quad (17)$$

Extending Eq. 15 to the 16 measurements for each unique combination of g and a, we can expand the scalar $I_{g,a}$ to the 1 x 16 vector $\vec{I_{meas}}$, and expand the 1 x 16 vector $\vec{B_{g,a}}$ to the 16 x 16 matrix $\mathbf{B}$. Then, solving for $\vec{A}$, which is a simple vectorization of the sample Mueller matrix, we find

$$\vec{A} = \mathbf{B^{-1}} \vec{I_{meas}}. \quad (18)$$

2.8 Example Material Measurements

Some example data recorded with the example system design are presented here. These data represent the near-monostatic response of a red clay brick sample and a tar-fiberglass shingle sample, as previously reported in [1]. These data also have their m_{00} elements normalized to the near-normal returns of a Spectralon Lambertian reference of known reflectance. The plots shown here are also available in greater resolution in [1].

The red clay brick sample, shown in Fig. 5, was relatively matte and of middling reflectance at the operating wavelength. As such, we expect relatively flat reflectance across θ_v, with a slight dip at steeper angles and a moderate increase in polarizance and diattenuation at steep angles as well. These features can be observed in the results shown in Fig. 5, and we can also see that the off-diagonal elements for rotation and phase offset are minimal relative to the diagonal elements.

A tar-fiberglass shingle was also measured, as seen in Fig. 6. This sample was the least in-line with expected Lambertian or specular surface responses. The shingle consisted primarily of 1- to 3-mm diameter rough fragments of tar overlaying a thin layer of fiberglass insulation which was still visible in places through the tar. The reflectance was fairly Lambertian, at least in line with the brick's. Likely due to the high anisotropy of the tar fragments, there was also no significant increase in polarizance and diattenuation at steeper θ_v. For a rough surface, we would expect a reduction in polarization maintenance (the diagonal elements), but we see relatively strong maintenance in this sample. Dark surfaces and specular reflectors both have stronger polarization maintenance, and it is unclear for such a complex sample if this effect is due to the darkness of the tar or the high reflectance of the visible regions of fiberglass.

2.9 Discussion

We have discussed the purpose, theory, and design principles for simple monostatic and near-monostatic polarimeters. The example design and cited software serve to enable groups with shared interest in active polarimetry for sample discrimination to develop their own reference measurements.

One of the major limitations of our example system is that it records only at 1064-nm wavelength. As spectral characteristics of materials change, their polarimetric responses are all but certain to change as well. For groups aiming to make a simple instrument to characterize materials for other devices at specific operating wavelengths, such as a lidar operating at a single wavelength, this narrow spectral reference will work well so long as the simple polarimeter has the same wavelength as the main device.

The other limitation of our example system is that it is not truly monostatic. The system for which we were generating sample references was not truly monostatic, so a near monostatic was sufficient for our research. If, however, a true monostatic geometry is

preferred, a group could use a non-polarizing beam-splitter in front of the Tx output which reflects some of the Tx signal into a beam-block, then reflects a fraction of the return signal out of the primary optical path to a Rx setup on the reflected path. This option produces a true-monostatic geometry, but may complicate design due to higher power requirements to produce similar SNR.

Another consideration, given the longer time scale of the measurement sets, is the transmitter power stability, and by extension, its polarization stability. This is relatively simply measured by placing the transmitter source behind the clean-up polarizer and firing into a detector, taking constant measurements for about 15 to 20 minutes. The laser need only be stable (not changing significantly) over the time period typical of a 16-measurement set; about 1-3 minutes for an experienced operator or 6-8 minutes for a newer operator.

Though it results in a much more expensive system, motorized rotation stages can be used in place of the manual rotation stages. In such a system, it is similarly efficient to realize a polarimetrically optimized set of PSG-PSA state combinations. For such a setup, we recommend the following four states for the unique states of the PSG and PSA individually, reported as their Poincarè coordinates $(2\theta_{PF}, \phi_{\Delta}, DoP)$: (0°, 90°, 1), (0°, -19.4712°, 1), (120°, -19.4712°, 1), and (-120°, -19.4712°, 1).

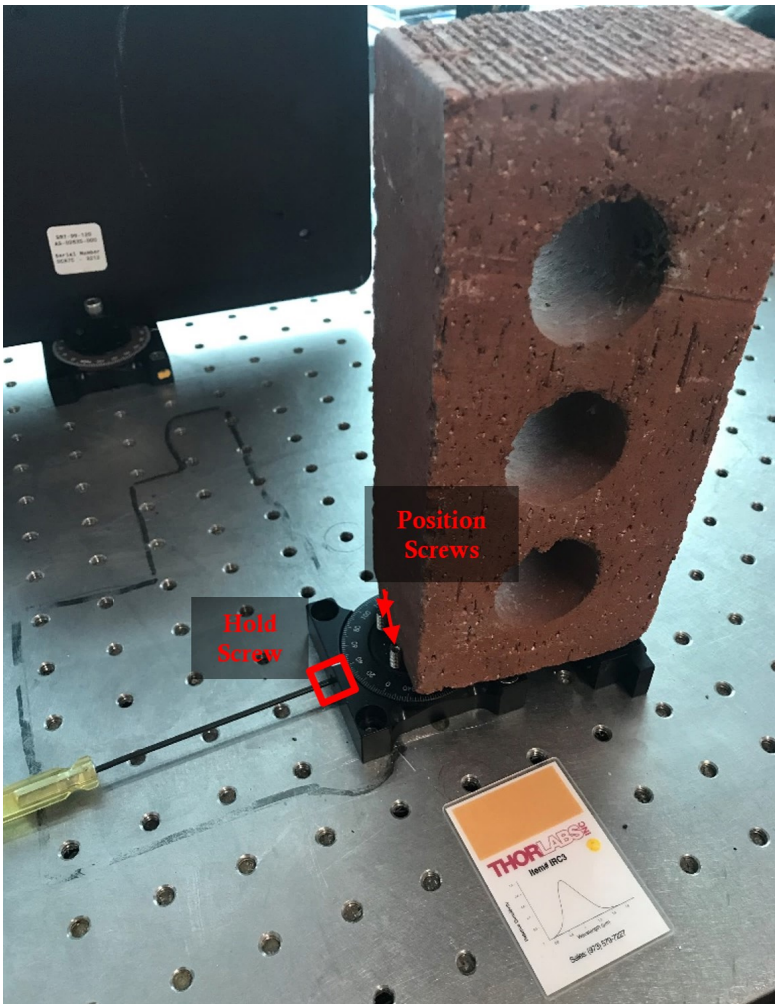


Figure 4: The red clay brick sample on a horizontal rotation stage. Two set screws make it easy to return the brick to the same position repeatably, and to more accurately determine the invidence/viewing angle, θ_v, relative to the polarimeter. This figure is a partial reproduction of a figure in [1].

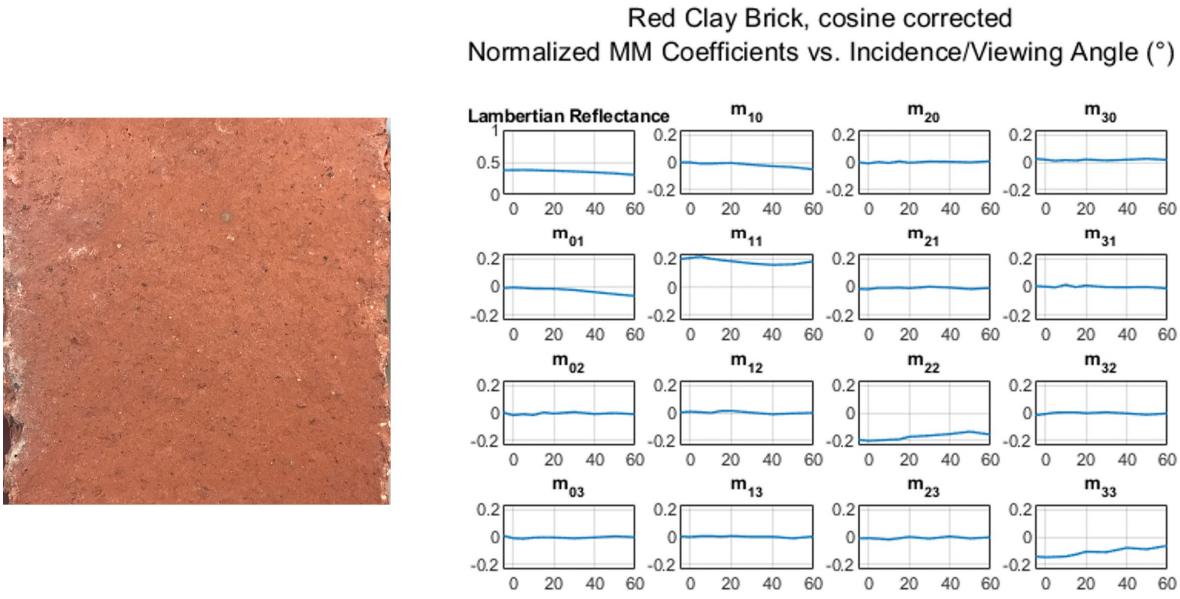


Figure 5: An image of the sample brick surface about the measurement location (left) and the resulting P-mBRDF measurement (right).

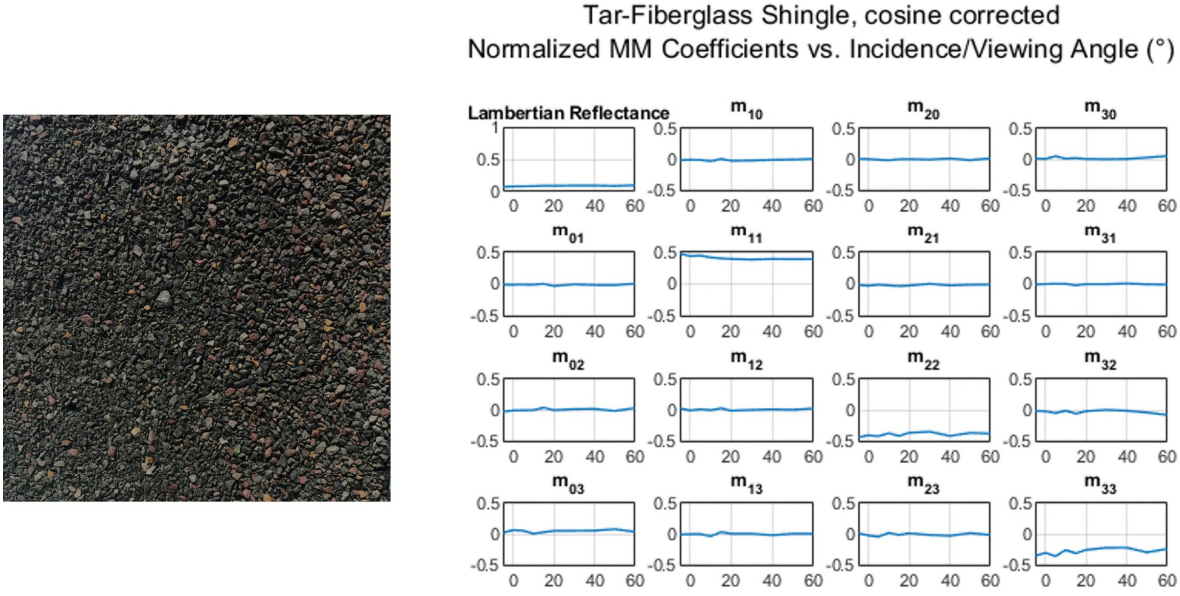


Figure 6: An image of the sample tar-fiberglass shingle surface about the measurement location (left) and the resulting P-mBRDF measurement (right).

CHAPTER THREE

REFLECTANCE RELATIVE CALIBRATION

Calibration refers to the association of a system's response to a stimuli to the units associated with some element outside the system. For example, a radiometric calibration of a photodetector and lens system associates the electrical response of the system to the radiance $[\frac{W}{sr*m^2}]$ of an external source. Many passive systems, and some active systems as well, use a so-called reflectance calibration. But reflectance lacks units and so cannot be directly calibrated. Instead, a relative calibration is performed, in which two calibrations with like units are combined to simplify their procedures and the result is unitless.

3.1 Constraining the BRDF

In this method, we ultimately aim to associate a scene's bidirectional reflectance distribution function (BRDF) values, f_r, to a given electrical signal return to the receiver, V, given a ratio input electrical power to the transmitter. Although we use the variable V, the electrical signal might be represented by current or digital number instead of voltage.

Beginning with the general form of the bidirectional reflectance distribution function (BRDF) [34], f_r, of a scene illuminated by the transmitter and observed by the receiver, we state

$$f_r(\omega_i, \omega_v) = \frac{dL_r(\omega_v, \omega_i)}{dE_i(\omega_i)}, \tag{19}$$

where L_r is the received radiance in $[\frac{W}{m^2 sr}]$, E_i is the illuminating irradiance in $[\frac{W}{m^2}]$, and ω_i and ω_v are angle vectors representing (θ_i, ϕ_i) and (θ_v, ϕ_v), respectively. There are spectral forms of this equation, but for the systems discussed in this dissertation we need only generate one calibration function for a given operating wavelength, and these functions take the same form.

The illumination for our system, E_i, is confined to within the incident solid angle Ω_i; note that we use Ω to denote solid angles and Ω^P to denote projected solid angles; projection simply multiplies the base value by $\cos(\delta)$, where δ is the separation between the viewing or illumination direction and the reference optical axis. As such, we can translate dE_i to a discrete ΔE_i.

$$\Delta E_i = \Delta E_0 \cos(\theta_i), \tag{20}$$

where ΔE_0 is the source irradiance at normal incidence.

Similarly, the received radiance is constrained to within the received solid angle, Ω_v. By default, this constraint is the receiver FOV solid angle, Ω_{FOV}.

$$\Omega^P_{FOV} = \frac{A_{ep}\cos(\theta_v)}{R^2_{sc}} \tag{21}$$

Considering the received radiance, we expand the basic radiometer equation as

$$\Delta L_r = \frac{\Phi}{A\Omega^P} = \frac{\rho_{cc}(T_{sys}T_{atm})\Delta E_i A_{sc}}{A_{ep}\Omega^P_{sc}} \tag{22}$$

where ρ_{cc} is the biconical reflectance, the T terms are transmittance values of the optical system and the atmosphere, A_{sc} is the area of the scene, A_{ep} is the area of the receiver entrance pupil, and Ω_{sc} is the scene solid angle. Following from Eqs. 19 and 22, we find a discrete and constrained form of the BRDF,

$$\Delta f_r = \frac{\rho_{cc}(T_{sys}T_{atm})A_{sc}}{A_{ep}\Omega^P_{sc}} \tag{23}$$

This is the discrete form of the BRDF, but we will generally refer to it as simply f_r as done in most literature. Additionally, both A_{sc} and Ω_{sc} are limited by the viewing geometry – whether the system is over-filled or under-filled.

3.1.1 Geometric Considerations

The geometry of a reference sample and the specifications of the remote sensing system determine the scene projected solid angle, Ω_{sc}. The limiting Ω_{sc} is the smaller of the FOV solid angle, Ω_{FOV}, or the solid angle set by the sample's projected area and range, Ω_s. The three possible cases for overlap – over-filled, under-filled, or critically filled FOV – are presented visually in Fig. 7. When the FOV is over-filled by the illuminated surface, the limiting Ω_{sc} is the constant system parameter,

$$\Omega_{FOV} = 4\pi \sin^2(\frac{\theta_{FOV}}{2}) \approx \frac{A_{ep}}{R_{sc}^2}, \tag{24}$$

where θ_{FOV} is the half-angle field-of-view for the receiver, A_{ep} is the area of the receiver entrance pupil, and R_{sc} is the range from the receiver's entrance pupil to the center of the sample's projected area.

On the other hand, when the FOV is under-filled, the limiting Ω_{sc} is determined by

$$\Omega_{ill}^P = \frac{A_{sc}^P}{R_{sc}^2} = \frac{A_{sc}\cos(\theta_v)}{R_{sc}^2} \tag{25}$$

where A_{sc}^P is the projected area illuminated on the sample relative to the optical path of the receiver and A_{sc} is the illuminated area on the sample. A critically filled geometry is a special case where $\Omega_{sc} = \Omega_{FOV} = \Omega_{ill}$, and it behaves in the same way as an under-filled geometry for the purpose of calibration and measurement; however, critically filled geometries are difficult to practically achieve and are generally undesirable if there is any potential for the beam to walk due to turbulent atmosphere or other environmental considerations. We explore these geometric considerations in greater detail in [48].

In each of the devices described in this dissertation, the system had an under-filled viewing geometry such that they are both limited by the illuminated area in the scene

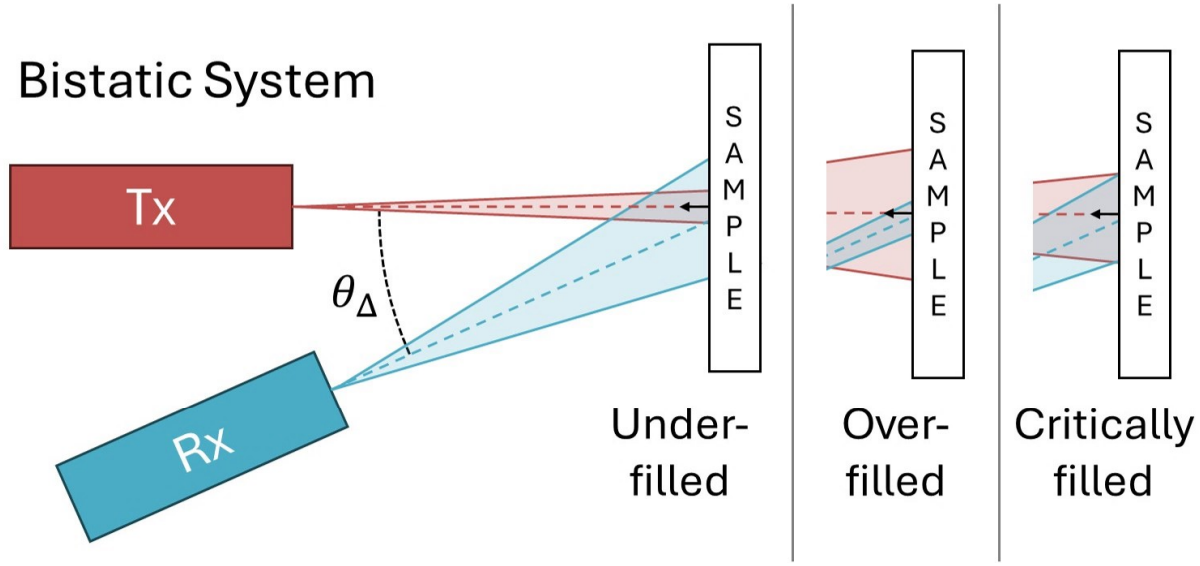


Figure 7: A representation of a bistatic active remote sensing system. The FOV solid angle, Ω_{FOV}, is represented by the blue shaded region, and the solid angle subtended by the sample's projected illuminated area, Ω_{ill}, is represented by the red shaded region. Also of note, for bistatic systems with large separation angles, θ_Δ, should place their transmitter or receiver normal to the panel.

($\Omega_{sc} = \Omega_{ill}$).

3.1.2 Lambertian Reference Surfaces

The biconical reflectance term in Eq. 23 is the discrete and practical form of reflectance which is related to the BRDF as

$$\rho_{cc} = \frac{1}{\Omega_i^P} \int_{\Omega_i} \int_{\Omega_v} f_r(\omega_i, \omega_v) \; d\Omega_v \; d\Omega_i. \tag{26}$$

When f_r is constant, the integral form of the equation can be reduced to a linear form.

$$\rho_{cc} = \Omega_v^P f_r \tag{27}$$

$$f_r = \frac{\rho_{cc}}{\Omega_v^P} \tag{28}$$

The BRDF is constant for Lambertian reflectors, and for most reflectors over very small viewing solid angles. The latter is the case for our active polarimeters generally, and the Lambertian case can be leveraged to determine the calibration functions.

A highly diffuse surface, such as sintered polytetrafluoroethylene (PTFE), comes as close to an ideal Lambertian surface as can be manufactured under realistic constraints. A Lambertian surface is defined as having constant radiance, L $[\frac{W}{m^2 sr}]$, over all of its angles and areas. From this definition, we can extend that an ideal Lambertian surface has the constant BRDF,

$$f_r^L = \rho_{cc}/\pi. \tag{29}$$

3.1.3 Reflectance Relative Calibration Function, K

For detectors operating in their linear region, the measured signal, V, is proportional to the radiance within the FOV solid angle. Combining this relationship with Eqs. 21, 22,

25, and 28, we can establish

$$\Delta L_r = CV(\omega_v) = f_r(\omega_i, \omega_v) * (T_{sys}T_{atm})\Delta E_0 \cos(\theta_i). \tag{30}$$

We can rearrange the second and third portions of the equation to acquire the form of the calibration relationship.

$$f_r(\omega_i, \omega_v) = V(\omega_i, \omega_v)\left[\frac{C}{T_{sys}T_{atm}\Delta E_0 \cos(\theta_i)}\right] = V(\omega_i, \omega_v)K(\omega_i, \omega_v) \tag{31}$$

This leaves C as the calibration function capturing responsivity and the like, and $T_{sys}T_{atm}\Delta E_0$ as the terms which would result in a calibration function for the transmitter in a given setup. K is therefore the combined relative calibration function for the system.

$$K(\omega_i, \omega_v) = \frac{C}{T_{sys}T_{atm}\Delta E_0 \cos(\theta_i)} \tag{32}$$

3.2 Procedure

The reference calibration method takes a measurement of a Lambertian reference, such as a Spectralon or other sintered PTFE panel, and uses that measurement to normalize returns from other surfaces of interest. Combining Eqs. 29 and Eq. 42, we find an expression relating known f_r and measured V,

$$f_r^L = \frac{\rho_{cc}}{\pi} = V_{ref}K = V_{ref}\left[\frac{C}{T_{sys}T_{atm}\Delta E_0 \cos(\theta_i)}\right], \tag{33}$$

where V_{ref} is the measured electrical signal for the reference measurement. While we can generally assume ΔE_0 and T_{sys} are stable constants, and that T_{atm} is a stable constant for a

controlled environment and similar ranges, K remains a function of θ_i.

$$K(\theta_i) = K_0 \cos^{-1}(\theta_i) \tag{34}$$

There may be use cases where K must be determined as a function of additional variables previously assumed to be constants, but the form of the equation in those instances should be easily derived from Eq. 35 using a similar process.

When a measurement of a Lambertian reference is taken while aligned at normal incidence, we can rearrange Eqs. 35 and 34 so the known values give a simple solution for K_0.

$$K_0 = \frac{\rho_{cc}}{\pi V_{ref}} \tag{35}$$

No real diffuse reference behaves perfectly Lambertian at all angles, and PTFE samples have been shown to behave most Lambertian at normal incidence or normal viewing [2, 49, 50]. Therefore, the reference measurement should be taken with the Lambertian reflector at as near normal incidence (θ_i of 0°) as possible.

To apply the calibration, we can simply plug $K(\theta_i)$ back into Eq. 42.

$$f_r(\omega_i, \omega_v) = V_{sig}(\omega_i, \omega_v) K(\theta_i) \tag{36}$$

3.2.1 Calibration Procedure Summary

The procedure for the Lambertian reference calibration method is summarized as follows:

1. Determine the potential variables from ΔE_0, T_{sys}, T_{atm}, and θ_i, deriving the appropriate function for K using those variables (as demonstrated for a single variable in Eq. 34).

2. Select a Lambertian reference panel of similar reflectance, ρ_{cc}, to your active remote sensor system's intended scenes.

3. Measure V_{ref} (proportional to the power reflected by the reference) by taking a measurement of the Lambertian reference at surface-normal incidence, $\theta_v = 0°$, and taking note of any initial variable values for the function determined in step 1.

4. Determine the appropriate K_0 value for your relative calibration by plugging in the known initial and measured values to the function determined in step 1.

5. Apply the relative calibration to measurements using the form of equation modeled by Eq. 36.

3.3 Experimental Validation

To validate this reflectance relative calibration method, we compared it to an alternate method for achieving normalized reflectance values based on a direct measurement of the transmitted and received powers.

3.3.1 Alternate Reflectance Normalization Procedure

The method used for comparison relies on precisely measuring the transmitter output power and determining the system's FOV solid angle. To find the system's Ω_{FOV}, we can either calculate using measurements of the receiver optical train or by measuring Ω_{FOV} using a pinhole and rotation mount centered at the optical train's nodal point. For these validation data, we calculated from measured and reported values using Eq. 21, assuming the detector active area is located at the back focal plane of the optical train.

Measuring the transmitter output power, P_i, at normal incidence and relative to the receiver's optical efficiency, η, results in the electrical signal, V_{sig}, we would expect for $f_r = 1$. We will refer to this electrical signal as V_{max}, and it is directly proportional to ΔE_0. This measurement is performed simply by directing the transmitter entirely into the receiver,

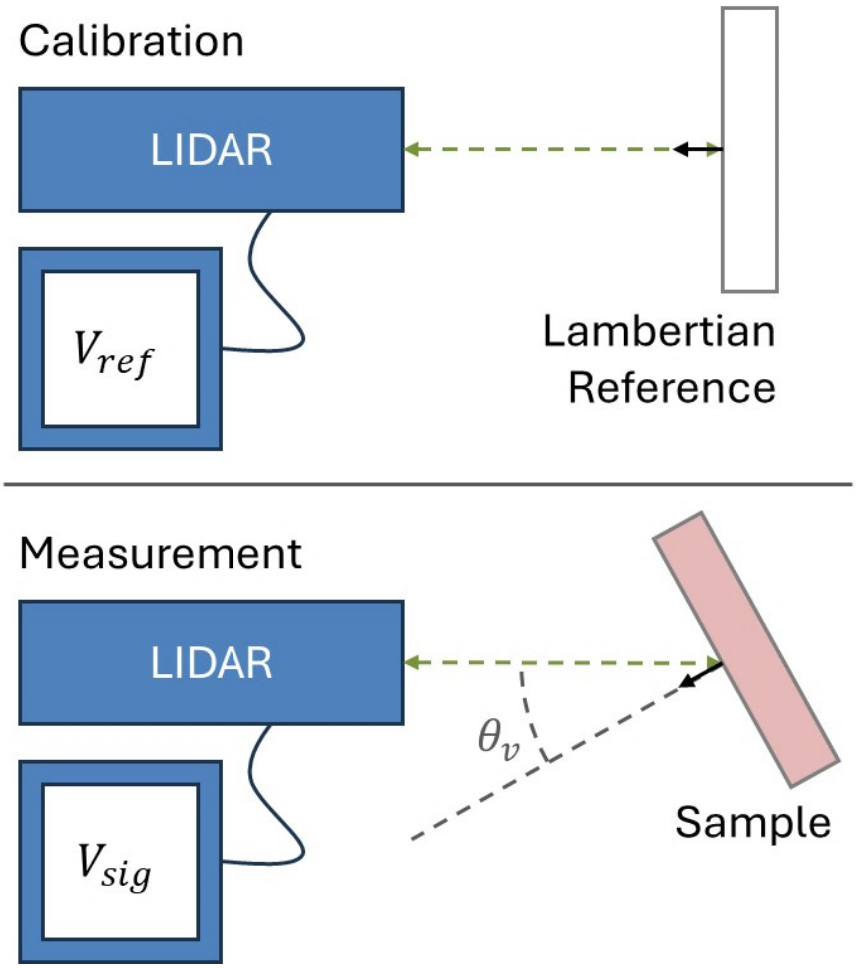


Figure 8: Overview of the Lambertian reference calibration method applied to a monostatic lidar system (or other active remote sensing system). The calibrating measurement (top) of the Lambertian reference with known reflectance, ρ_{cc}, is performed with the reference panel at normal incidence to the lidar optical path. The sample measurements (bottom) can then be taken at any measured incidence angle. The measured V_{ref} value would be used with Eqs. 34 and 36 in this case, turning the measured signal voltage, V_{sig}, into a BRDF value, f_r^m, at the given viewing angle, $\theta_v = \theta_i$.

either by splitting the two arms of the active remote sensor apart, or by using a high-fidelity mirror.

In the case of the data presented here, the transmitter power was much higher than could be measured in the linear response region of the receiver. For cases such as these, we can implement neutral density (ND) optical filters which have been calibrated at the wavelength of interest. These filters reduce the optical power from the transmitter which reaches the receiver by a known order of magnitude (e.g., an ND filter with a value of 1.0 reduces the optical power by a factor of 10). We can thereby artificially extend the region of linearity to a hypothetical V_{max}.

For an illuminated sample at a specific wavelength, the radiance reflected from leaving the surface can be redefined as

$$L_r(\omega_{\mathbf{i}}, \omega_{\mathbf{v}}) = \frac{P_d(\omega_{\mathbf{i}}, \omega_{\mathbf{v}})}{A_{ep}\Omega_{sc}} = \frac{P_d(\omega_{\mathbf{i}}, \omega_{\mathbf{v}})R_{sc}^2}{A_{ep}A_{sc}^P}, \tag{37}$$

where P_d is the optical power falling on the detector. Given $\Delta E_0 = P_i/A_{sc}^P$, where P_i is the optical power incident on the illuminated sample and assuming an under-filled geometry (as in the systems discussed in this dissertation), we can combine Eqs. 19, 21, and 37.

$$f_r(\omega_i, \omega_v) = \frac{P_d(\omega_i, \omega_v)}{P_i\Omega_{FOV}\cos(\theta_v)} \tag{38}$$

The incident power, P_i, can be represented by ηV_{max}, where η is the efficiency of detector $[\frac{V}{W}]$. Similarly, the detected power, P_d, can be represented by ηV_{sig}, where V_{sig} is the signal voltage returned for any given measurement. We can therefore rewrite Eq. 38 to consider received electronic signals to their BRDF values at given geometries as

$$f_r(\omega_i, \omega_v) = \frac{V_{sig}(\omega_i, \omega_v)}{V_{max}}\frac{1}{\Omega_{FOV}\cos(\theta_v)}. \tag{39}$$

In summary, the procedure for this normalization method we use as a comparison is as follows:

1. Determine the Ω_{FOV}, typically by measuring the detector active area and the distance between the detector and lens (or lens system exit pupil).

2. Measure V_{max} (proportional to transmit beam power) by firing the transmitter into the receiver, either directly or using a high-quality mirror, and possibly using ND filters to extend the detector's effective linear response region.

3. Measure V_{sig} (proportional to the reflected power) with the transmitted beam reflected from the sample (and the receiver back in its usual configuration if it was moved in the previous step).

4. Apply V_{sig}, V_{max}, and θ_v to Eq. 39 to determine the BRDF.

3.3.2 Data Collection

The active polarimeter system was composed of a transmitting 1064-nm laser (Edmond Optics, 10 mW DPSS Pointing Laser #37-043) and a receiving InGaAs variable-gain photodiode (Thorlabs PDA10CS2), a 10-nm bandwidth laser line filter centered at 1064 nm (Thorlabs FLH1064-10), and a 50-mm focal length lens (Newport KPX082) with the focal plane at the detector active area. The sensor-sample distance was 1.575 meters, and the receiver and transmitter were separated such that the fixed separation angle, θ_Δ, was approximately 3°. The beam diameter at the sample was 8 mm, and with a receiver FOV of 1.13° (full angle), the geometry satisfied the under-filled FOV expectation. The specific instrument used to make these measurements had full polarimetric capability, which was used to determine the unpolarized reflectance as the m_{00} element of the calculated Mueller matrix [2].

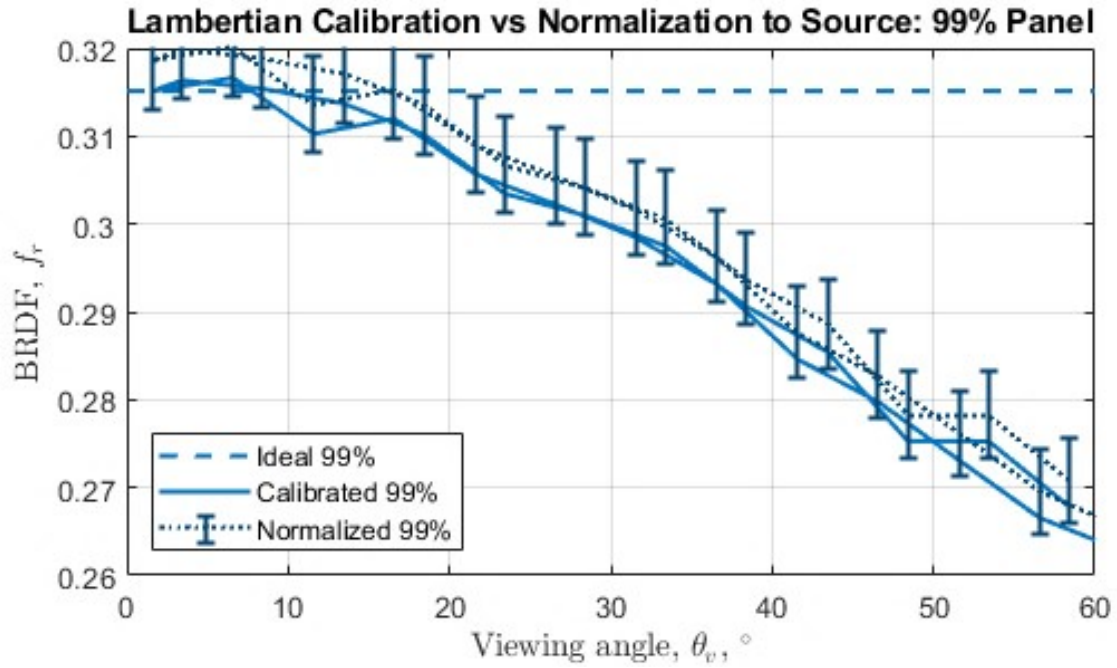


Figure 9: A plot of $f_r(\theta_v)$ for a 99% Spectralon® panel. The trend away from an ideal Lambertian response at increasing θ_v is as expected, and the reference method produced normalized results closer to the expected reflectance near normal θ_v and within the tolerance of the normalized results.

The device was used for both the procedures in Section 3.2.1 and Section 3.3.1. A 99% reflectance Spectralon® panel was measured at normal incidence for the reflectance relative calibration method. The laser was fired into a mirror and reflected into the receiver through ND filters (4.7106 OD at 1064 nm) to record a maximum signal, V_{max}, for the alternate normalization method.

3.3.3 Data Comparisons

The validating data are presented in Figs. 9 and 10. The data presented are on the same vertical scale, although they are on different parts of the vertical axis. Each figure shows data measured with a nearly monostatic laser and receiver (separated by 3° or less) and the viewing angle was varied by tipping the Spectralon panel with respect to the system

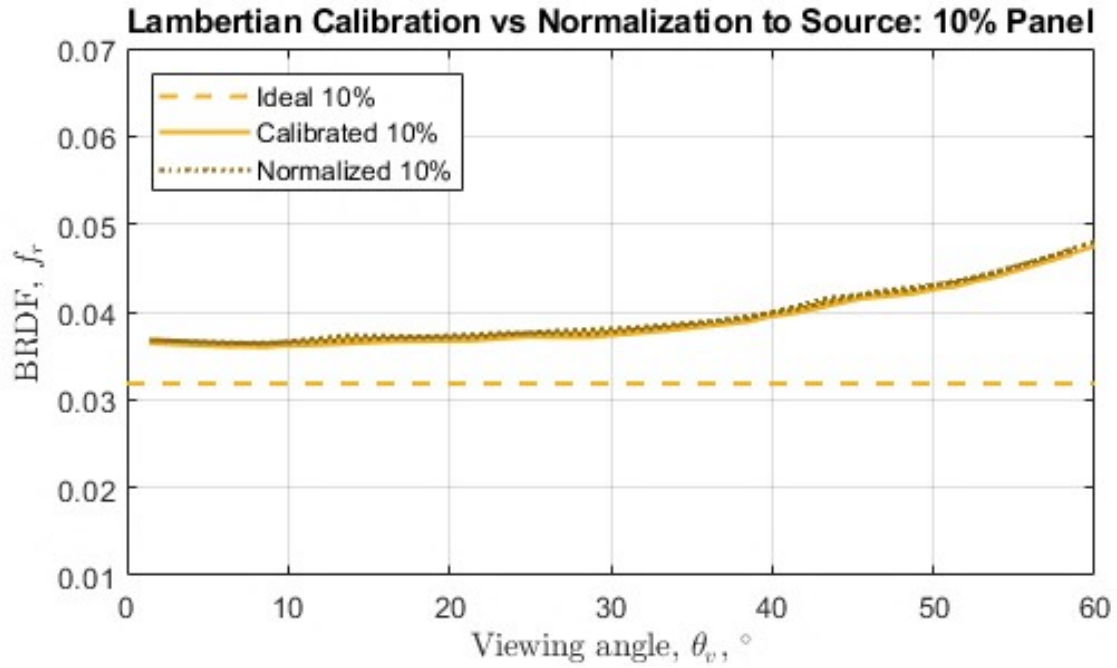


Figure 10: A plot of $f_r(\theta_v)$ for a 10% Spectralon® panel. At these lower ρ_{cc} values, the BRDF actually increases at larger θ_v, perhaps due to an increased prevalence of single-scattering events [2].

optical axes. The two solid lines in each figure show the measurements at each viewing angle calibrated with the normal-incidence reading (one for tipping toward "positive" angles and one for tipping toward "negative" angles). Similarly, the two dotted lines show measurements at each viewing angle normalized with the direct power readings. The horizontal dashed line in each figure shows the ideal Lambertian response, a constant ρ_{cc}/π, for the panel's nominal reflectance.

The meaning of these data are discussed in greater detail in [2], but there are two primary things to note here. First is the systematic variation of the measurements with viewing angle. As shown and discussed more elsewhere [2], the measurements produce BRDF values that fall off with viewing angle for the high-reflectance panel (Fig. 9) and that rise with viewing angle for the low-reflectance panel (Fig. 10). The second thing to note is the close agreement of values derived using the reflectance relative calibration and the Tx-power normalization method, which provides confirmation of the relative calibration method. The root-mean-squared error (RMSE) of the relative calibration as compared to the more direct normalization method with the 99% and 10% reflectance cases are 0.0031 (0.99%) and 0.00042 (1.3%), respectively.

In comparing the two methods, however, it is important to note that the normalization method actually has higher uncertainty than the relative calibration performed with a Lambertian panel. The most prominent error for the normalization method came from the Ω_{FOV} measurement. In our case, a 0.5-mm uncertainty in receiver lens position relative to the detector translates to a 0.01° uncertainty in the full-FOV angle, and ultimately results in the approximately 1.8% uncertainty displayed with the error bars in Fig. 9.

On the other hand, the most prominent error for the relative calibration was a misalignment of the reference panel from normal θ_v. We mounted the panels on a rotation stage on the same optical table as the reflectometer, with a rotational uncertainty of 1°. This uncertainty equates to about 0.02% in the normalized result, which is not shown in error

bars in Fig. 9 because they are indistinguishable from the line at the plotted scale. From Fig. 9 we see that it would take a misalignment of the normal-incidence measurement of the panel by 10° or more to introduce a systematic error as large as the uncertainty in the direct-power normalization method.

Variations in the V_{max} or V_{ref} measurements are other sources of potential uncertainty, but time-averaging over long periods (10 minutes or more) can reduce these uncertainties to near insignificance in comparison to geometric uncertainties.

3.4 Discussion

The reflectance relative calibration method presented in this chapter is useful for a wide variety of active remote sensor systems, and can be generalized for measurement scenarios with multiple variables, such as changing T_{sys} or T_{atm}. Compared to a method of determining reflectance by normalizing to the transmitter output power, the relative calibration more easily matches scene parameters expected for diffuse reflectors and has improved precision due to lower uncertainty propagation into the calibration function.

Given the validation data, we recommend the reflectance relative calibration over the compared normalization method in most cases where a near-Lambertian reference is available. A reference panel would need to have misalignment uncertainty of more than 10° in its tilt relative to the remote sensor system to produce the same uncertainty as was seen for the 99% panel using the Tx-power normalization (Fig. 9).

Potential detector damage is a major concern with firing the transmitter into the receiver for the normalization method, though it can be overcome by implementing neutral density (ND) optical filters when taking the V_{max} measurement. This requires accounting for the ND filters' attenuation of the transmitter power, however, which introduces another layer of uncertainty to the calibration function.

These data and methods are meant primarily for monostatic or near-monostatic ($\theta_{\Delta} <$

10°) systems. It should be noted that for a bistatic system illuminating a reference panel at near-normal incidence with a receiver pointed at a larger viewing angle, the panel will give a more Lambertian behavior over a larger range of viewing angles than is suggested by our figures.

CHAPTER FOUR

NON-RANGING MATERIAL P-MBRDF CHARACTERIZATION

4.1 Methods

Using the simple polarimeter described in Ch. 2, P-mBRDF measurements were taken for a variety of samples. Samples were mounted vertically on the sample rotation stage shown in Fig. 11. Throughout the measurements, we changed the incidence and viewing angles of the polarimeter, θ, by rotating the stage. An overhead schematic of the rotation geometry is shown in Fig. 12, as presented in [1]. The data were recorded as electrical signals and reported as BRDF values following the calibration method discussed in Ch. 3.

4.2 Lambertian References

The first measurement presented is the 99% Spectralon reference, the results of which are shown in Fig. 13. Given the system defined with angle of polarization orientation (AoP) set to 0° vertical, and that the samples are rotated about the vertical axis, we expect to see – and do observe – a slight increase in magnitude toward -1 for both the m_{01} and m_{10} coefficients, which represents the increasing polarizance of an isotropic surface at glancing angles [26, 51]. Also expected, the off-diagonal coefficients are significantly smaller than the diagonal coefficients of the Mueller matrix because the Spectralon is primarily depolarizing by random scattering, not preferentially rotating linear states or altering ellipticity.

We also used the initial polarimeter design to characterize the P-mBRDF response of multiple Spectralon panels of varying reflectance [2]. For that work, we received mBRDF data from the Air Force Research Laboratory for that work to compare to our own measurements of a 99%, 50%, 30%, and 10% reflectance reference; these comparisons gave rise to the

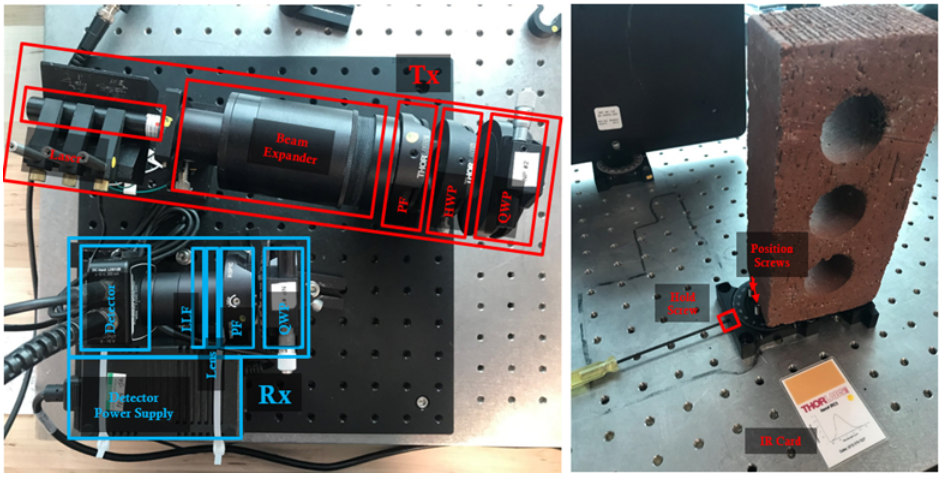


Figure 11: The simple near-monostatic Mueller polarimeter. The overhead view is labelled with system components and the red clay brick sample is shown on the sample rotation stage used to control θ_v.

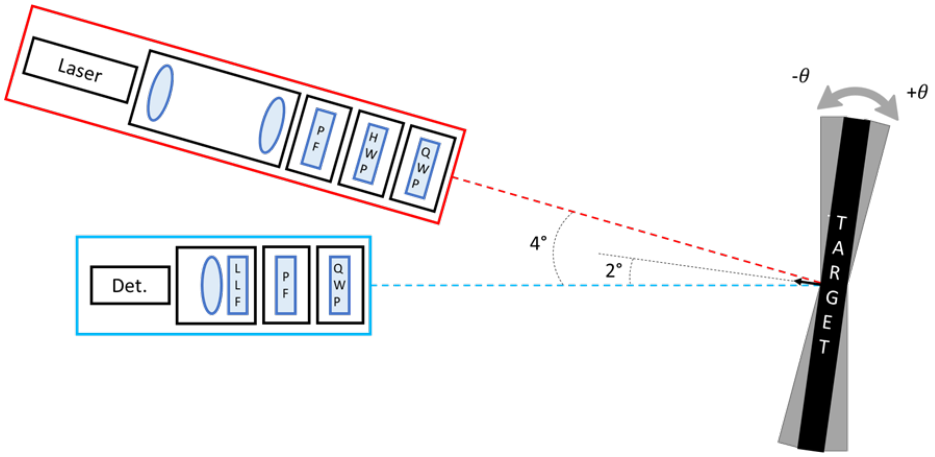


Figure 12: The P-mBRDF measurement geometry, not to scale. A 0° incidence/viewing angle is defined when the surface normal of the target is 2° from the optical paths of both the transmitter and receiver. Rotating counterclockwise (surface normal toward the receiver) is the negative angular direction, while rotating clockwise (surface normal toward the transmitter) is the positive angular direction.

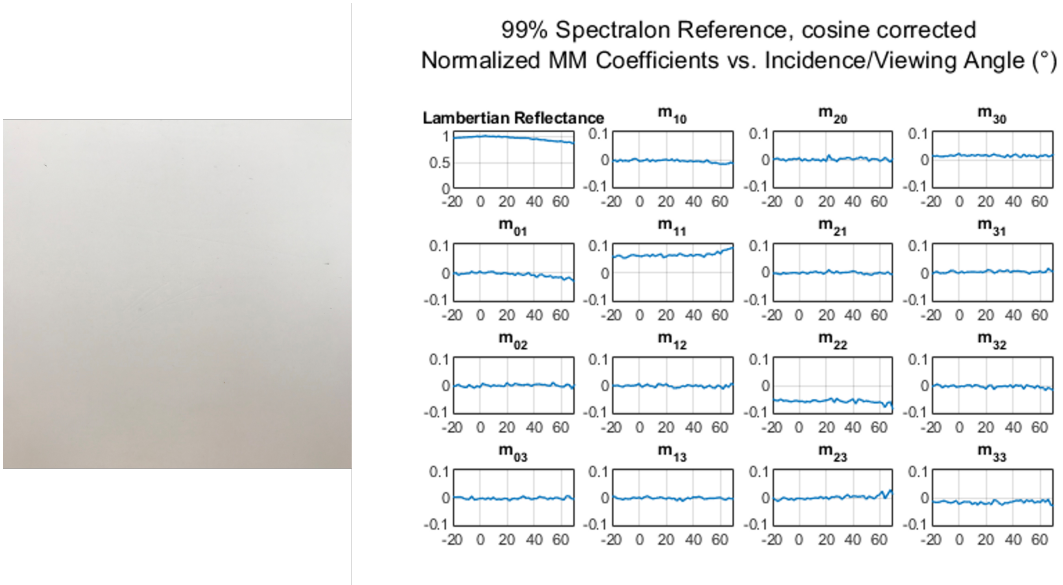


Figure 13: An image of the sample Spectralon surface (left) and the resulting P-mBRDF measurement over a fine scan of θ (right).

reflectance relative calibration function discussed in Ch. 3. Our mBRDF values are the unpolarized m_{00} coefficients of the also-reported P-mBRDF of the samples.

As compared to the nominal mBRDF for their reflectance labels, the reference panels generally showed smallest errors near surface-normal incidence, as expected [2]. The mBRDF errors from ideal Lambertian reflectors show a broad trend of increasing error with increasing reflectance, though the 10% reference did show increased error over the 30% reference. These error data are summarized in Fig. 14.

As a qualitative analysis of the data in Fig. 15, the higher-reflectance panels show mBRDF falling below the ideal as the incidence angle increases, while lower-reflectance panels seem to show the opposite, with mBRDF rising above the ideal as incidence angle increases. These trends combine to suggest that there should be some reflectance at which deviation from the ideal is at a minimum. Of the panels which were measured, the 30% panel has the lowest RMS error from the expected ideal, but the 50% panel has the flattest response across incidence angles. In fact, if we instead take the nominally 50% panel to have

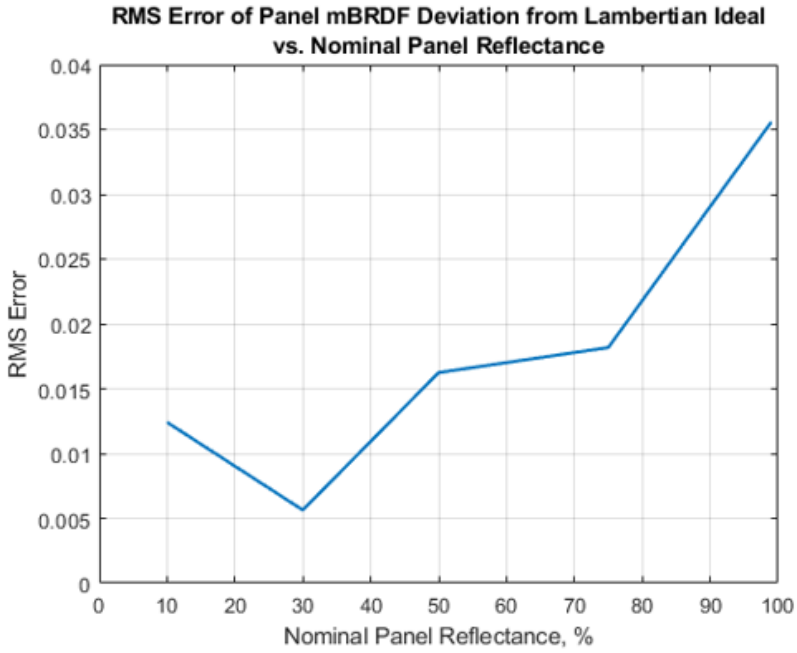


Figure 14: Average RMS error of measurements as compared to ideal Lambertian mBRDF by reference nominal reflectance.

reflectance of about 55%, its RMS error is reduced to 0.003, which would be the lowest of any of the measured panels.

The Mueller matrix plots of the 99%, 50%, 30%, and 10% panels are presented in Figs. 16 through 19. Each of the reported P-mBRDF coefficients reported is the average of three or more datasets taken at different locations on the same panel. The maximum deviation of a given dataset from the average for any panel measurements presented is $\pm 2.5\%$.

The results of these P-mBRDF measurements did not provide significantly novel insights, but helped to validate the system nonetheless. The diagonal coefficients are greater in magnitude than the off-diagonals, which are all about 0 for most angles, and the diagonal coefficients increase with decreasing reflectivity due to reduced multiple scattering depolarization. Though it can be difficult to see in the Mueller matrix plots, the polarizance does increase as reflectivity decreases (see Fig. 20), in accordance with the Umov effect.

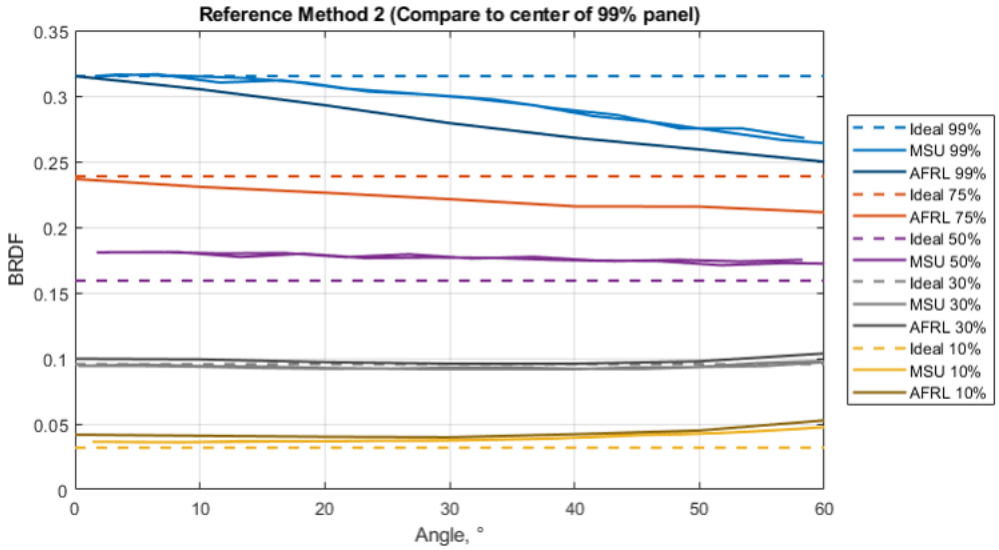


Figure 15: Plot of Spectralon reference mBRDF returns as compared to the ideal for a Lambertian reflector of the reference panel's nominal reflectance. These data are calculated using a relative reflectance calibration as described in Ch. 3.

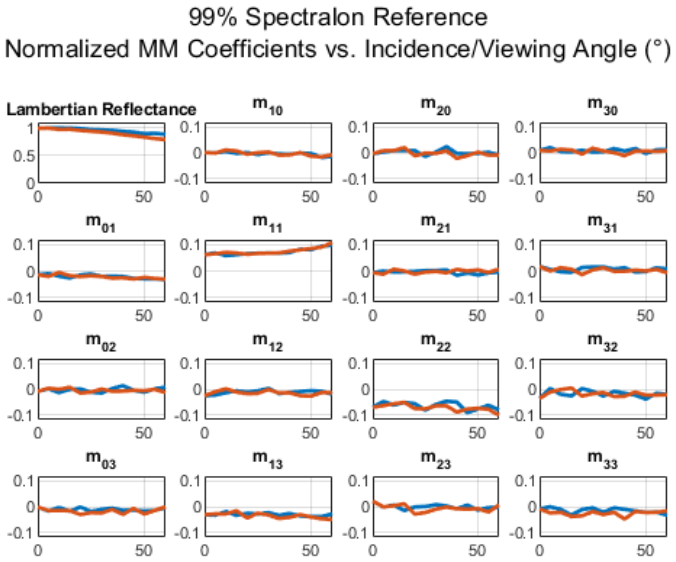


Figure 16: A second, broader set of measurements of a 99% Spectralon reference, which can be compared to the former measurement shown in Fig. 13. The blue line shows positive θ values while the red line shows negative values.

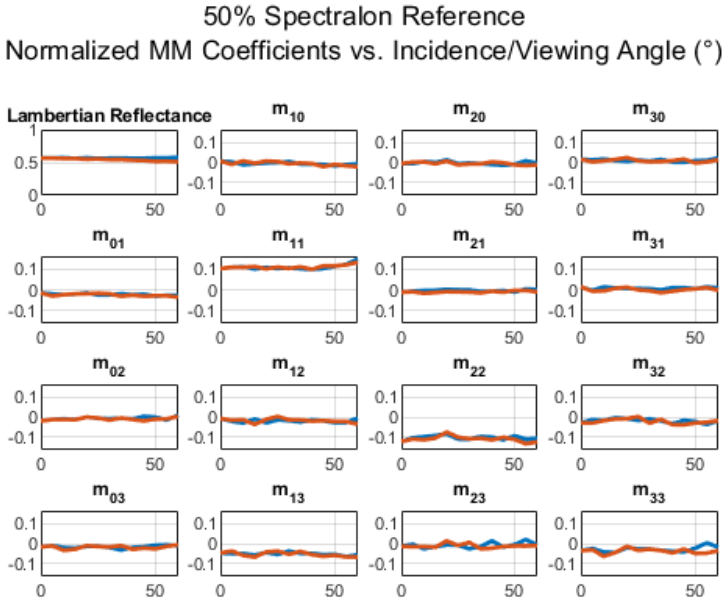


Figure 17: P-mBRDF measurements of a 50% Spectralon reference. The blue line shows positive θ values while the red line shows negative values.

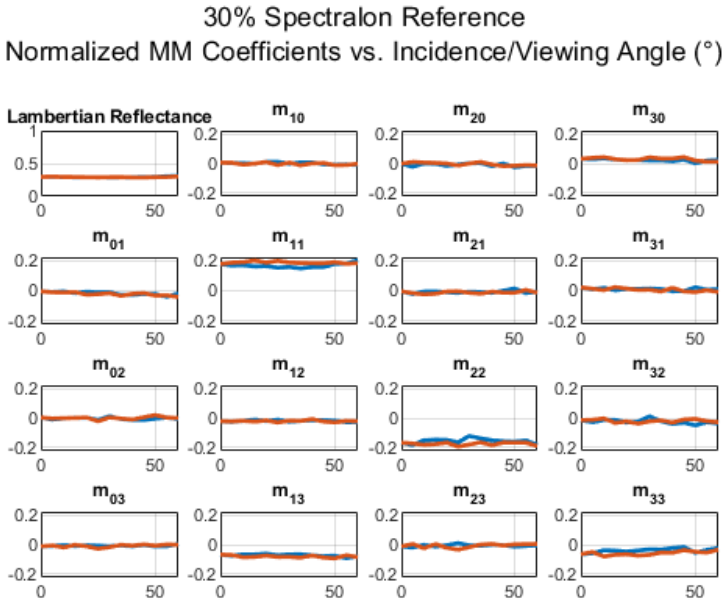


Figure 18: P-mBRDF measurements of a 30% Spectralon reference. The blue line shows positive θ values while the red line shows negative values.

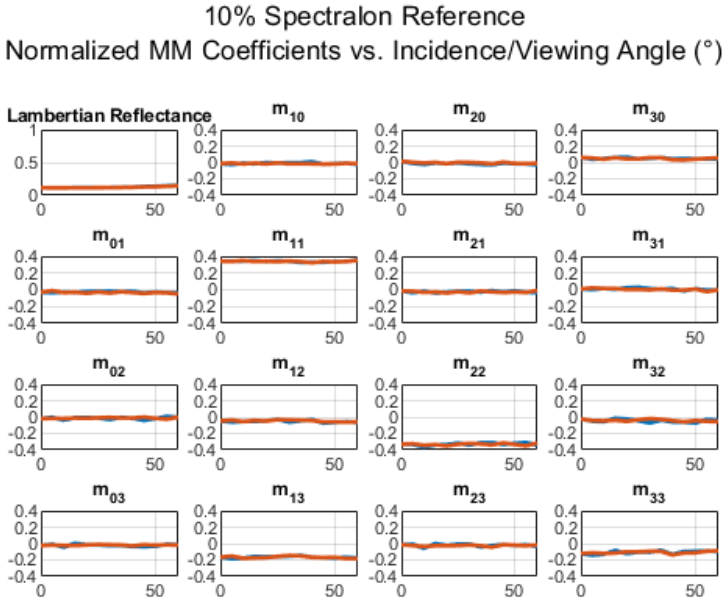


Figure 19: P-mBRDF measurements of a 10% Spectralon reference. The blue line shows positive θ values while the red line shows negative values.

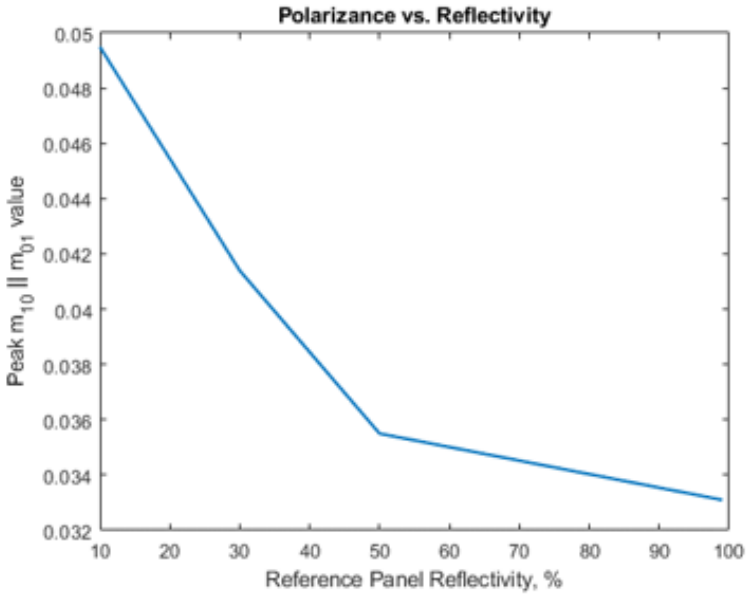


Figure 20: The polarizance, as represented by the magnitude of m_{01} or m_{10}, as a function of nominal panel reflectance.

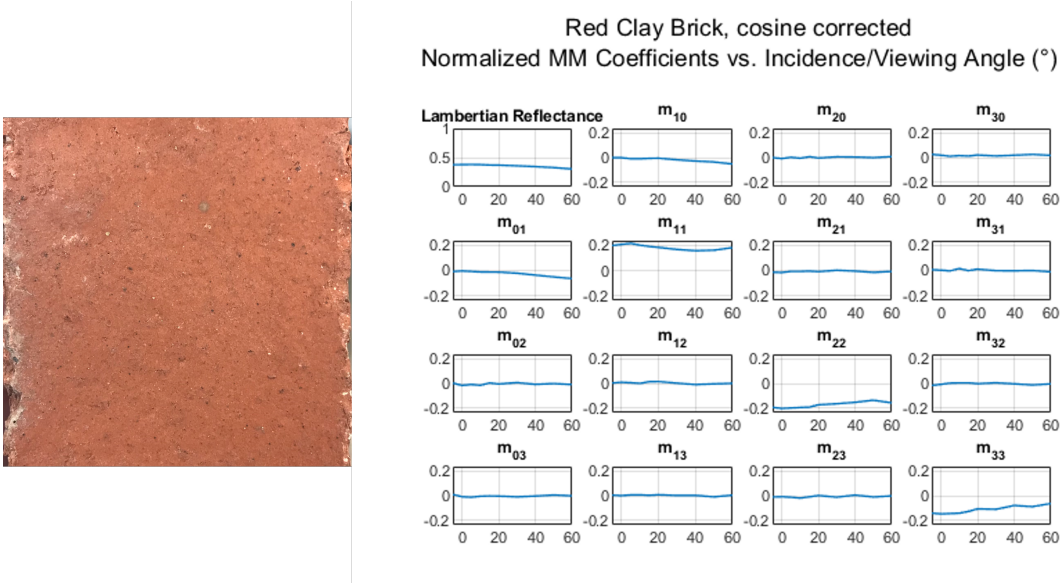


Figure 21: An image of the sample brick surface about the measurement location (left) and the resulting P-mBRDF measurement (right).

4.3 Urban Materials

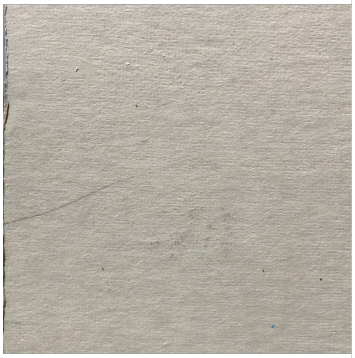
In addition to the well-characterized PFTE references, we also measured a number of common urban materials, including a brick, sheetrock, plain steel, and a shingle. The results of the red clay brick are shown in Fig. 21. The material was relatively matte, so a largely Lambertian response was expected. The response was similar to that of the PFTE references, based on the flatness of the reflectance, the much greater magnitude of the diagonal coefficients as compared to the off-diagonal coefficients, and the increase in magnitude of m_{01} and m_{10} with increasing θ. As the quasi-Lambertian reflectance of the brick at 1064 nm was middling, the greater increase in magnitude of m_{01} and m_{10} was justified by the Umov effect. The brick, unsurprisingly, did not show any birefringence or polarization rotation.

An image of the reference sheetrock and measured P-mBRDF are given in Fig. 22. Unlike the PFTE references and clay brick, the unpainted sheetrock was somewhat glossy, which gave it a reflectance behavior between specular and diffuse. Nearer the 0°

incidence/viewing angle, the reflectance and polarization maintenance (magnitude of the diagonal coefficients) were greater than at more oblique angles. The only other apparent feature is the inverse relation between m_{23} and m_{32}, which would be sensible for a birefringent material. Thin films of different materials can sometimes cause a very slight degree of birefringence, which would be the likeliest scenario for sheetrock with a finishing layer.

Plain milled steel served as our near-specular sample. Its measurement results are shown in Fig. 23. The (relative) Lambertian reflectance peaked very strongly near 0° incidence/viewing, but falls off very quickly afterward. As a largely specular surface, the steel was very strongly polarization maintaining, with the diagonal Mueller coefficients approaching magnitudes of 1. The steel showed some glancing angle diagonal polarizance and diattenuation (shown by the increase in magnitude of m_{20} and m_{02}, respectively), and curiously showed some glancing angle birefringence as well, as evidenced by the increase in magnitudes of m_{03} and m_{30} along with the diagonal linear polarization effects. These slight diagonal and circular tendencies at glancing angles are novel and not well explained, but they are also within the error tolerance of original simple polarimeter that took the measurements, so they may also be a measurement artifact.

Of the urban surfaces characterized, the tar-fiberglass roofing shingle was the least in-line with expected Lambertian or specular surface responses. The shingle consisted primarily of 1- to 3-mm diameter rough fragments of tar overlaying a thin layer of fiberglass insulation which was still visible through the surface. The reflectance was fairly Lambertian, at least in line with the brick sample's degree of Lambertian quality if not more so. Likely due to the more anisotropic structure of the shingle surface, the polarizance of the shingle did not increase significantly with increasing θ as compared with other samples measured, despite its lower reflectance. We would also expect a rough surface to be more limited in polarization maintenance, but we instead saw much increased polarization maintenance for this material. To first degree, this increase in the diagonal coefficients may be due to the



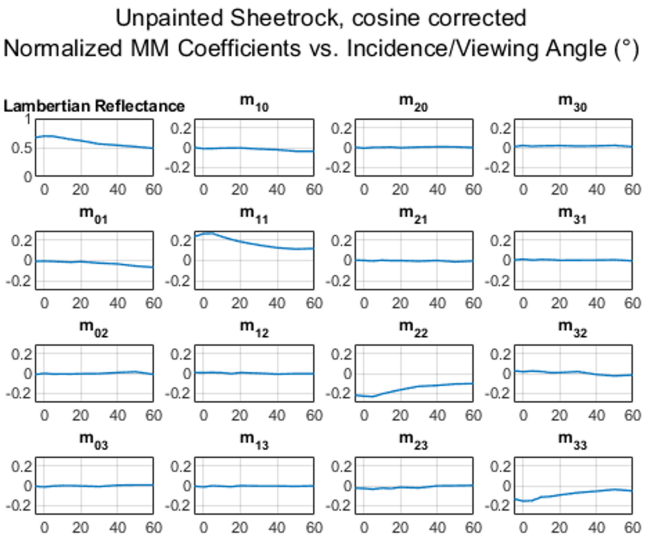


Figure 22: An image of the sample plain, unpainted sheetrock surface (left) and the resulting P-mBRDF measurement (right).



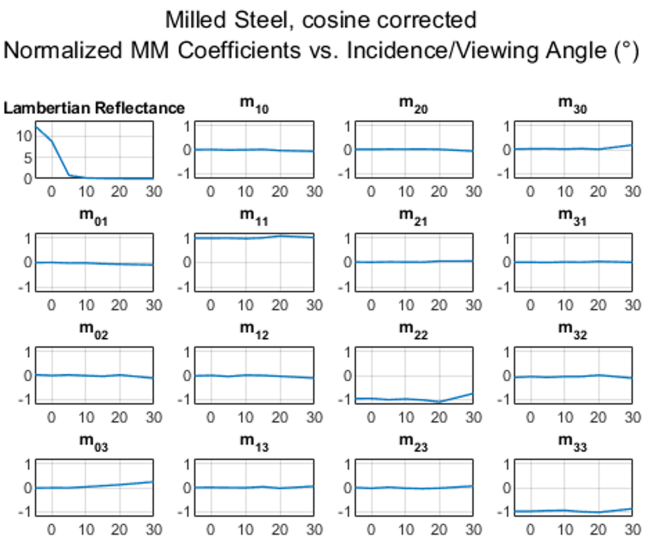


Figure 23: An image of the sample milled steel surface (left) and the resulting P-mBRDF measurement (right).

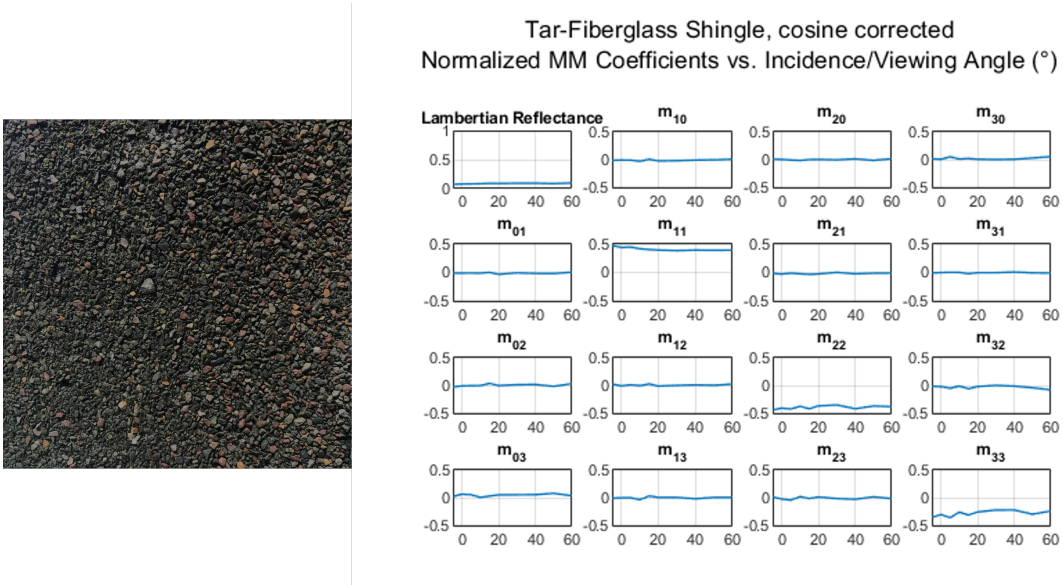


Figure 24: An image of the sample tar roofing shingle which includes fiberglass insulation (left) and the resulting P-mBRDF measurement (right).

darker surface reducing multiple scattering depolarization, but it is difficult to decipher the exact mechanism for such a complex sample's response.

While this small set of urban samples show that P-mBRDF characterization by even a simple polarimeter can be validated, the response of the complex tar shingle sample is more difficult to theorize. This concept reinforces the rationale behind the simple polarimeter presented in Ch. 2: to expand the knowledge base of geometrically-resolved polarimetric responses from materials in the monostatic or near-monostatic domains common among lidar and other active remote sensing systems.

CHAPTER FIVE

DICHROIC MUELLER PULSED LIDAR (DMPL) TESTBED

5.1 Contribution of Author and Co-Author

Manuscript in Chapter 5

Author: Nathaniel J. Field

Contributions: Conceptualization, Data acquisition and analysis, System design, build, and assessment, Writing – original draft

Co-Author: Joseph A. Shaw

Contributions: Conceptualization, Funding acquisition, Project administration, Resources, Supervision, Writing – review and editing

5.2 Manuscript Information

Nathaniel J. Field, Joseph A. Shaw

Optical Engineering

Status of Manuscript:
____ Prepared for submission to a peer-reviewed journal
_X_ Officially submitted to a peer-reviewed journal
____ Accepted by a peer-reviewed journal
____ Published in a peer-reviewed journal

SPIE Publishing Group
Submitted: 04 April 2025

5.3 Abstract

We describe the design and implementation of a dichroic Mueller pulsed lidar (DMPL) testbed. Operating at 532-nm and 1064-nm wavelengths simultaneously, the polarimetric lidar returns a full set of range-resolved Mueller matrix elements after a measurement period of just under 3 minutes. The instrument is designed as a source of reference measurements to produce proof-of-concept and high-fidelity scene models for the validation of a wide variety of other, more complex polarimetric lidar systems. Polarimetric optimization, careful alignment, and radiometric calibration achieve theoretical Mueller coefficient errors of no more than 2.04%. Initial measurements show expected polarimetric features for samples characterized in existing literature and a vast majority of measured coefficients well within the theoretical maximum error; the mean observed Mueller coefficient error across multiple scenarios was 0.86%.

5.4 Introduction

Machine vision can exploit polarimetric optical sensing as an added dimension beyond intensity and color for applications such as automated vehicles, military sensing, atmospheric monitoring [3–9]. Such polarization-enhanced remote sensing has been used in both passive and active systems, though there is more literature regarding its passive system applications [3, 9]. Passive remote sensing systems benefit from low power consumption due to a lack of an illumination source, but active polarimeters can generate a wider variety of polarized illumination states to more fully characterize a sample or scene than would be possible with only passive measurements of the natural light.

One type of polarization-enhanced active remote sensing system – dual-polarization light detection and ranging (lidar) – transmits a single polarization state (typically linearly polarized) and has receivers for both that state and the orthogonal state. To show the variety

of scenarios for which this is useful, a small selection of dual-polarization lidar applications include: detecting the thermodynamic phase of clouds [13], detecting honeybees in flight [11], detecting vehicles concealed by foliage and other vegetation [12], and locating invasive lake trout from the air [14, 15]. The seminal work in dual-polarization lidar actually began with noting changes in depolarization of clouds and melting snowflakes [16, 17]. This led to further studies on depolarization effects in the atmosphere, especially concerning ice crystals and cloud make-up [18, 19]. A push from the previous linear-only polarimetry to full Stokes measurements led to the conclusion that dual-polarization measurements were the most efficient means of characterizing atmospheric effects [20]. The standard notation and theory of dual-polarization lidar operation was published in 2008 [21] and complete theoretical explanation of polarimetric lidar derived from Stokes vectors and Mueller matrices was published four years later [22].

However, for active polarimetric sensing of solid objects instead of distributed atmospheric scattering, the question remains open as to the most effective transmit and receive states for polarization-enhanced active remote sensors for various applications. Despite – or perhaps because of – the prevalence and broad successes of dual-polarization lidar in active optical remote sensing, there has been little exploration into more fully polarimetric lidar. Previous research in full-polarization lidar has used "Mueller matrix polarimetric imaging lidar" for improved detection of samples submerged in water [23] as well as in two polarimetric approaches to the detection of biological warfare agents [24, 25]. The potential new information available from active Mueller matrix polarimetry has been noted in previous publications, along with some initial work on classifying materials using the polarization bidirectional reflectance distribution function (P-BRDF) in laboratory settings [26–29]. To pursue this capability, The U.S. Air Force Research Laboratory (AFRL) is developing a novel fully polarimetric time-of-flight lidar instrument [4, 30, 31], with the hope that it will provide more information per return than other systems. These complex systems can benefit from

simpler systems for validation and phenomenology studies, which motivated our development of a fully polarimetric lidar testbed. Specifically, the testbed presented here can provide characterization of the monostatic P-BRDF of a sample or scene with high accuracy, then a more complex system that improves on other performance metrics like measurement speed or scanning can use these measurements for critical validation. For atmospheric phenomena considerations, this testbed can be used to later perform volumetric analysis of different conditions, or it can simply be deployed with a complex system in a given set of conditions to serve as validation.

We have a great deal to explore regarding optical polarization properties of objects and scenes beyond the cross-polarization ratio observed in dual-polarization systems. To that end, we recently described a simple polarimeter for near-monostatic characterization of a broad variety of samples [1]. Here we report the extension of that range-independent polarimeter to a Mueller polarization lidar testbed capable of retrieving the full polarimetric response of materials and the range-dependent polarization effects of atmospheric conditions, such as smoke, fog, or precipitation.

5.5 System Design

The dichroic Mueller pulsed lidar (DMPL) aims to provide a relatively simple system to measure polarimetric responses of sample materials and scenes with well-characterized polarimetric accuracy and precision. We explain the fundamental instrument design, the assessment of theoretical polarimetric accuracy, the limitations of measurement rates with high precision, and considerations for testing at variable range windows. A labeled overhead view of the DMPL transmitter and receiver is shown in Fig. 25.

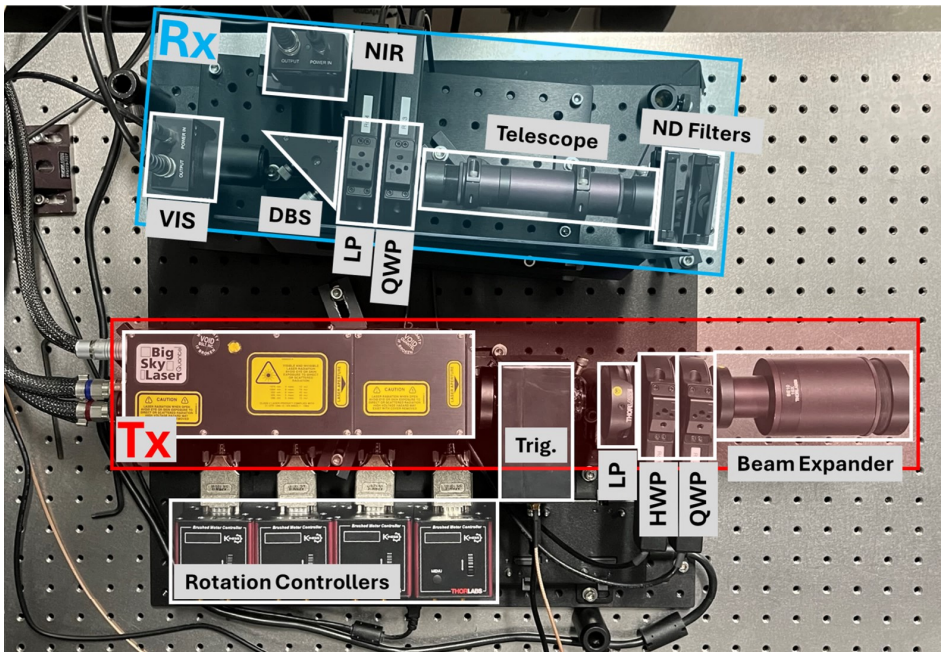


Figure 25: The DMPL transmitter (red) and receiver (blue), mounted on an optical breadboard. This assembly weighs about 16 kg, sufficiently light and rigid to be mounted on a motorized pan-tilt mount with a full range of motion.

5.5.1 Key Components

The fundamental instrument builds on a previously developed non-ranging polarimeter [1, 32], adding a pulsed laser transmitter, avalanche photodiodes (APDs) receivers, a high-speed analog-digital converter for signal acquisition, and a high-speed photodiode as an optical trigger. The transmitter is an ND:YAG pulsed laser (Quantel Ultra) operating simultaneously at 532-nm and 1064-nm wavelengths, with 6.86 ns pulse width (full-width at half-max), 34.6 mJ pulse energy at 532 nm, and 14.6 mJ pulse energy at 1064 nm. The receiver uses a Si APD (ThorLabs APD430A) to collect the 532-nm channel and an InGaAs APD (ThorLabs APD430C) to collect the 1064-nm channel, both of which are specified to have electrical bandwidths up to 400 MHz (rise time of 0.875 ns). The digitizer is a GaGe CSE161G2 with a 1 GS/s sample rate, 16-bit resolution, and 600 MHz electrical bandwidth. The digitizer is externally triggered, and we implemented an optical trigger in the form of a high-speed photodiode (ThorLabs DET025A) viewing side-scattering from the transmitter.

The polarization elements are split into a polarization state generator (PSG) in the transmitter (Tx) and a polarization state analyzer (PSA) in the receiver (Rx). The PSG begins with a linear polarizer (LP) aligned to the laser output major polarization axis, cleaning up the initial linear state with maximum power throughput. After the clean-up polarizer, a rotating half-wave retarder (HWP) rotates the orientation of the linear polarization state without variable attenuation, and a quarter-wave retarder (QWP) can be rotated relative to the HWP to produce any ellipticity in the output polarization state. The PSA consists of a QWP followed by an LP to attenuate signals based on their incident polarization, both in terms of ellipticity and major polarization axis orientation. The HWP is a Meadowlark SAHM-100-420/1100, the QWPs in both the PSG and PSA are Meadowlark DQQ-100-532/1064, and the LPs in both the PSG and PSA are Meadowlark VFR-100-NIR. Each of these elements are mounted in a motorized rotation stage (ThorLabs PRM1Z8) with inter-measurement repeatability of $\pm 0.3^\circ$ ($\pm 0.1^\circ$ for a set of measurements, and $\pm 0.2^\circ$ when the motors are power cycled and homed again).

5.5.2 Polarimetric Accuracy

Assuming reasonable quality polarizers and retarders, optimizing polarimetry relies mainly on the proper selection of PSG and PSA states. Previous literature shows optimal PSG states in an active system are matched to PSA states [42, 43]. Optimal PSA states occur when each of the states is of equal similarity to each of the other states [44, 45]. This is most easily conceptualized as optimization occuring when the coordinates for the PSA states on the Poincaré sphere form the vertices of a platonic solid (tetrahedron, cube, octahedron, dodecahedron, or icosahedron). Because there are only five platonic solids, there are only five possible optimal numbers of measurements for full-polarimetric measurement: four measurements (tetrahedron), six measurements (octahedron), eight measurements (cube), twelve measurements (icosahedron), or twenty measurements (dodecahedron). For simplicity,

our original selection consisted of four states, starting with right-hand circular polarization, with Poincaré coordinates ($2\theta_{PF}$, ϕ_{Δ}, I_P) of (0°, 90°, 1), and three additional semi-elliptical states at (0°, -19.4712°, 1), (120°, -19.4712°, 1), and (-120°, -19.4712°, 1). However, since the high angular dependence of retarders is one of the largest potential sources of polarimetric error, it is best to minimize the total retardance required to generate or analyze the four states. This results in a rotation to two purely linear states – (125.2644°, 0°, 1) and (-125.2644°, 0°, 1) – and two elliptical states with reversed rotation directions – (0°, 54.7356°, 1) and (0°, -54.7356°, 1).

One common metric used to describe polarimetric resolution is the condition number, κ, of the analysis matrix, $\mathbf{B}$. The condition number represents the maximum error propagation from the measurements to the calculated polarization elements, either the Stokes vector elements for passive polarimetry or the Mueller matrix elements for active polarimetry. The analysis matrix is derived from the Mueller matrices describing the PSA states or PSG states as

$$\mathbf{B} = \begin{bmatrix} \mathbf{M_0^1} \\ \mathbf{M_0^2} \\ \mathbf{M_0^3} \\ \mathbf{M_0^4} \end{bmatrix} = \begin{bmatrix} m_{00}^1 & m_{01}^1 & m_{02}^1 & m_{03}^1 \\ m_{00}^2 & m_{01}^2 & m_{02}^2 & m_{03}^2 \\ m_{00}^3 & m_{01}^3 & m_{02}^3 & m_{03}^3 \\ m_{00}^4 & m_{01}^4 & m_{02}^4 & m_{03}^4 \end{bmatrix}, \tag{40}$$

where M_0^i is the first row of the matrix for the ith state. The condition number is then calculated as

$$\kappa(\mathbf{B}) = ||\mathbf{B}||_2 \, ||\mathbf{B}^{-1}||_2 = \frac{\sigma_{max}(\mathbf{B})}{\sigma_{min}(\mathbf{B})}, \tag{41}$$

where $||\cdot||_2$ is the L^2 norm, σ_{max} and σ_{min} are the maximum and minimum singular values decomposition. In the case that $\mathbf{B}$ is singular (or near-singular), it may be necessary to use calculate κ using the pseudo-inverse rather than the inverse. Even for optimal configurations, κ still has a minimum value greater than 1; the minimum for linear polarimetry is $\sqrt{2}$, while

the minimum for full polarimetry (including elliptical states) is $\sqrt{3}$.

Although PSG and PSA states are chosen precisely, the reality of polarization filters, retarders, and their mounts introduce potential error. Each polarization element has associated tolerances for its effects on incident light. We can apply these tolerance values as maximum deviations from the expected PSG and PSA Mueller matrices, producing a new κ for the $\mathbf{B}$ matrix for each combination of positive or negative deviations; the worst-case scenario value for κ is then our accepted system value.

For an LP, we should consider the extinction ratio, r_e, and the tolerance on the major axis orientation angle, $\Delta\theta_p$. For a QWP or HWP, we should consider the retardance tolerance, $\Delta\phi_\Delta$, and the tolerance on the crystal axis orientation angle, $\Delta\theta_f$. For the LPs used, r_e is about 1100 at 532-nm and 3800 at 1064-nm. For the HWP, $\Delta\phi_\Delta$ is about of $\lambda/200$ for both wavelengths, and for the QWPs it is a maximum of $\lambda/100$ for both wavelengths. The clean-up polarizer is at a fixed angle that defines the polarization coordinate system of the device (and therefore does not contribute to polarimetric error other than a global orientation offset), while the remaining components are mounted in rotation stages with a maximum intra-measurement-set $\Delta\theta$ equal to $\pm 0.1^\circ$.

Applying these tolerance values while generating $\mathbf{B}$, the worst-case scenario condition numbers were $\kappa_{532,G} = 1.7792$, $\kappa_{532,A} = 1.7932$, $\kappa_{1064,G} = 1.7769$, and $\kappa_{1064,A} = 1.7908$. On average, this represents a combined maximum propagating magnification of noise of 3.19 for the 532-nm channel and 3.18 for the 1064-nm channel, which are both about 1.06-times higher than the best case scenario of 3-times magnification, respectively.

The dominant source of error in the transmitter arm is the pulse energy tolerance and the dominant source of error in the receiver when using with the majority of the APD dynamic range is the integrated noise. The pulse energy is specified as stable to within 0.61% when operating at 95% power (as we do in our measurements); scaling by $\kappa_{532,G}$ and $\kappa_{1064,G}$, respectively, this contributes $\pm 1.09\%$ and $\pm 1.08\%$ error to the Mueller coefficients via the

generator arm for the respective channels.

The potential coefficient error from the receiver is more dependent on the amount of dynamic range used, and therefore the maximum measurement value. However, we can make a very conservative constraint that we will be operating with a maximum signal not less than one-tenth the dynamic range (170 mV). The APDs have specified RMS noise of 0.46 mV for the 532-nm channel and 1.02 mV for the 1064-nm channel. Scaling by the condition numbers $\kappa_{532,A}$ and $\kappa_{1064,A}$ for error propagation, we can therefore expect not more than $\pm 0.48\%$ (532-nm) or $\pm 1.07\%$ (1064-nm) error to the Mueller coefficients via the analysis arm.

Combined, we expect not more than $\pm 1.57\%$ (532-nm channel) or $\pm 2.17\%$ (1064-nm channel) in our Mueller coefficient calculations. For a Mueller matrix reported as normalized to its m_{00} value, this results in a maximum Mueller coefficient error of ± 0.016 and ± 0.022 for the respective channels.

5.5.3 Automation and Measurement Rate

While the DMPL testbed will be used generally on contrived scenes that are likely to remain static or homogeneous for extended times, some environmental effects of interest may change on a time scale of minutes. Therefore, we had a goal of acquiring a full set of 16 measurements within a few minutes. Using the less optimal states for the non-ranging polarimeter we built previously [32], an experienced operator could run the system in 1 to 3 minutes. However, to improve safety with the higher-power pulsed laser and to narrow our PSG and PSA state tolerances due to repeatable precision for θ_p and θ_f, we implemented motorized rotation stages. The stages reduced the discrete angle tolerance to $0.3°$, as compared to approximately $1°$ for manual rotation; referring to calculations made in the previous section, the larger tolerance would have resulted in noise propagation of about 1.19-times and 1.18-times higher than the ideal for the 532-nm and 1064-nm channels,

respectively. These rotation stages are limited in their rotation speed and how many stages can be operated at one time by the software controls.

Even collecting multiple pulses, the rotation speed of the motorized stages is the limiting factor for measurement rate. Therefore, the order of PSG-PSA state combinations was optimized for minimum total rotation time by determining the total rotation time for each permutation of states and selecting one of the few options with the lowest result. The full set of measurements currently takes just under 3 minutes regardless of operator experience and with higher polarimetric accuracy than the non-ranging polarimeter.

5.5.4 Variable Scene Distances

The DMPL system is meant to function both in a laboratory environment and outdoors, with scene distances from a few meters up to a few hundred meters. The geometric overlap function of the illumination area and the receiver field-of-view (FOV) depends strongly on range for all bistatic systems. At long distances, usually more than 100 m, the best overlap is achieved when the optical axes of the Tx and Rx are parallel; however, at shorter distances, the overlap is often zero unless the optical axes are made to cross. When the optical axes cross, maximum overlap occurs in a window around the fixed range where they intersect, falling off at ranges nearer or farther from the lidar. Determining this "weighted" depth of field (the region of full overlap and the edges where partial overlap occurs) requires us to know both the system's Tx divergence and Rx FOV, which are 5 mrad and 15 mrad, respectively.

To achieve effective ranging at highly variable scene distances, the receiver was mounted on a rigid optical breadboard and mounted on a locking rotation stage, as shown in Fig. 26. This allows manual alignment via return maximization from a reference target at a desired scene distance prior to measurements. Retractable legs allow the receiver platform to be leveled and better stabilized once its pointing angle is set. The angle between the Tx and

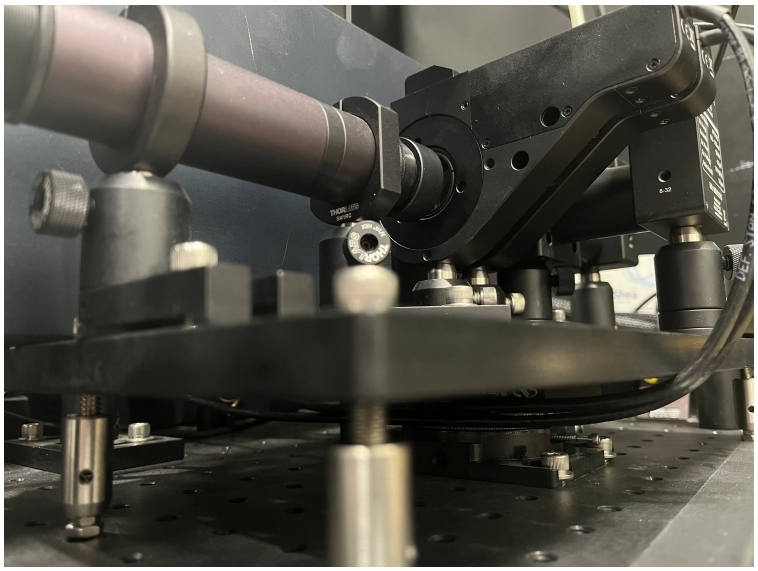


Figure 26: A look underneath the receiver, showing the locked rotation stage and the retractable legs used to level and better stabilize the platform.

Rx optical axes is referred to herein as ψ. For an optimized scene range of about 2 meters, our set up in the optics lab, we find ψ to be about 3.7° and a depth of field of about 0.35 m FWHM. For an optimized scene range of about 11.5 meters in our lab's laser tunnel, which is the longest path we comfortably achieve in our lab, we find $\psi \approx 0.65°$ and a depth of field of about 10 m FWHM.

5.6 Calibration & Validation

As an intended reference testbed, we calibrated and validated the DMPL system's responses. The calibration focused on scene reflectance, and we validated the polarimetric measurements against samples with known Mueller responses. In addition, the tolerance on the system's coordinate plane was determined using a polarimetric validation sample.

5.6.1 Reflectance Calibration

The relative calibration function for our system takes the form of $K(\omega_i, \omega_v)$, with units $(sr \cdot V \cdot m^2)^{-1}$, in the equation relating bidirectional reflectance distribution function (BRDF),

f_r, and the range-normalized APD electrical response, $V^R(\omega_v)$:

$$f_r(\omega_i, \omega_v) = V^R(\omega_v) \left[\frac{C(\omega_i, \omega_v)}{T_{sys} \Delta E_0 \cos(\theta_i)} \right] = V^R(\omega_v) K(\omega_i, \omega_v) = R^2 V(\omega_v) K(\omega_i, \omega_v), \quad (42)$$

therefore,

$$K(\omega_i, \omega_v) = \frac{f_r(\omega_i, \omega_v)}{V^R(\omega_v)} = \frac{C_2}{\cos(\theta_i)}, \quad (43)$$

where C is the calibration function capturing responsivity and the like, T_{sys} is the transmittance of the receiver system, ΔE_0 is the transmitter irradiance at normal incidence on the sample, C_2 is a constant capturing those three values for operation in set conditions, and ω_i and ω_v are angle vectors (θ, ϕ) for the incidence and viewing directions, respectively. To keep the detector operating within its linear response region across a wide range of sample reflectances, we must also apply different neutral spectral density (ND) filters; for a more reflective sample, we add more ND filters and reduce the total optical power falling on the detectors. Adding ND filters to the system reduces the value of T_{sys} as a multiplier, so generating calibration functions with a T_{sys} modifier, T_{ND}, should cover use cases with varied sample reflectivities.

We measured isotropic, highly Lambertian reference panels with known constant BRDF, $f_r^L(\rho_{ref})$, at a range of T_{ND} to generate both the K_{532} and K_{1064} relative calibration functions. For these types of reference panel, the isotropic nature reduces the BRDF dependencies to $f_r(\theta_i, \theta_v)$, and similarly the dependencies of the K functions are reduced. For our system, the viewing angle, θ_v, is defined by a fixed separation angle, ψ, from the incidence or illumination angle, θ_i. Therefore, the final form of the relative calibration function for the DMPL system is

$$K_\lambda(\theta_i, \psi; T_{ND}) = \frac{C_\psi}{T_{ND} \cos(\theta_i)}, \quad (44)$$

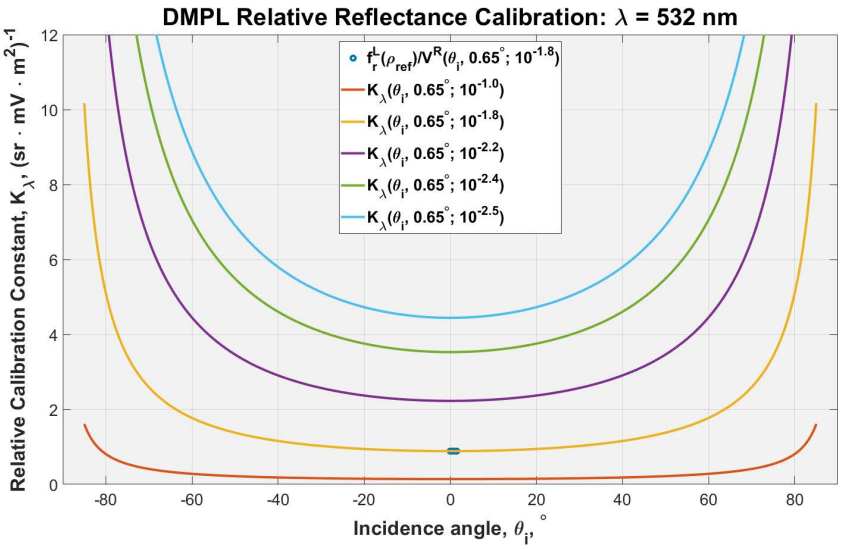


Figure 27: Plot of K_{532} as a function of θ_i, for a handful of T_{ND} values, as well as the fitted inverse cosine curves extending to values beyond 0 to ψ. These values are for our laser tunnel setup where $\psi \approx 0.65°$.

where we can determine C_ψ as

$$C_\psi = \frac{f_r^L(\rho_{ref}) T_{ND} \cos(\theta_i)}{V^R(\theta_i, \psi)}. \tag{45}$$

This form of the equation is useful for extrapolating K_λ values for eccentric cases from those found under near-ideal conditions.

Although the Spectralon® used for these measurements is highly diffuse, no real material can be truly Lambertian across all angles and this material is known to be most Lambertian at incidence or viewing angles near surface normal [2, 26]. Therefore, we performed measurements at normal incidence angle, $\theta_i = 0$, and as close as possible to normal viewing angle, $\theta_i = \psi$, and halfway between the two (the specular case), $\theta_i = \psi/2$. For long distances, and therefore small ψ, we were generally limited to steps of about 0.5°.

Selected data and extrapolated values are shown in Fig. 27, limited to the 532-nm case with only five values of T_{ND} following the format in Eq. 44. For the DMPL system, the value of $C_{0.65}$ is 0.01405 $(sr \cdot mV \cdot m^2)^{-1}$ for the 532-nm channel and 0.2814 $(sr \cdot mV \cdot m^2)^{-1}$

for the 1064-nm channel. Note that $T_{ND} = 10^{-OD}$, where OD is the total optical density of the applied ND filters, but the actual OD for a ND filter at a specific wavelength is often different than its nominal OD. For example, the ND filters we have in our lab typically have an order of magnitude difference in their OD at 532-nm and 1064-nm. Therefore, care must be taken to apply the appropriate OD values for each wavelength's relative calibration separately and the most accurate method remains taking calibration measurements with the full intended setup when possible.

5.6.2 Ranging Validation

For the equipment used, we have a range resolution of about 15 cm. Each of the Mueller matrix coefficients above was derived from 16 measurements returned from a single lidar range bin with the sample at a given θ_i. We can also produce figures showing Mueller coefficients as a function of range. This is useful for differentiating multiple staggered or non-opaque samples at different ranges. An example of the Mueller coefficient plots as a function of range is shown in Fig. 28, where we have placed two samples at different range bins such that they are only partially illuminated by the transmitter.

The two cardboard samples were placed in our laser tunnel at approximately 8.69 m and 13.12 m. The lidar returns show peaks in the range bins containing these two values, the first bin from 8.61 to 8.75 m and the second bin from 13.10 to 13.25 m, validating our measured and applied electronic delay. Note that the return is spread over a range of approximately 1 m at FWHM, which is appropriate signal distribution for our approximately 7-ns pulse length. In this and other plots, values for which the signal across the 16 measurements does not rise above the noise threshold are masked out; this prevents the plots from appearing extremely noisy when normalized to the m_{00} coefficient. This plot shows only a signal strength using arbitrary units since the amount of the illumination area falling on each sample in the complex scene cannot be precisely determined. But for scenes where the illumination area

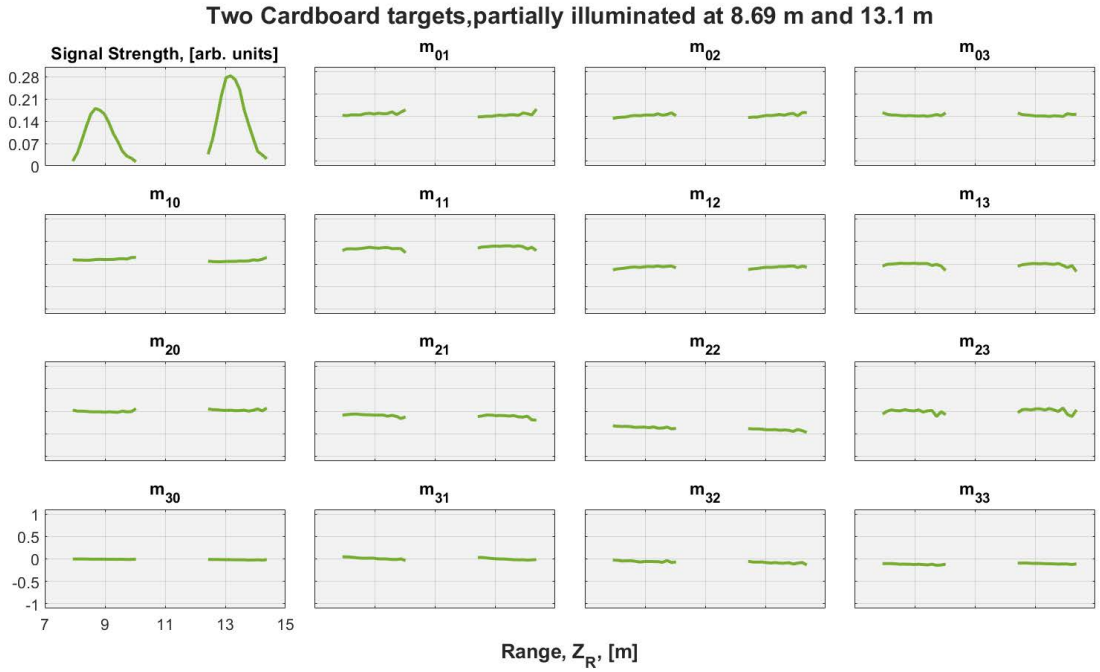


Figure 28: Plot of Mueller coefficients in the 532-nm channel as a function of range for two cardboard samples at a range of 8.69 m and 13.1 m. Note that the Mueller coefficients are normalized to m_{00}, and in place of m_{00} an arbitrary signal strength is plotted instead. Range values for which the signal is at or below the noise threshold are masked out of the plots. All plots share the same x-axis scale and limits, and only the upper-left plot has different y-axis scale and limits.

falls entirely on a single sample and that sample's area is under-filled by the illumination, we can use the reflectance relative calibration discussed in 5.6.1 to instead report BRDF with units of sr^{-1}.

5.6.3 Polarimetric Validation

To validate the DMPL as a polarimeter, we measured a diffuse reflector, a scene containing three distinct materials in different range bins, and a specular sample with multiple linear polarizer orientations and a quarter-waveplate (QWP) in front of the receiver.

The diffuse sample is expected to be as near a perfect depolarizer as is achievable, represented by all coefficients other than m_{00} having values of 0 (when normalized to m_{00}). The measurements were taken with OD 1.80 filters in place. The resulting Mueller matrix for the diffuse material for θ_i ranging from -60° to 60° is shown in Fig. 29. Within the expected error of about ± 0.02 for the m_{00}-normalized coefficients, this plot shows the expected polarimetric response from Spectralon® references measured in previous literature [1, 2, 26, 51], and, though a bit harder to quantify by looking at the plot, the cross-range slices of the BRF plot are flat as expected (given their cosinusoidal correction relative to θ_i based on the K_λ calculation in Eq. 44).

For a more complex scene, we placed a plant at 8.23 m, a piece of cardboard at 9.75 m, and a piece of aluminum at 11.89 m. The plant was placed so it cast a shadow onto the cardboard, and only a very small sliver of the beam passed the cardboard to the aluminum (otherwise the return from the metal would be much too bright compared to the other returns). These three materials were chosen to show distinct polarimetric and spectral signatures. The plant and cardboard are relatively diffuse, with the plant being a bit glossier in the visible wavelengths, while the aluminum provides a near-specular response which is partially tempered in the visible by the striations left in its surface from milling. Live plants are commonly known to have higher reflectance in the infrared than the visible, which can

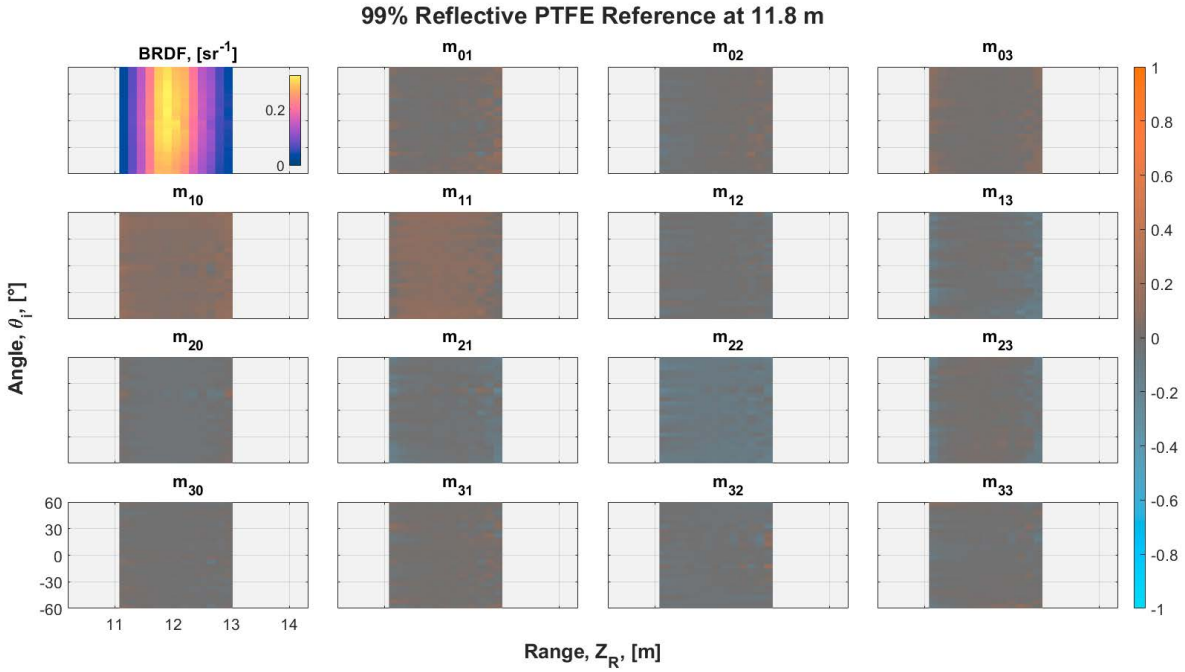


Figure 29: Plot of Mueller coefficients for a 99% reflective Spectralon® sample from -60° to 60° in steps of 5°. Note that the very small values of the coefficients are 0 to within the system error. No data are shown for range-angle combinations where there was no detectable return signal above the noise. Each plot shares the same x- and y-axis scale and limits.

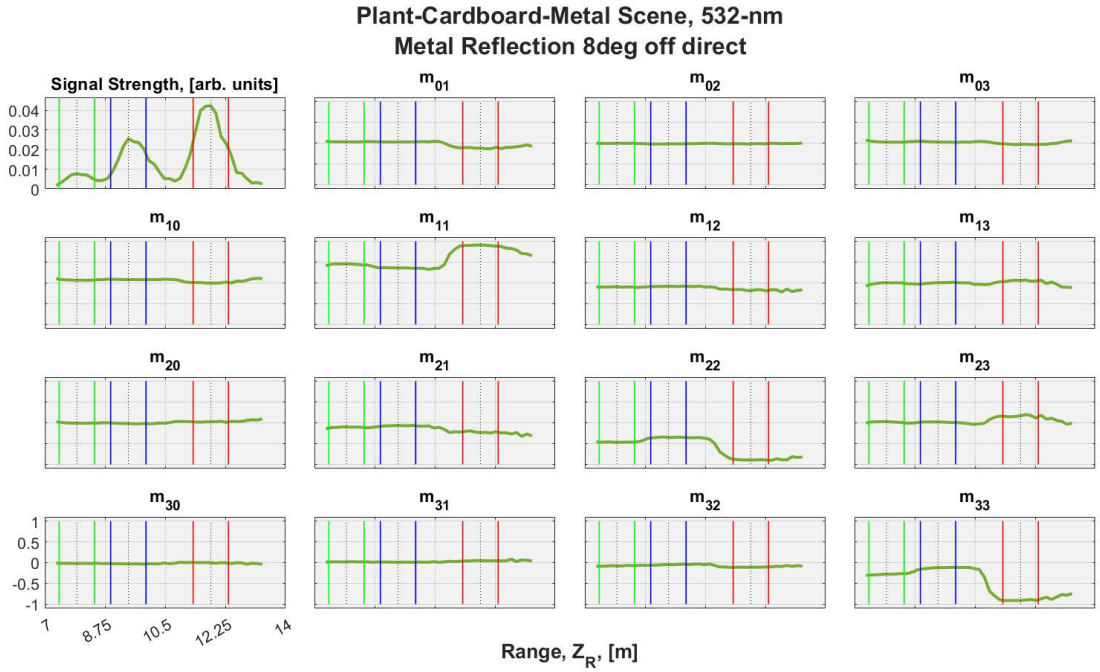


Figure 30: Plot of Mueller coefficients in the 532-nm channel as a function of range for three partially illuminated samples: a plant at 8.23 m, cardboard at 9.75 m, and aluminum at 11.89 m. The peak signal for each sample is shown with a vertical dotted line, and the unambiguous range resolution around those peaks are denoted with colored vertical lines: green (plant), blue (cardboard), and red (aluminum). Note that the Mueller coefficients are normalized to m_{00}, and in place of m_{00} an arbitrary signal strength is plotted. All plots share the same x-axis scale and limits, and only the upper-left plot has different y-axis scale and limits.

compare to the relatively flat spectral response of diffuse cardboard. Similarly, the milling striations in the aluminum should have less effect at larger wavelengths, so we expect to see a sharper peak signal in the lidar return due to reduced multiple scattering. The processed data for the 532-nm and 1064-nm channels are shown in Figs. 30 and 31, respectively, and do show all of the expected trends. The plotted data also show appropriate separation between signals based on the pulse width.

The specular sample was measured independently to generate a scene Mueller matrix,

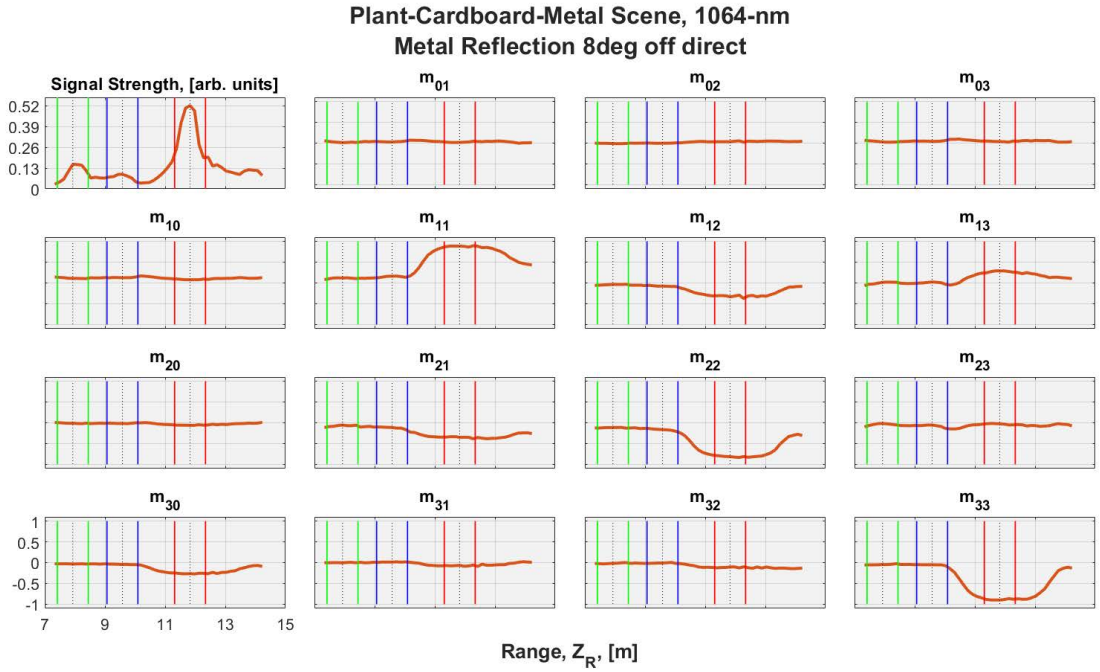


Figure 31: Plot of Mueller coefficients in the 1064-nm channel as a function of range for three partially illuminated samples: a plant at 8.23 m, cardboard at 9.75 m, and aluminum at 11.89 m. The peak signal for each sample is shown with a vertical dotted line, and the unambiguous range resolution around those peaks are denoted with colored vertical lines: green (plant), blue (cardboard), and red (aluminum). Note that the Mueller coefficients are normalized to m_{00}, and in place of m_{00} an arbitrary signal strength is plotted. All plots share the same x-axis scale and limits, and only the upper-left plot has different y-axis scale and limits.

$\mathbf{M_{sc}}$, represented as a combination of

$$\mathbf{M_{sc}}(\omega_i, \omega_r) = \mathbf{M_P}(\omega_r)\mathbf{M_{spec}}(\omega_i, \omega_r), \tag{46}$$

where $\mathbf{M_{spec}}$ is the polarized response of the specular sample alone and $\mathbf{M_P}$ is the expected response of the transmissive polarizing element placed in front of the receiver. For small separation angles, ψ, the values of ω_i and ω_r are functionally equal and, constraining sample rotation to the horizontal plane and a fixed position of the polarizer, Eq. 46 reduces to

$$\mathbf{M_{sc}}(\theta_i) = \mathbf{M_P}\mathbf{M_{spec}}(\theta_i). \tag{47}$$

For the specular measurements, we used a piece of aluminum as the sample, which required OD 3.80 to prevent saturation. At the specular angle, this sample has a Mueller matrix close to an identity matrix but with the m_{22} and m_{33} coefficients having a negative sign (indicating π phase offset). The surface is not as smooth as a high quality mirror, but still serves as a largely non-depolarizing sample. At the sample range of 11.7 m, the aluminum's polarized response at 532-nm was measured as

$$\mathbf{M_{spec}^{532}} = \begin{bmatrix} 1.00 & 0.09 & 0.01 & 0.03 \\ 0.09 & 0.95 & 0.28 & -0.03 \\ 0.04 & 0.25 & -0.94 & 0.13 \\ -0.02 & 0.03 & -0.15 & -0.93 \end{bmatrix}. \tag{48}$$

A notable feature of the aluminum sample was a diffraction effect orthogonal to milling striations on the metal surface. For the data presented in Eq. 48, these striations were horizontal, causing diffraction in the vertical direction. This grating-like structure may account for the significant above-zero values of the m_{01}, m_{10}, m_{12}, m_{21}, m_{23}, and m_{32}, as it

increases non-normal reflectance polarizance/diattenuation as well as induces variable phase retardance. Although $\mathbf{M}_{\mathbf{spec}}^{\mathbf{532}}$ is sufficient for the polarization element analysis we wanted to perform, for an interested reader we also include the specular sample's Mueller matrix when the diffracting striations are rotated 90° (resulting in horizontal diffraction).

$$\mathbf{M}_{\mathbf{spec,Horz}}^{\mathbf{532}} = \begin{bmatrix} 1.00 & -0.02 & -0.01 & 0.03 \\ -0.00 & 0.95 & -0.16 & 0.02 \\ 0.05 & -0.20 & -0.97 & 0.11 \\ -0.01 & 0.03 & -0.13 & -0.91 \end{bmatrix} \tag{49}$$

With the specular sample's response determined, we added a linear polarizer in front of the receiver such that the entire scene was seen through $\mathbf{M_P}$. The polarizer was oriented horizontally (case H, 0°), vertically (case V, 90°), diagonally (case D, 45°), and at a non-cardinal angle (case N, 30°), all to within ±0.5°. We can remove the known $\mathbf{M_{spec}}$ from each of the resulting $\mathbf{M_{sc}}$ for the scenes to produce the measured Mueller matrices for the polarizers. For the sake of space, only the 532-nm channel's horizontal orientation matrix, $\mathbf{M}_{\mathbf{P,H}}^{\mathbf{532}}$, and non-cardinal matrix at 30°, $\mathbf{M}_{\mathbf{P,N}}^{\mathbf{532}}$, are shown here.

$$\mathbf{M}_{\mathbf{P,H}}^{\mathbf{532}} = \begin{bmatrix} 1.00 & 1.01 & 0.05 & 0.07 \\ 1.01 & 1.00 & 0.04 & 0.04 \\ -0.01 & 0.02 & 0.04 & 0.01 \\ 0.01 & -0.03 & 0.01 & 0.04 \end{bmatrix} \tag{50}$$

$$\mathbf{M}_{\mathbf{P,N}}^{\mathbf{532}} = \begin{bmatrix} 1.00 & 0.44 & 0.89 & -0.02 \\ 0.54 & 0.23 & 0.47 & -0.02 \\ 0.83 & 0.37 & 0.76 & -0.00 \\ -0.05 & -0.04 & -0.01 & 0.03 \end{bmatrix} \tag{51}$$

These Mueller matrices are normalized to their m_{00} coefficients for ease of analysis and error discussion. For the $\mathbf{M}_{\mathbf{P,H}}^{\mathbf{532}}$ case, the ideal linear polarizer coefficients are zero except for the upper-left quadrant, where the normalized coefficients should all be 1; this is approximately the case as reported in Eq. 50 to within about 0.05 (with one marginal outlier of 0.07). Given the polarizer pass-axis orientation uncertainty of 0.5°, we might expect any of the upper-left nine coefficients other than m_{00} (m_{01}, m_{02}, m_{10}, m_{11}, m_{12}, m_{20}, m_{21}, m_{22}) to be off by up to 0.87% in magnitude but all about equal to each other and of matching sign for the horizontal case . Additionally, by dividing one measurement out of another, the error propagates through the calculations again, increasing the maximum possible error from ±1.57% for the 532-nm channel by a factor of 3.19 ($\kappa_{532,G} * \kappa_{532,A}$) for a new maximum expected error of ±5.02% when estimating the $\mathbf{M}_{\mathbf{P}}^{\mathbf{532}}$ coefficients. With these caveats in mind, the results presented in Eqs. 50 and 51 are within the expected error tolerances with the exceptions of $m_{03}^{P,H}$ and $m_{21}^{P,N}$, which display error about 2% higher than expected.

To get a better sense of error in the fourth row and fourth column terms, we also measured a QWP (532-nm design wavelength) at a non-cardinal angle of -6° (case E, for elliptical). The waveplate was inserted in place of the previous linear polarizer.

$$\mathbf{M}_{\mathbf{P,E}}^{\mathbf{532}} = \begin{bmatrix} 1.00 & -0.01 & 0.00 & 0.02 \\ 0.00 & 0.99 & -0.18 & 0.27 \\ 0.03 & -0.21 & -0.01 & 0.95 \\ -0.02 & -0.23 & -1.04 & -0.01 \end{bmatrix} \tag{52}$$

The ideal QWP at -6° should have a Mueller matrix of

$$\mathbf{M}^{\mathbf{532}}_{\mathbf{P,E-ideal}} = \begin{bmatrix} 1.00 & 0.00 & 0.00 & 0.00 \\ 0.00 & 0.96 & -0.20 & 0.21 \\ 0.00 & -0.20 & 0.04 & 0.98 \\ 0.00 & -0.21 & -0.98 & 0.00 \end{bmatrix}. \tag{53}$$

The extended maximum theoretical error of ±5.02% from above should still apply, and we see only three terms here above that value, with a maximum observed error of 6.53%. Given the 0.5° orientation uncertainty, we might expect up to an additional 1.7% error on the bottom-right coefficients (other than m_{33}), which accounts for the largest error seen here. Across all measurements, 20% have greater than 5.02% error, but only 7% have error beyond what might be expected given our orientation uncertainties, the highest being 13.62% error. These high error values were consistent for a given coefficient in a given scenario across multiple measurement sets. Because it is possible for an unknown Mueller matrix to have multiple possible solutions when poorly constrained, there is a distinct possibility these higher-than-expected errors arise from the use of milled aluminum as our reflector, which is a rather low-quality mirror.

For the five measurement scenarios, the mean magnitude of the measurement error as compared to the ideal expected polarization element responses are 3.05% (case H), 2.63% (case V), 2.68% (case D), 3.04% (case N), and 2.38% (case E). If we take into account the compounded influence of κ when dividing out $\mathbf{M_{spec}}$ from $\mathbf{M_{sc}}$, the scene measurement error magnitudes have a maximum observed error of 4.27%, and the mean errors reduce further to 0.96% (case H), 0.82% (case V), 0.84% (case D), 0.95% (case N), and 0.75% (case E). Additional validation with higher-quality, large-area mirrors can be performed in future work using the same procedure before the device is deployed for a given application to potentially cull the handful of observed errors which were above the theoretical expectations.

5.6.4 Global Rotation Tolerance

The effect of combined offsets of the polarization elements in the PSG and PSA are discussed in Sect. 5.5.2, but for the many cases where the sample is not mounted to the same level surface as the DMPL, it is important to note the potential coordinate system error. The coordinate system of the DMPL associates horizontal and vertical polarization with the surface on which it is mounted. This was accomplished using a reference polarizer leveled to the smooth optical table's polarized reflection, resulting in an orientation known to within $\pm 0.5^\circ$. We used this reference polarizer to determine the orientation of the polarization axis or crystal axes of each of the PSG and PSA polarization elements, with their rotation stage tolerance of $\pm 0.1^\circ$. The actual combined tolerance for each type of polarization element is difficult to calculate, but as combined error is always a geometric sum, it cannot be greater than the simple sum of the errors. Therefore, when measuring a sample at range, DMPL reports cross-range orientation angles relative to the surface it is mounted on with tolerance not greater than $\pm 0.6^\circ$.

5.7 Discussion & Conclusions

We have described the design, build, and specifications of a dichroic Mueller pulsed lidar testbed. This testbed device was built with the primary purpose of providing proof-of-concept measurements for more complex polarimetric ranging devices, emphasizing high polarimetric accuracy and precision and adaptability to varied control scene scenarios. The theory and design decisions presented here can be used to build a similar system for these purposes at alternate operating wavelengths or SWaP requirements.

The system was calibrated relative to a Lambertian reflectance standard so its data could be presented in BRF values. We also validated the system operation relative to the calculated maximum Mueller coefficient tolerances, $\pm 1.46\%$ for the 532-nm channel and

$\pm 2.04\%$ for the 1064-nm channel, relative to the expected m_{00} coefficient. The DMPL ranging capability was also validated to within its range-bin limit. Inherent coordinate system tolerances were also reported.

This system is currently planned for use in multi-static polarimetry proofs of concept, material discrimination measurements, and early measurements of snow and smoke's volumetric effects on polarized scattering for ranging applications. The entire system fits on a relatively small computer cart to move easily between indoor and outdoor measurement scenes, and can be transported to alternate sites by operators with limited training.

CHAPTER SIX

CONCLUSION

6.1 Summary of Research Objectives & Achievements

This dissertation has presented the design, construction, calibration, and validation of the DMPL testbed device intended to provide science-grade measurements of various samples' polarimetric responses. The four primary objectives of this work were 1) to design and build optimal polarization state generator (PSG) and analyzer (PSA) systems; 2) provide methods to fill knowledge gaps in material P-BRDF responses at or near monostatic geometries; 3) to design and build a fully-polarimetric lidar testbed operating in the visible and near-infrared; and, 4) to calibrate and validate the polarimetric lidar testbed against known samples and preliminary samples of interest, providing an operating procedure for future use.

Objective 1 was accomplished through literature review, analysis of polarization element specifications, and the design and optimization processes discussed primarily in Ch. 2 as well as in Sect. 5.5.2 of Ch. 5. Objective 2 was accomplished through the publication presented in Ch. 2, with example optimizing and characterizing measurements additionally presented in Ch. 4. The completion of objective 3 is discussed in detail in Ch. 5, which describes the final DMPL system. Objective 4 involved both the relative reflectance calibration discussed in Ch. 3 and the additional calibrations and validation measurements discussed in Ch. 5. The final DMPL system is a result of these constituent efforts, having produced a high polarimetric accuracy testbed with which to test the theories of or validate future polarized lidar research.

6.2 Contributions to the Field

This research makes significant contributions to the field of photonics engineering in several key areas. First, the development and publication of a simple monostatic polarimeter fills a critical gap in the literature, providing a tool that researchers can use for both validating reference measurements of novel samples. Prior to this work, most P-BRDF systems were limited by viewing geometry constraints to exclude the monostatic and near-monostatic cases – the geometries most common in lidar instruments.

Second, by producing a fully-polarimetric lidar, this research furthers the study of volumetric scattering effects on opaque sample detection and classification. Measurements made with this testbed can provide additional information on the effects of environmental factors such as fog, smoke, and precipitation on the relative degradation of polarimetric features of lidar returns from samples in real-world scenarios. This is of particular importance for remote sensing applications where these environmental factors are often encountered.

Lastly, this dissertation has provided valuable insight into the relative reflectance calibration process as well as polarimetric calibration, error tolerance analysis, and validation for polarimetric lidar. The methods and protocols developed for this purpose can be adapted to other polarimetric systems, contributing to a more standardized approach in the field.

6.3 Implications & Applications

The successful development and validation of the polarimetric testbed opens the door to a wide range of applications. In remote sensing, the ability to measure the polarimetric response of both opaque samples and volumetric environmental effects with a high degree of accuracy is crucial for interpreting data from the growing field of non-atmospheric, polarimetric lidar and ladar systems, especially in the presence of non-ideal atmospheric disturbances. This testbed is sufficiently mobile to be used in the field to evaluate, at least

under relatively uncontrolled scenarios, the effects of fog, smoke, or precipitation conditions on machine vision scenarios. Such data would advance algorithms for remote sensing data processing in more robust sets of scenarios.

Furthermore, the science-grade measurements of the DMPL allows it to measure material polarimetric properties with high accuracy and precision. Depending on the materials measured, these data can advance machine vision applications in situational awareness or other sample discrimination applications where spectral or radiative information is insufficient. Particularly when combined with machine learning techniques, the novel data from the DMPL testbed may provide significantly enhanced object discrimination in polarimetrically sensed scenes.

Finally, with improving division-of-focal-plane (DoFP) polarization cameras on the market, multi-static polarimetric sensing of complex scenes becomes a possibility. The characterizing data from the DMPL discussed above is useful in this regard, and the DMPL itself can serve as the illumination source and the ranging component of such a multi-static system.

REFERENCES CITED

[1] Nathaniel J Field, Michael R Roddewig, and Joseph A Shaw. Near-monostatic angular mueller matrix measurements using a simple laser polarimeter. In *Polarization Science and Remote Sensing X*, volume 11833, pages 175–185. SPIE, 2021.

[2] Nathaniel J Field, Jarrod P Brown, Darrel B Card, Chad M Welsh, Andre J Van Rynbach, and Joseph A Shaw. Gray spectralon polarized reflectance deviations from lambertian. In *Polarization: Measurement, Analysis, and Remote Sensing XV*, volume 12112, pages 49–58. SPIE, 2022.

[3] J. Scott Tyo, Dennis L. Goldstein, David B. Chenault, and Joseph A. Shaw. Review of passive imaging polarimetry for remote sensing applications. *Appl. Opt.*, 45(22): 5453–5469, Aug 2006. doi: 10.1364/AO.45.005453.

[4] Christian K. Keyser, Richard K. Martin, Helena Lopez-Aviles, Khanh Nguyen, Arielle M. Adams, and Demetrios Christodoulides. Single-pulse, kerr-effect mueller matrix lidar polarimeter. *Opt. Express*, 28(9):13694–13713, Apr 2020. doi: 10.1364/OE.388565.

[5] François Goudail, Patrick Terrier, Yoshitate Takakura, Laurent Bigué, Frédéric Galland, and Vincent DeVlaminck. Target detection with a liquid-crystal-based passive stokes polarimeter. *Appl. Opt.*, 43(2):274–282, Jan 2004. doi: 10.1364/AO.43.000274.

[6] Daniel A. Lavigne, Mélanie Breton, Georges Fournier, Jean-François Charette, Mario Pichette, Vincent Rivet, and Anne-Pier Bernier. Target discrimination of man-made objects using passive polarimetric signatures acquired in the visible and infrared spectral bands. In Joseph A. Shaw and J. Scott Tyo, editors, *Polarization Science and Remote Sensing V*, volume 8160, page 816007. International Society for Optics and Photonics, SPIE, 2011. doi: 10.1117/12.894055.

[7] Shih-Schon Lin, K.M. Yemelyanov, E.N. Pugh, and N. Engheta. Polarization enhanced visual surveillance techniques. In *IEEE International Conference on Networking, Sensing and Control, 2004*, volume 1, pages 216–221 Vol.1, 2004. doi: 10.1109/ICNSC.2004.1297437.

[8] K. Knobelspiesse, B. van Diedenhoven, A. Marshak, S. Dunagan, B. Holben, and I. Slutsker. Cloud thermodynamic phase detection with polarimetrically sensitive passive sky radiometers. *Atmospheric Measurement Techniques*, 8(3):1537–1554, 2015. doi: 10.5194/amt-8-1537-2015.

[9] Kenneth Sassen. Polarization in lidar: a review. In Joseph A. Shaw and J. Scott Tyo, editors, *Polarization Science and Remote Sensing*, volume 5158, pages 151 – 160. International Society for Optics and Photonics, SPIE, 2003. doi: 10.1117/12.507006. URL `https://doi.org/10.1117/12.507006`.

[10] Laura M. Eshelman and Joseph A. Shaw. The vis–swir spectrum of skylight polarization. *Appl. Opt.*, 57(27):7974–7986, Sep 2018. doi: 10.1364/AO.57.007974.

[11] Joseph A. Shaw, Nathan L. Seldomridge, Dustin L. Dunkle, Paul W. Nugent, Lee H. Spangler, Jerry J. Bromenshenk, Colin B. Henderson, James H. Churnside, and James J. Wilson. Polarization lidar measurements of honey bees in flight for locating land mines. *Opt. Express*, 13(15):5853–5863, Jul 2005. doi: 10.1364/OPEX.13.005853.

[12] Songxin Tan, Jason Stoker, and Susan Greenlee. Detection of foliage-obscured vehicle using a multiwavelength polarimetric lidar. In *2007 IEEE International Geoscience and Remote Sensing Symposium*, pages 2503–2506, 2007. doi: 10.1109/IGARSS.2007.4423352.

[13] Joseph A. Shaw and Nathan J. Pust. Icy wave-cloud lunar corona and cirrus iridescence. *Appl. Opt.*, 50(28):F6–F11, Oct 2011. doi: 10.1364/AO.50.0000F6.

[14] Michael R. Roddewig, Nathan J. Pust, James H. Churnside, and Joseph A. Shaw. Dual-polarization airborne lidar for freshwater fisheries management and research. *Optical Engineering*, 56(3):031221, 2017. doi: 10.1117/1.OE.56.3.031221.

[15] Michael R. Roddewig, James H. Churnside, F. Richard Hauer, Jacob Williams, Patricia E. Bigelow, Todd M. Koel, and Joseph A. Shaw. Airborne lidar detection and mapping of invasive lake trout in yellowstone lake. *Appl. Opt.*, 57(15):4111–4116, May 2018. doi: 10.1364/AO.57.004111.

[16] S. R. Pal and A. I. Carswell. Polarization properties of lidar backscattering from clouds. *Appl. Opt.*, 12(7):1530–1535, Jul 1973.

[17] Kenneth Sassen. Laser depolarisation 'bright band'from melting snowflakes. *Nature*, 255(5506):316–318, 1975.

[18] Kenneth Sassen. Polarization diversity lidar returns from virga and precipitation: Anomalies and the bright band analogy. *Journal of Applied Meteorology and Climatology*, 15(3):292–300, 1976.

[19] Kenneth Sassen. Ice crystal habit discrimination with the optical backscatter depolarization technique. *Journal of Applied Meteorology and Climatology*, 16(4):425–431, 1977.

[20] J. D. Houston and A. I. Carswell. Four-component polarization measurement of lidar atmospheric scattering. *Appl. Opt.*, 17(4):614–620, Feb 1978.

[21] Gary G. Gimmestad. Reexamination of depolarization in lidar measurements. *Appl. Opt.*, 47(21):3795–3802, Jul 2008. doi: 10.1364/AO.47.003795.

[22] Matthew Hayman and Jeffrey P. Thayer. General description of polarization in lidar using stokes vectors and polar decomposition of mueller matrices. *J. Opt. Soc. Am. A*, 29(4):400–409, Apr 2012. doi: 10.1364/JOSAA.29.000400.

[23] M Floc'h, G Le Brun, C Kieleck, J Cariou, and J Lotrian. Polarimetric considerations to optimize lidar detection of immersed targets. *Pure and Applied Optics: Journal of the European Optical Society Part A*, 7(6):1327, nov 1998. doi: 10.1088/0963-9659/7/6/011. URL `https://dx.doi.org/10.1088/0963-9659/7/6/011`.

[24] Jonathan M. Richardson, John C. Aldridge, and Adam B. Milstein. Polarimetric lidar signatures for remote detection of biological warfare agents. In David B. Chenault and Dennis H. Goldstein, editors, *Polarization: Measurement, Analysis, and Remote Sensing VIII*, volume 6972, page 69720E. International Society for Optics and Photonics, SPIE, 2008. doi: 10.1117/12.777833.

[25] Gilles A. Roy, Xiaoying Cao, and Robert Bernier. On linear and circular depolarization LIDAR signatures in remote sensing of bioaerosols: experimental validation of the Mueller matrix for randomly oriented particles. *Optical Engineering*, 50(12):126001, 2011. doi: 10.1117/1.3657505.

[26] Dennis H. Goldstein, David B. Chenault, and J. Larry Pezzaniti. Polarimetric characterization of Spectralon. In Dennis H. Goldstein and David B. Chenault, editors, *Polarization: Measurement, Analysis, and Remote Sensing II*, volume 3754, pages 126 – 136. International Society for Optics and Photonics, SPIE, 1999. doi: 10.1117/12.366323.

[27] Dennis H. Goldstein. Polarimetric characterization of Federal Standard paints. In David B. Chenault, Michael J. Duggin, Walter G. Egan, Dennis H. Goldstein, Walter G. Egan, and Michael J. Duggin, editors, *Polarization Analysis, Measurement, and Remote Sensing III*, volume 4133, pages 112 – 123. International Society for Optics and Photonics, SPIE, 2000. doi: 10.1117/12.406618.

[28] Israel J. Vaughn, Brian G. Hoover, and J. Scott Tyo. Classification using active polarimetry. In David B. Chenault and Dennis H. Goldstein, editors, *Polarization: Measurement, Analysis, and Remote Sensing X*, volume 8364, page 83640S. International Society for Optics and Photonics, SPIE, 2012. doi: 10.1117/12.922623.

[29] Jarrod Brown, Christian Saludez, Darrell Card, and Rodney Roberts. Polarimetric lidar feature selection for material classification. In *2020 IEEE Research and Applications of Photonics in Defense Conference (RAPID)*, pages 1–3, 2020. doi: 10.1109/RAPID49481.2020.9195711.

[30] Richard K. Martin and Christian Keyser. Compact lidar polarimetry via time-varying transmit polarization and an elliptical polarization analyzer. In Monte D. Turner and Gary W. Kamerman, editors, *Laser Radar Technology and Applications XXIV*, volume 11005, page 110050A. International Society for Optics and Photonics, SPIE, 2019. doi: 10.1117/12.2518880.

[31] Christian K. Keyser, Richard K. Martin, P. Khanh Nguyen, and Arielle M. Adams. Single-pulse mueller matrix lidar polarimeter: Modeling and demonstration. *IEEE*

Transactions on Geoscience and Remote Sensing, 57(6):3296–3307, 2019. doi: 10.1109/TGRS.2018.2883242.

[32] Nathaniel J. Field and Joseph A. Shaw. Simple near-monostatic mueller polarimeter. *Appl. Opt.*, 63(28):7540–7546, Oct 2024. doi: 10.1364/AO.538901.

[33] Nicolas Vannier, François Goudail, Corentin Plassart, Matthieu Boffety, Patrick Feneyrou, Luc Leviandier, Frédéric Galland, and Nicolas Bertaux. Comparison of different active polarimetric imaging modes for target detection in outdoor environment. *Appl. Opt.*, 55(11):2881–2891, Apr 2016. doi: 10.1364/AO.55.002881.

[34] USNB of Standards and Fred Edwin Nicodemus. *Geometrical considerations and nomenclature for reflectance*, volume 160. US Department of Commerce, National Bureau of Standards Washington, DC, USA, 1977.

[35] Dennis H. Goldstein and Joseph Lee Cox. Spectropolarimetric properties of vegetation. In Dennis H. Goldstein and David B. Chenault, editors, *Polarization: Measurement, Analysis, and Remote Sensing VI*, volume 5432, pages 53 – 62. International Society for Optics and Photonics, SPIE, 2004. doi: 10.1117/12.546808.

[36] Douglas G. Jones, Dennis H. Goldstein, and Jonathan C. Spaulding. Reflective and polarimetric characteristics of urban materials. In Dennis H. Goldstein and David B. Chenault, editors, *Polarization: Measurement, Analysis, and Remote Sensing VII*, volume 6240, page 62400A. International Society for Optics and Photonics, SPIE, 2006. doi: 10.1117/12.665012.

[37] Vern C Vanderbilt, Lois Grant, and Craig ST Daughtry. Polarization of light scattered by vegetation. *Proceedings of the IEEE*, 73(6):1012–1024, 1985.

[38] Carla Rodríguez, Enrique Garcia-Caurel, Teresa Garnatje, Mireia Serra i Ribas, Jordi Luque, Juan Campos, and Angel Lizana. Polarimetric observables for the enhanced visualization of plant diseases. *Scientific reports*, 12(1):14743, 2022.

[39] Songxin Tan and Ali Haider. A comparative study of polarimetric and non-polarimetric lidar in deciduous-coniferous tree classification. *2010 IEEE International Geoscience and Remote Sensing Symposium*, pages 1178–1181, 2010. doi: 10.1109/IGARSS.2010.5654112.

[40] Guillaume Anna, François Goudail, and Daniel Dolfi. Optimal discrimination of multiple regions with an active polarimetric imager. *Opt. Express*, 19(25):25367–25378, Dec 2011. doi: 10.1364/OE.19.025367.

[41] Clifton G. Scarboro, Colleen J. Doherty, Peter J. Balint-Kurti, and Michael W. Kudenov. Multistatic fiber-based system for measuring the mueller matrix bidirectional reflectance distribution function. *Appl. Opt.*, 61(33):9832–9842, Nov 2022. doi: 10.1364/AO.470608.

[42] Antonello De Martino, Enric Garcia-Caurel, Blandine Laude, and Bernard Drévillon. General methods for optimized design and calibration of mueller polarimeters. *Thin Solid Films*, 455:112–119, 2004.

[43] KM Twietmeyer and RA Chipman. Optimization of mueller matrix polarimeters in the presence of error sources. *Optics Express*, 16(15):11589–11603, 2008.

[44] DS Sabatke, MR Descour, EL Dereniak, WC Sweatt, SA Kemme, and GS Phipps. Optimization of retardance for a complete stokes polarimeter. *Optics Letters*, 25(11): 802–804, 2000.

[45] J Scott Tyo. Design of optimal polarimeters: maximization of signal-to-noise ratio and minimization of systematic error. *Applied optics*, 41(4):619–630, 2002.

[46] Nathaniel J Field. Simple monostatic mueller polarimeter control software, 2024.

[47] Nathaniel J Field. Simple monostatic mueller polarimeter analysis software, 2024.

[48] Nathaniel J Field and Joseph A Shaw. Lambertian surfaces with over-and under-filled field of view. *Proceedings of SPIE*, 12213:46–53, 2022.

[49] Christopher Durell, Dan Scharpf, Greg McKee, Michelle L'Heureux, Georgi Georgiev, Gael Obein, and Catherine Cooksey. Creation and validation of spectralon ptfe brdf targets and standards. *Proceedings of SPIE*, 9639:377–388, 2015.

[50] A Shaw, MG Daly, E Cloutis, G Basic, D Hamilton, K Tait, B Hyde, E Lymer, and K Balachandran. Reflectance properties of grey-scale spectralon® as a function of viewing angle, wavelength, and polarization. *International Journal of Remote Sensing*, 37(11):2510–2523, 2016.

[51] Thomas A Germer. Full four-dimensional and reciprocal mueller matrix bidirectional reflectance distribution function of sintered polytetrafluoroethylene. *Applied optics*, 56 (33):9333–9340, 2017.

APPENDICES

APPENDIX A

ANALYSIS SCRIPT

This work uses the three following MATLAB scripts as the primary method to analyze the measurement data sets from the DMPL.

A.0.1 proc_all_folder_csv.m

This script is run to process the data as saved by the control software in the selected folder. It processes all the data in the folder into Mueller matrices as a function of θ_i and range, such that the output dimensions are (θ_i, R, i, j) for Mueller coefficients m_{ij}.

```
%% DMPL Data Folder Processing Script
% GUI prompts user to pick the folder
fpath = uigetdir();
addpath(fpath);

% Clear old values which might influence dimensionality
clear Nsets idx Npuls OD
clear DirG dG tstmpG datG angG
clear DirI dI tstmpI datI angI

% Input applied ND value if doing sample characterization
od_temp = inputdlg("What OD value was used?");
OD = str2num(od_temp{1});

% Create default structure for each channel's data
DirG = dir(fullfile(fpath,'\*\_w532*.csv'));
DirI = dir(fullfile(fpath,'\*\_w1064*.csv'));

% System Parameters based on using the GaGe CSE161G2
rSmp = 1E9; % Digitizer Sampling Rate, [Hz]
Rbin = 2.99792458E8/(2*rSmp); % Range bin depth, [m]
Nr_max = size(readmatrix(DirG(1).name),2)-2; % Acquired Range
   Depth, []
RR = Rbin*(1:Nr_max)-1.66223; % Range vector

%% Restructure the data struct for the 532 channel
Nsets = length(DirG);
for ii = 1:Nsets
    % Pull the incidence angles from the filenames
    Astr = split(string(DirG(ii).name),["_a","_"]);
    angG(ii) = double(Astr(3));
    % Pull the actual data
    dG(:,:,ii) = readmatrix(DirG(ii).name);
    idx = dG(:,1,ii); % The PSG-PSA stage ID#
```

```
    tstmpG(:,ii) = dG(:,2,ii); % The stage-specific data
       timestamp
    Npuls = length(idx)/length(unique(idx)); % The number of
       pulses taken to be averaged
    for nn = 1:Npuls
        % Rearranging the data to have dimensions (State_ID#,
           Range, Pulse#, Dataset#)
        datG(idx(nn:Npuls:end),:,nn,ii) = dG(nn:Npuls:end,3:end,
           ii);
    end
    % Find all indicies where signal is above the mean (all peaks
       )
    idxSig = find(mean(datG(:,:,:,ii),[1 3])>mean(datG(:,:,:,ii)
       ,"all"));
    % Set an upper limit on detected range, 50 range bins past
       the farthest peak
    idxLim = idxSig(end)+50;
    % Use the data after the last detected peak to generate a
       dark signal for each pulse
    drkG(ii) = mean(datG(:,idxLim:end,:,ii),"all");
    % Subtract the dark signal from the signal voltage data
    datG(:,:,:,ii) = datG(:,:,:,ii) - drkG(ii);
end
% Negative values are not real signal and cause processing errors
   : Set to 0
datG(datG<0) = 0;
% Determine the highest signal in any PS-State along the range
   dimension
dMmG = max(mean(datG,[3 4]),[],1);
% Mask out data where no PS-State signal rises above 1.5x the
   dark signal
datG(:,dMmG<mean(drkG,'all')/2,:,:) = NaN;
% Apply the range-squared correction to the data
datG = datG.*power(RR,2); % Final data units, [V m^2]

%% Apply the same steps as above to restructure the 1064-nm
   channel
Nsets = length(DirI);
for ii = 1:Nsets
    Astr = split(string(DirI(ii).name),["_a","_"]);
    angI(ii) = double(Astr(3));
    dI(:,:,ii) = readmatrix(DirI(ii).name);
    idx   = dI(:,1,ii);
```

```
    tstmpI(:,ii) = dI(:,2,ii);
    Npuls = length(idx)/length(unique(idx));
    for nn = 1:Npuls
        datI(idx(nn:Npuls:end),:,nn,ii) = dI(nn:Npuls:end,3:end,
           ii);
    end
    idxSig = find(mean(datI(:,:,:,ii),[1 3])>mean(datI(:,:,:,ii)
       ,"all"));
    idxLim = idxSig(end)+50;
    drkI(ii) = mean(datI(:,idxLim:end,:,ii),"all");
    datI(:,:,:,ii) = datI(:,:,:,ii) - drkI(ii);
end
datI(datI<0) = 0;
dMmI = max(mean(datI,[3 4]),[],1);
datI(:,dMmI<mean(drkI,'all')/2,:,:) = NaN;
datI = datI.*power(RR,2);

%% Generate Mueller matrices from the processed signal data
% Group and sort the incidence angles considered
aG = sort(unique(angG));
aI = sort(unique(angI));

% Find a MM for each unique incidence angle
for ii = 1:length(aG)
    % Find the Dataset# for each measurement set at a given
       incidence angle
    idNtmp = find(angG == aG(ii));
    % Average the Datasets & Pulses to produce a MM for the
       incidence angle
    MG(ii,:,:,:) = DMPLR(mean(datG(:,:,:,idNtmp),[3 4]),'g',OD,aG
       (ii));
end

% Apply the same steps to the 1064-nm channel as for the 532
   above
for ii = 1:length(aI)
    idNtmp = find(angI == aI(ii));
    MI(ii,:,:,:) = DMPLR(mean(datI(:,:,:,idNtmp),[3 4]),'i',OD,aI
       (ii));
end
```

A.0.2 DMPLR.m

This script is called by `proc_all_folder_csv.m` to generate the Mueller matrices. The called file, `W.csv`, holds the predetermined analysis matrix described as **B** in Eq. 17.

```
%% DMPL Analysis by Linear Algebra
% Takes the input 'dat' (16xNr matrix) and outputs the Mueller
   matrices for
% each set of 16 measurements at each lidar range bin, Nr.
% The output is an (Nr,4,4) Mueller matrix.
function M = DMPLR(dat,g_or_i,ND,ang)
    % the analysis matrix, for states 11,12,13...42,43,44
    W = readmatrix('W.csv');
    % the C2 values for the two channels, in [/sr mV m2], divided
        to [/sr V m2]
    if(matches(g_or_i,'g'))
        C2 = 0.01405E-3;
    elseif(matches(g_or_i,'i'))
        C2 = 0.28143E-3;
    else
        error('Please define if this is the 532-nm channel, ''g''
           , or the 1064-nm channel, ''i''.');
    end

    KK = C2/(power(10,-ND)*cosd(ang));
    % KK = 1;

    Nr_max = size(dat,2);
    Mt = nan([Nr_max 4 4]);
    for Nr = 1:Nr_max
        m = W*dat(:,Nr);
        m_temp = devec(m);
        Mt(Nr,:,:) = m_temp;
    end

    % first, set the m00 coefficient as a BRF value [/sr]
    M(:,1,1) = KK*Mt(:,1,1);
    % then, normalize the remaining coefficients to
    % the associated m00 [no units]
    M(:,1,2) = Mt(:,1,2)./Mt(:,1,1);
        M(:,1,3) = Mt(:,1,3)./Mt(:,1,1);
        M(:,1,4) = Mt(:,1,4)./Mt(:,1,1);
    M(:,2,1) = Mt(:,2,1)./Mt(:,1,1);
        M(:,2,2) = Mt(:,2,2)./Mt(:,1,1);
```

```
        M(:,2,3) = Mt(:,2,3)./Mt(:,1,1);
        M(:,2,4) = Mt(:,2,4)./Mt(:,1,1);
    M(:,3,1) = Mt(:,3,1)./Mt(:,1,1);
        M(:,3,2) = Mt(:,3,2)./Mt(:,1,1);
        M(:,3,3) = Mt(:,3,3)./Mt(:,1,1);
        M(:,3,4) = Mt(:,3,4)./Mt(:,1,1);
    M(:,4,1) = Mt(:,4,1)./Mt(:,1,1);
        M(:,4,2) = Mt(:,4,2)./Mt(:,1,1);
        M(:,4,3) = Mt(:,4,3)./Mt(:,1,1);
        M(:,4,4) = Mt(:,4,4)./Mt(:,1,1);
end

%% Auxillary Functions
function M = devec(A)
    M = [A( 1) A( 2) A( 3) A( 4);
         A( 5) A( 6) A( 7) A( 8);
         A( 9) A(10) A(11) A(12);
         A(13) A(14) A(15) A(16)];
end
```

A.0.3 DMPL_Analysis.m

This script is called in the command window after running `proc_all_folder_csv.m` to plot the data in a predefined 4x4 matrix of plots with auto-scaling and specifically defined colorbars for accessibility.

```
%% DMPL Data Plotting Script
% This function analyzes and returns plots for DMPL
   datDMPL_Structure.
% The output is a structure containing all the analysis info.

function DMPL_Structure = DMPL_Analysis(MM,RR,ANG,g_or_i)
    if(matches(g_or_i,'g'))
        cN = 5; % Green line for 532-nm
    elseif(matches(g_or_i,'i'))
        cN = 2; % Red line for 1064-nm
    else
        error('Please define if this is the 532-nm channel, ''g''
           , or the 1064-nm channel, ''i''.');
    end
    %% Global Plot Limits - Editable
    % BRDF magnitude limit
    blim = max(MM(:,:,1,1),[],'all'); % Default auto-sizing
    % Mueller coefficient magnitude limit (default: 1)
```

```
    mlim = 1;

    %% Autoscaling (range & incidence angle)
    rrg = RR(~isnan(max(MM(1,:,1,1),[],1)));
    thR = max(ANG)-min(ANG); thV = 10;
    thl = thV*ceil(min(ANG)/thV);
    thu = thV*ceil(max(ANG)/thV);

    %% Define Top-Level Figure Structure
    DMPL_Structure.fig = figure();
    DMPL_Structure.tlo = tiledlayout(4,4);
    DMPL_Structure.tlo.TileSpacing = 'compact';
    DMPL_Structure.plt = gobjects(1,16);

    if(length(ANG) == 1)
%% 2-Dimensional Plots for single angles or complex scenes
        % Define range plot limits
        rl  = min(rrg); ru  = max(rrg);
        rL = floor(rl); rU = ceil(ru); rt = (rU-rL)/4;
        % Plot line colors, choosing the green or red option
        lns = lines();
        DMPL_Structure.clr = lns(cN,:);
        % Mueller matrix plot limits
        ml = -1.1*mlim; mu = 1.1*mlim;
        mT = max([round(mlim,1) 0.1]); mt = round(mT/2,2);
        % BRDF plot limits
        bu = 1.1*blim; bT = round(blim,2); bt = round(blim/4,2);

        % Plot BRDF in place of the m00 coefficient
        DMPL_Structure.ax(1) = nexttile(DMPL_Structure.tlo);
        DMPL_Structure.plt(1) = plot(DMPL_Structure.ax(1),...
            RR,MM(1,:,1,1),'Color',DMPL_Structure.clr,...
            'LineWidth',3); grid on;
        % Check if there's a single sample peak or multiple
        if(mean(diff(find(~isnan(MM(1,:,1,1)))),'all')<=1.05)
            title('BRDF, [sr^{-1}]'); % Single sample =
               characterization
        else
            title('Signal Strength, [arb. units]'); % Multi-
               Sample != characterization
        end
        ylim([0 bu]); yticks(0:bt:bT);
        xlim([rL rU]); xticks(rL:rt:rU); xticklabels('');
```

```
        DMPL_Structure.ax(1).FontSize = 16;

        % Plot the remaining MM coefficients
        for ii = 2:16
            % Determine the Mueller coefficients in order
            jj = 1+floor((ii-1)/4); kk = rem(ii,4); kk(kk==0) =
               4;
            DMPL_Structure.ax(ii) = nexttile(DMPL_Structure.tlo);
            DMPL_Structure.plt(ii) = plot(DMPL_Structure.ax(ii),
               ...
                RR,MM(1,:,jj,kk),'Color',DMPL_Structure.clr,...
                'LineWidth',3); grid on;
            title(sprintf('m_{%i%i}',jj-1,kk-1));
            ylim([ml mu]); yticks(sort(unique([-mT:mt:mT 0])));
            xlim([rL rU]); xticks(rL:rt:rU);
            if(jj~=4 || kk~=1)
                xticklabels('');
                yticklabels('');
            end
            DMPL_Structure.ax(ii).FontSize = 16;
        end
        set(DMPL_Structure.ax(1:16),'Color',[0.95 0.95 0.95]);
        xlabel(DMPL_Structure.tlo,'Range, Z_R, [m]','FontWeight',
           'bold','FontSize',20);
    else
%% 3-Dimensional Plots for multiple angles
        % Loads a preset brightness/heat colormap
        map = load('surfPlotMaps.mat');
        % Generate meshgrid for plotting
        [ZR,TH] = meshgrid(RR,ANG);
        % Ranging plot bounds
        rl  = max([0.92*min(rrg) 0]); ru  = 1.1*max(rrg);
        rL  = round(rl); rU = round(ru,1); rt = round((rU-rL)/4);
        ru00 = rl + .7775*(ru-rl);
        % Incidence angle plot bounds
        thL = round(thl); thU = round(thu); tht = round((thU-thL)
           /4);

        % Plot BRDF in place of the m00 coefficient
        % NOTE: Varied incidence angle is assumed to be used
           solely for
        % characterization purposes, so it always plots BRDF here
           .
```

```
DMPL_Structure.ax(1) = nexttile(DMPL_Structure.tlo);
DMPL_Structure.plt(1) = surf(DMPL_Structure.ax(1),...
    ZR,TH,MM(:,:,1,1),MM(:,:,1,1),'edgecolor','none');
grid on; alpha 1.0; view(2);
title('BRDF, [sr^{-1}]');
xlim([rl ru]); xticks(rL:rt:rU); xticklabels('');
ylim([thl thu]); yticks(thL:tht:thU); yticklabels('');
DMPL_Structure.ax(1).FontSize = 16;

% Plot the remaining MM coefficients
for ii = 2:16
    jj = 1+floor((ii-1)/4); kk = rem(ii,4); kk(kk==0) =
       4;
    DMPL_Structure.ax(ii) = nexttile(DMPL_Structure.tlo);
    DMPL_Structure.plt(ii) = surf(DMPL_Structure.ax(ii),
       ...
        ZR,TH,MM(:,:,jj,kk),MM(:,:,jj,kk),'edgecolor','
           none');
    grid on; alpha 1.0; view(2);
    title(sprintf('m_{%i%i}',jj-1,kk-1));
    xlim([rl ru]);   xticks(rL:rt:rU);
    ylim([thl thu]); yticks(thL:tht:thU);
    if(jj~=4 || kk~=1)
        xticklabels('');
        yticklabels('');
    end
    DMPL_Structure.ax(ii).FontSize = 16;
end
% Set the colormap and colorbar for the BRDF\m00 plot
set(DMPL_Structure.ax(1),'Colormap',map.BRFmap,'CLim',[0
   blim]);
DMPL_Structure.cbh00 = colorbar(DMPL_Structure.ax(1),'
   east','FontSize',14);
% Set the colormap and colorbar for the MM coeff. plots
set(DMPL_Structure.ax(2:16),'Colormap',map.MMCmap,'CLim'
   ,[-mlim mlim]);
DMPL_Structure.cbh = colorbar(DMPL_Structure.ax(16),'
   FontSize',16);
DMPL_Structure.cbh.Layout.Tile = 'east';
% Set plot box background color and the axes labels
set(DMPL_Structure.ax(1:16),'Color',[0.95 0.95 0.95],'Box
   ','on');
ylabel(DMPL_Structure.tlo,strcat(['Angle, \theta_i, ['
```

```
            char(176) ']']),'FontWeight','bold','FontSize',20);
        xlabel(DMPL_Structure.tlo,'Range, Z_R, [m]','FontWeight',
            'bold','FontSize',20);
    end
    % Establish a default sgtitle for setting defaulting
    sgtitle('Title','FontWeight','bold','FontSize',24);
end
```

APPENDIX B

CONTROL SOFTWARE ARCHITECTURE

These diagrams show the control software architecture for the DMPL, as programmed in LabView. These only include the two programs which I generated or heavily altered, though they also rely on multiple sub-vis from GaGe and Thorlabs which are entirely unedited.

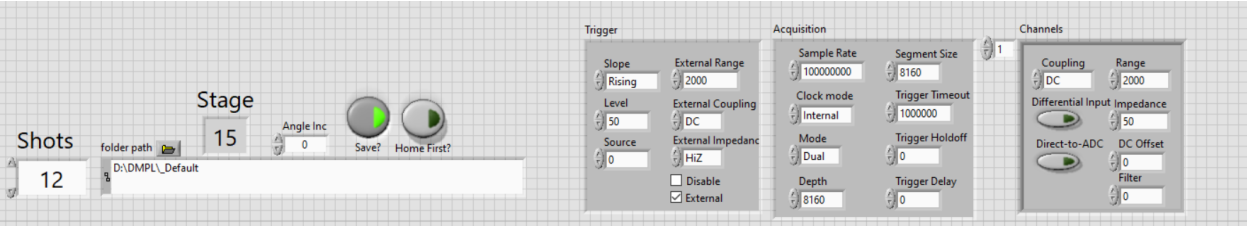


Figure 32: The front panel for the DMPL control software. The default number of average shots is 12. Other default channel and sampling rate options are set and not regularly changed.

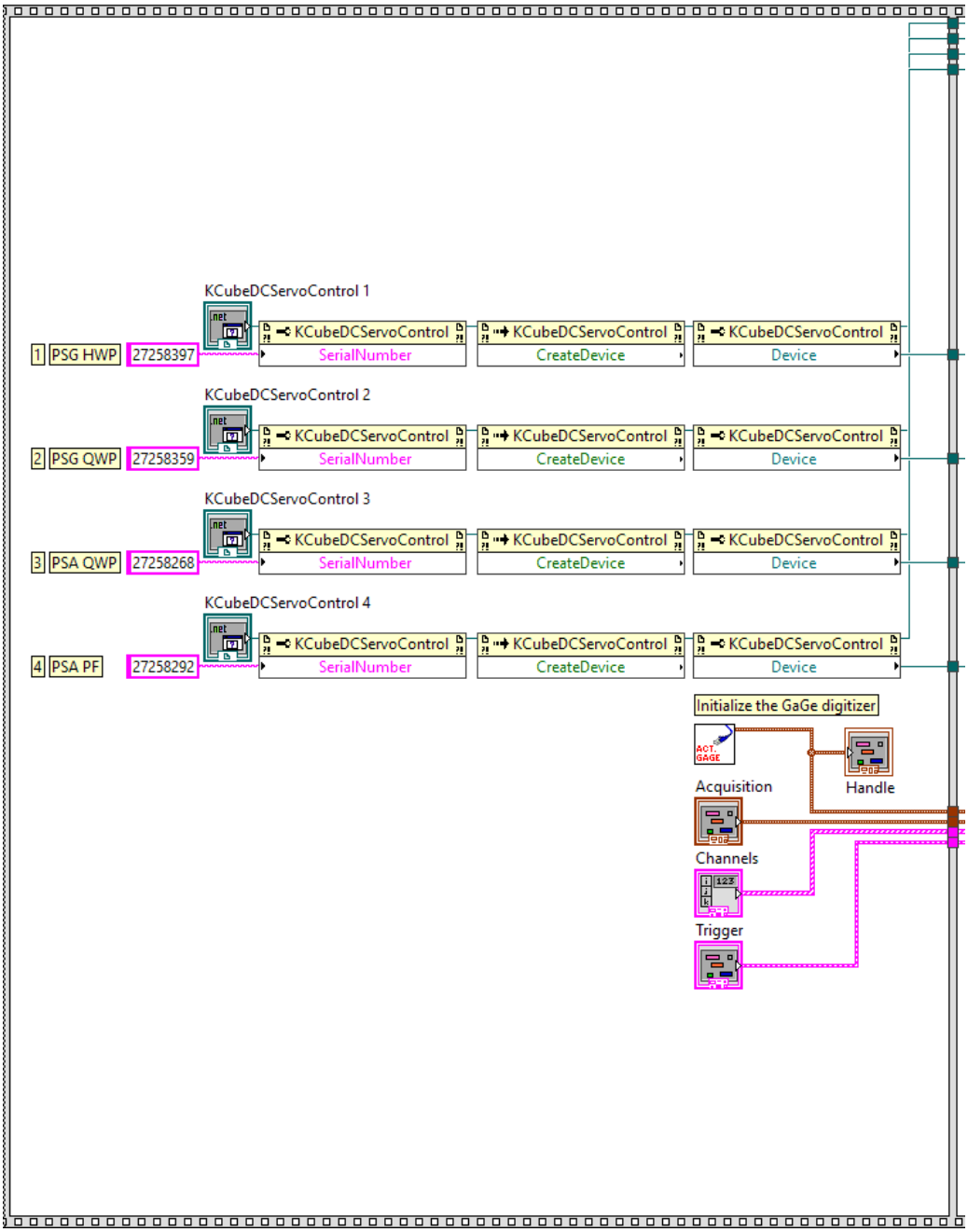


Figure 33: The first third of the DMPL control software block diagram. This section initializes the rotation controllers and the digitizer.

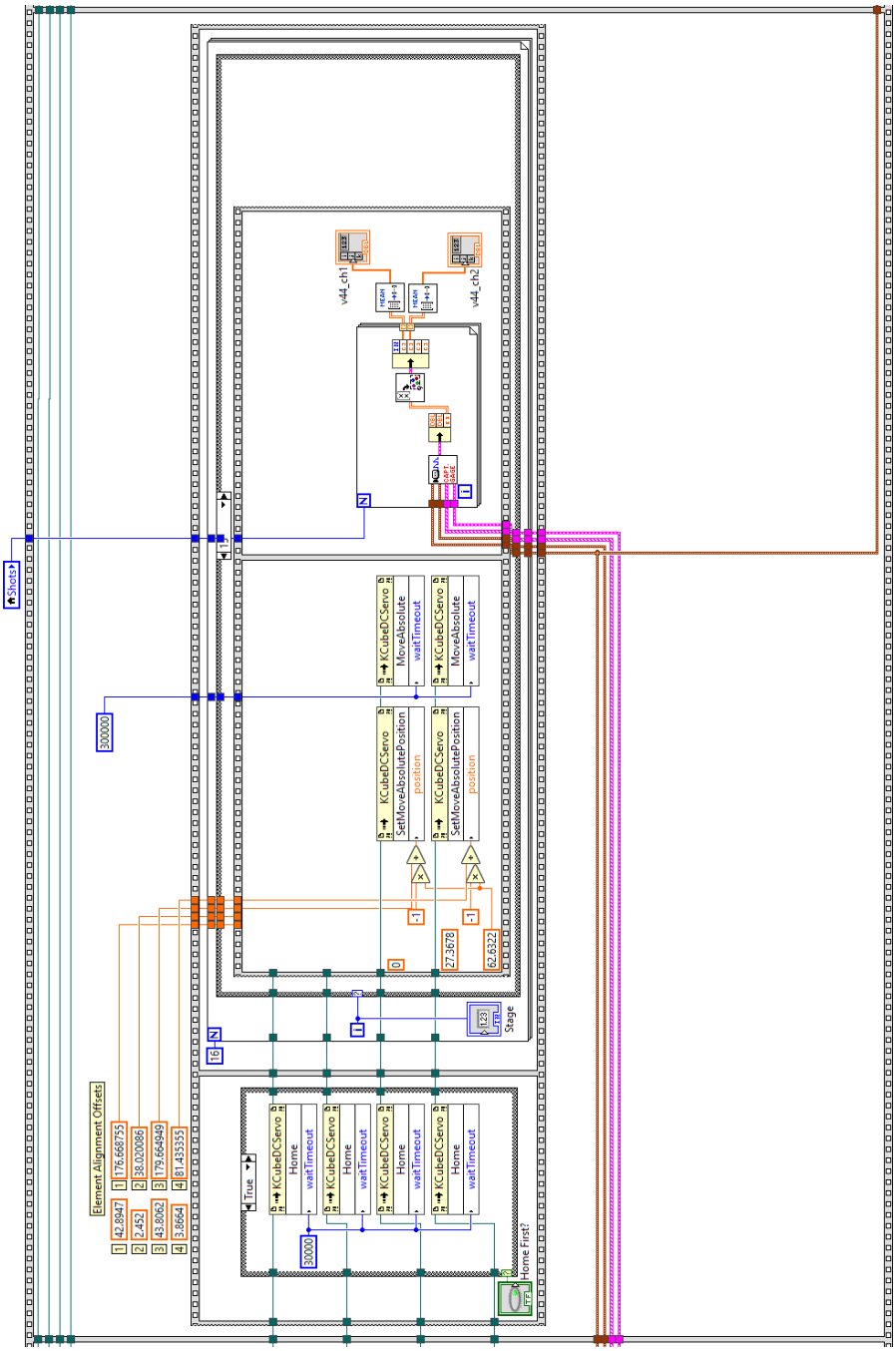


Figure 34: The middle third of the DMPL control software block diagram. This section loops through the rotation values for each of the PSG and PSA states and captures the lidar returns for each state combination. If the rotation mounts need to be homed, that is performed in this section as well.

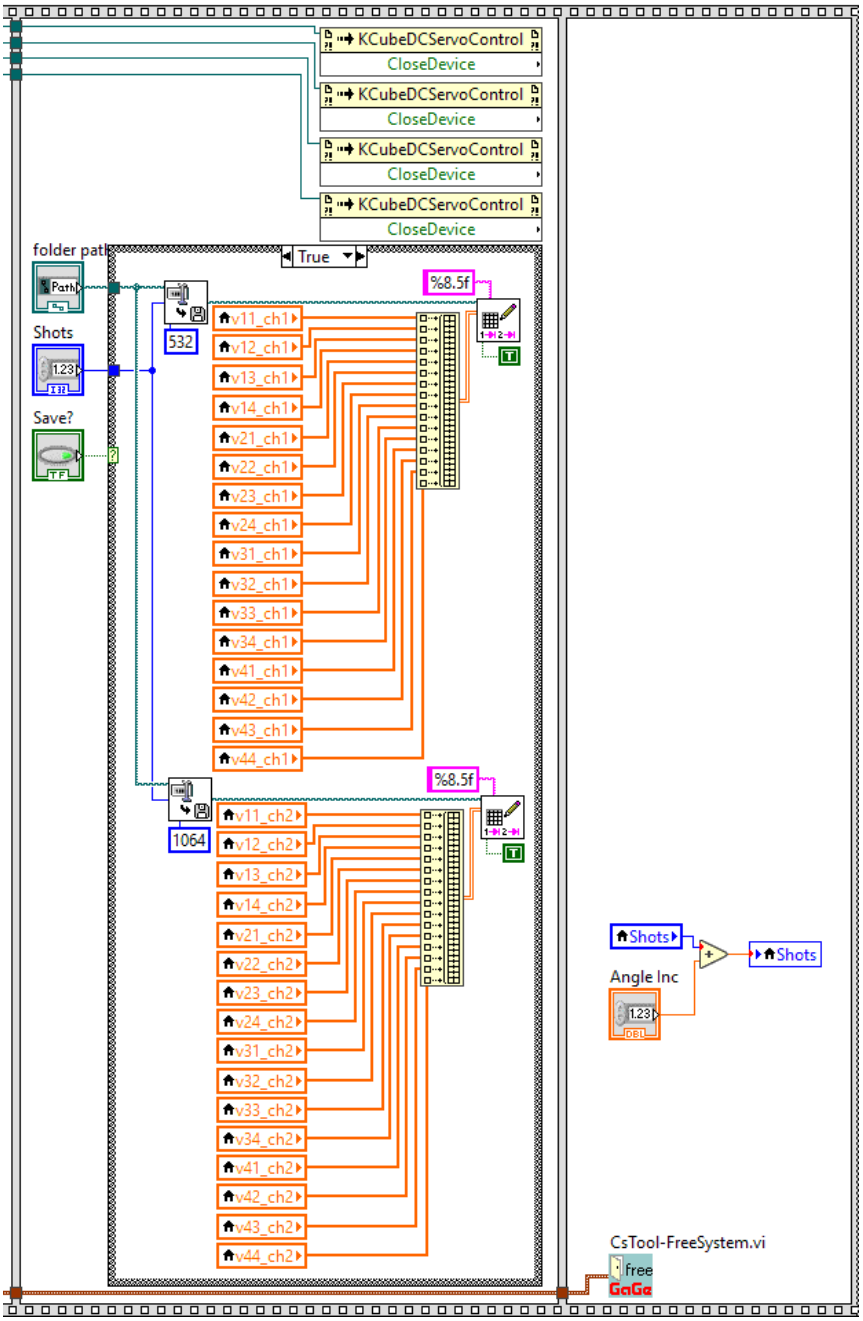


Figure 35: The last third of the DMPL control software block diagram. This section generates the save files and saves them to the selected file path. It also releases control of the rotation mounts to avoid issues in continuous runs.

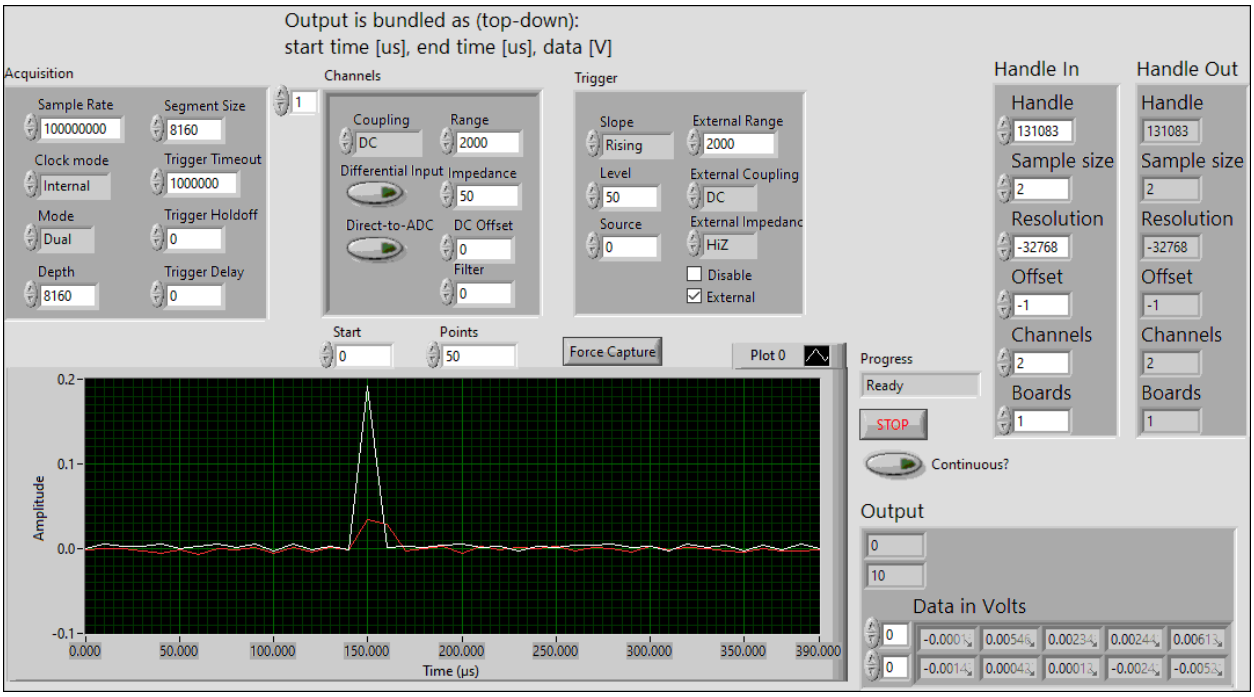


Figure 36: The front panel for the lidar shot capture code, visually modified from the original GaGe capture software.

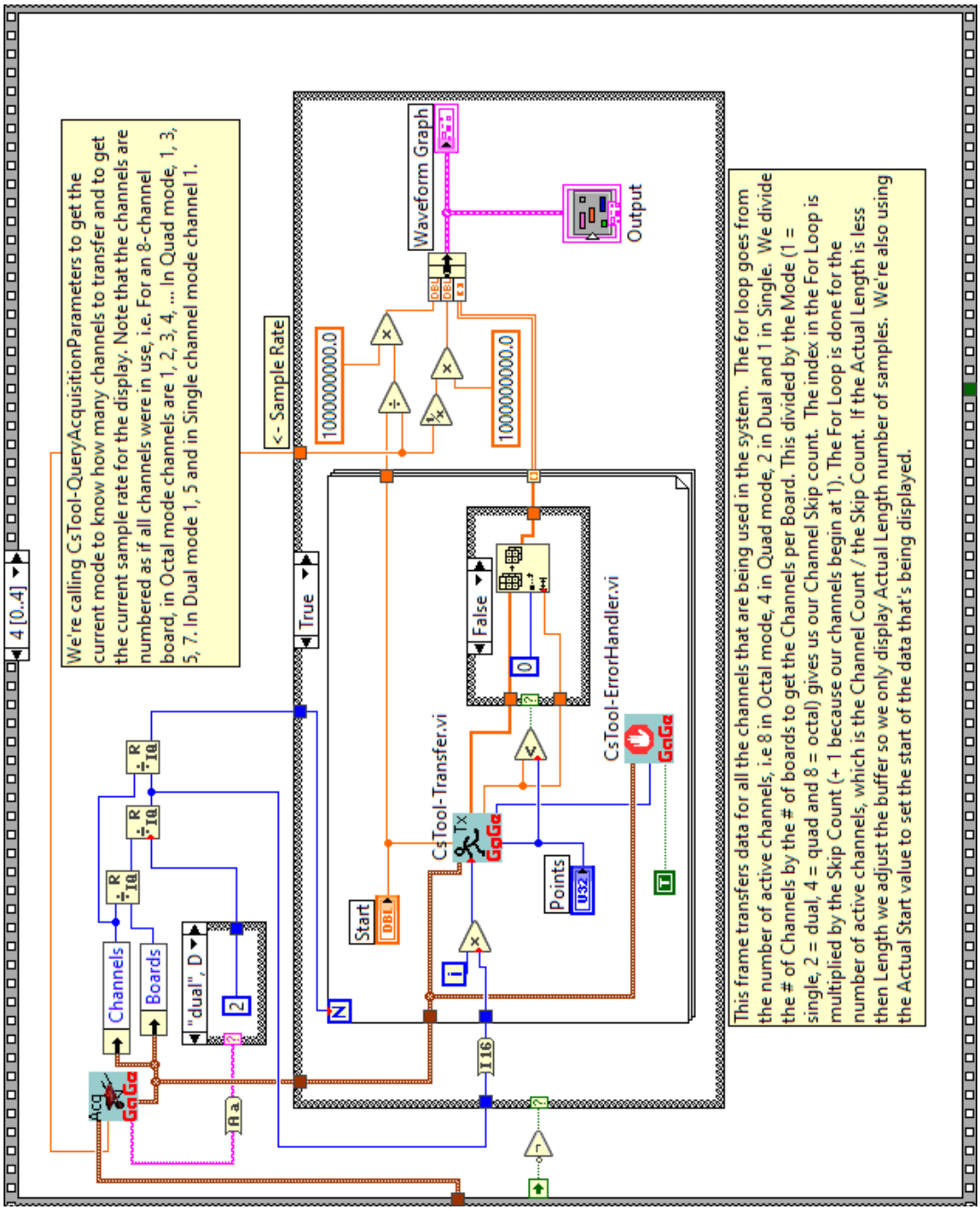


Figure 37: The actual capture procedure from the GaGe capture software used to collect the lidar returns. This section of the code was modified significantly to change the structure of the outputs to be more usable in the primary DMPL control software.

APPENDIX C

PHOTOMETRIC CALCULATIONS

For the DMPL system, the following are the rough radiometric calculations to ensure that SNR is reasonable and the detectors will not saturate (which will also ensure damage thresholds are not reached). These values are for the Quantel ULTRA laser and the Thorlabs APD430C and APD430A detectors.

The transmitter uses a Quantel ULTRA laser, which is a Q-switched laser with measured 34.6 mJ pulse energy at 532-nm wavelength and 14.6 mJ pulse energy at 1064-nm wavelength. Given these pulse energy values and the beam diameter and divergence, we were able to calculate signal-to-noise ratios (SNRs) and saturation potential of a number of viewing geometries and sample parameters. These values were determined from basic radiometry equations expanded for received photon flux, Φ_{Rx}, instead of the typical received optical power, P_{Rx}, briefly summarized for a given wavelength, λ, as

$$\Phi_{Rx}^{\lambda} = \rho_t T_{atm}^2 L_{ph}^{\lambda} A_{Rx} \Omega_{FOV}, \tag{54}$$

where ρ_t is the sample reflectance, T_{atm} is the integrated atmospheric transmittance along the path, L_{ph} is the photon radiance from the sample $[\frac{photons}{pulse*m^2*sr}]$, A_{Rx} is the area of the receiver entrance pupil $[m^2]$, and Ω_{FOV} is the projected solid angle between the sample and receiver $[sr]$ (assuming an overfilled FOV). For a given APD, we can pull from the datasheet the noise-equivalent number of photons over the sensor integration period, NEN_{ph}^{λ}, and the saturating number of photons over the sensor integration period, N_{sat}^{λ}. These specifications are used to ensure the setup is not wildly outside the range of saturation, and an estimation of the expected SNR for a given setup and wavelength as

$$SNR_{\lambda} = \Phi_{Rx}^{\lambda} / NEN_{ph}^{\lambda}. \tag{55}$$

Received Photons, $\Phi_{Rx}^{\lambda}[\frac{ph}{p}]$: Since we're dealing with a pulse of light, we'll calculate based on the number of photons received per pulse. This follows from Eq. 54. Assuming the following values,

$$\rho_{t,hi} = 0.99 \tag{56}$$

$$\rho_{t,lo} = 0.10 \tag{57}$$

$$T_{atm} = 0.9 \tag{58}$$

$$A_{Rx} = \frac{\pi}{4}(0.0254)^2 \approx 2.03 * 10^{-3}[m^2] \tag{59}$$

$$\Omega_{FOV} = 4\pi sin^2(\frac{\theta_{FOV}}{2}) \approx 7.85 * 10^{-5}[sr] \tag{60}$$

we find the high and low values for received photons to be

$$\Phi_{Rx,hi}^{\lambda} = L_{ph,hi}(3.19 * 10^{-8}) \tag{61}$$

$$\Phi_{Rx,lo}^{\lambda} = L_{ph,lo}(3.22 * 10^{-9}) \tag{62}$$

Photon Radiance, $L_{ph}^{\lambda}[\frac{ph}{p*m^2*sr}]$: The number of photons radiated from the target.

For the purpose of these calculations, we will assume a Lambertian reflector. Assuming the following values,

$$Z_t = 10[m] \tag{63}$$

$$\theta_{div} = 5[mrad] \tag{64}$$

$$A_{illuminated} \approx \frac{\pi}{4}(Z_t tan(\theta_{div}))^2 \approx 0.0020[m^2] \tag{65}$$

$$\mathcal{E}_{532} = 34.6[mJ], \mathcal{E}_{1064} = 14.6[mJ] \tag{66}$$

$$N_{ph}^{532} = \mathcal{E}_{532}(532 * 10^{-9})/hc \approx 9.269 * 10^{16}[ph] \tag{67}$$

$$N_{ph}^{1064} = \mathcal{E}_{1064}(1.064 * 10^{-6})/hc \approx 7.823 * 10^{16}[ph] \tag{68}$$

we find the photon radiance values at each wavelength per pulse to be

$$L_{ph}^{532} \approx 1.503 * 10^{19}[\frac{ph}{p * m^2 * sr}] \tag{69}$$

$$L_{ph}^{1064} \approx 1.268 * 10^{19}[\frac{ph}{p * m^2 * sr}] \tag{70}$$

From these photon radiance values, we get the following received photon values per pulse at the DMPL detectors.

$$\Phi_{Rx,hi}^{532} \approx 4.79 * 10^{11}[\frac{ph}{p}] \tag{71}$$

$$\Phi_{Rx,lo}^{532} \approx 4.84 * 10^{10}[\frac{ph}{p}] \tag{72}$$

$$\Phi_{Rx,hi}^{1064} \approx 4.04 * 10^{11}[\frac{ph}{p}] \tag{73}$$

$$\Phi_{Rx,lo}^{1064} \approx 4.08 * 10^{10}[\frac{ph}{p}] \tag{74}$$

To approximate SNR, we can pull the noise-equivalent power, NEP^{λ}, for the detectors, translate them to noise-equivalent photon flux, $NE\Phi^{\lambda}$, and then divide the received photon flux by this noise equivalence. Note that the flux values above are in $[ph/pulse]$, so we need to divide the Φ_{Rx} values by 6.86 $[ns/pulse]$ to get into properly comparable units of $[ph/s]$.

$$NE\Phi^{\lambda} = \frac{NEP^{\lambda}\lambda}{hc} \tag{75}$$

$$NE\Phi^{532} = \frac{(5.5\ nW)(532\ nm)}{hc} \approx 1.473 * 10^{10} \tag{76}$$

$$NE\Phi^{1064} = \frac{(17\ nW)(1064\ nm)}{hc} \approx 9.108 * 10^{10} \tag{77}$$

$$SNR_{lo}^{532} = \frac{\Phi_{Rx,lo}^{532}}{(6.86\ ns)NE\Phi^{532}} = 4.79 * 10^8 \approx 173.6[dB] \tag{78}$$

$$SNR_{lo}^{1064} = \frac{\Phi_{Rx,lo}^{1064}}{(6.86\ ns)NE\Phi^{1064}} = 6.53 * 10^7 \approx 156.3[dB] \tag{79}$$

This supports the detectors' ability to receive sufficient signal for our lower-bounding case.

We can similarly determine the saturation photon flux numbers, Φ_{sat}^{λ}, for the detectors based on their CW saturation power specs, a $\sqrt{\frac{1\ ms}{6.86\ ns}} \approx 381.8$ magnification due to being pulsed, and a safety factor of 2.

$$\Phi_{sat}^{\lambda} = \frac{2 * 381.8 * P_{sat}^{\lambda}\lambda}{hc} \tag{80}$$

$$\Phi_{sat}^{532} = 1.64 * 10^{16}[\frac{ph}{s}] = 1.12 * 10^8[\frac{ph}{p}] \tag{81}$$

$$\Phi_{sat}^{1064} = 9.00 * 10^{16}[\frac{ph}{s}] = 6.17 * 10^8[\frac{ph}{p}] \tag{82}$$

Our high-reflectance cases exceed the saturation photon flux by about three orders of magnitude, but we can simply apply neutral density (ND) filters of optical density about 3.0 to remedy this situation.

APPENDIX D

DMPL OPERATING PROCEDURE

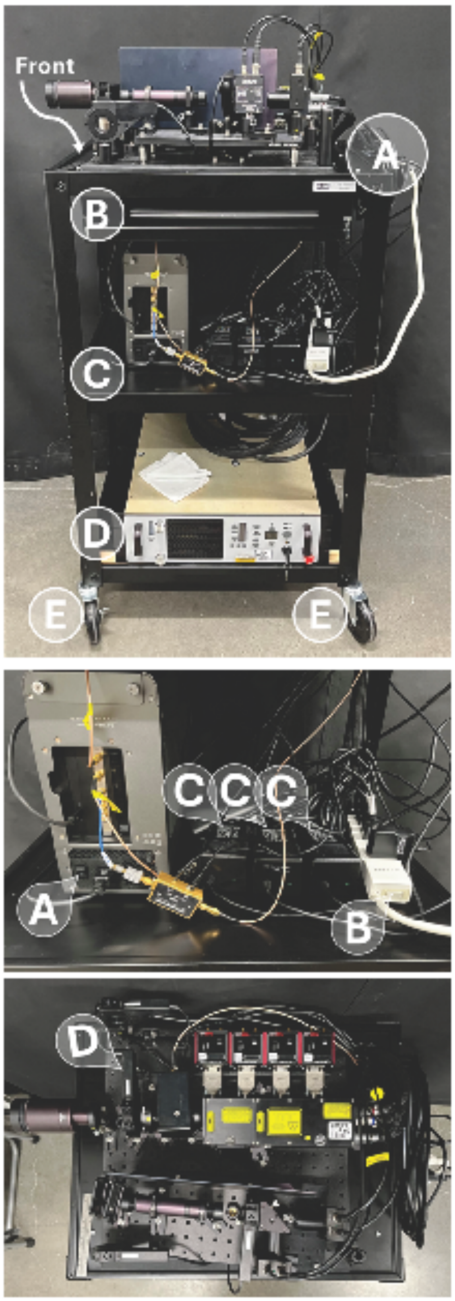
This appendix shows the exact page layouts of the basic DMPL operating procedure which is kept with the instrument.

DMPL Operating Procedure **v1.0**

Last Revision: 11 Dec 2024 (NJ Field)

Dichroic Mueller Pulsed Lidar (DMPL) testbed uses a Class IV pulsed laser operating at both 532-nm (green) and 1064-nm (infrared).

The lidar and its equipment are stored on a rolling cart, as shown in the figure to the right. The lidar sits on the top shelf pointing forward. The power cables are stored behind the top shelf at (A). The laptop is stored under the top shelf on a roll-out tray at (B). The digitizer and the detector power supplies are on the middle shelf, (C). The laser controller is stored on the bottom shelf, (D), because it is the heaviest item and holds water. The two wheels on the facing side of the cart, (E), lock to set a more stable physical position while taking measurements.



Setup: To prepare the DMPL for operation:

1. Plug in the laser controller and cart power. Both cables at (A) need wall power.
2. Point the laser and lock the cart position. Make sure the laser is pointed in a safe direction and mostly aligned to the scene of interest, then lock the wheels of the cart.
3. Turn on the laser controller. Turn the key on the front of the laser controller.
4. Enable the Q-Switch. Wait until the 'Fault' light turns off, then press the 'Q-Switch' button on the laser controller front panel.
5. Turn on the laptop. Sign into the ORSL lab user account using the normal password.
6. Turn on the digitizer. Labelled as {A} in the lower images, the blue ring should light up on the other side.
7. Turn on the power strip. Labelled {B}, gives power to the detectors and trigger amplifier.
   a. Turn on power supplies. If the lights on the power supply boxes aren't green, flip on their switches on the back of the boxes labelled {C}.
8. Turn on the rotation controllers. Labelled {D}, they are on the breadboard on the top shelf.

9. Open the DMPL control software. Open Labview. Select the "Mueller Lidar Control" project. Open "dmpl_meas_PmBRDF.vi".
10. Home and set the rotation controllers. Open and run "homeMultiple.vi". The default parameter values should be correct to home and set both the rotation stages to horizontal linear states. If the rotation controllers were left on, you can skip this step.
11. Open the plot reference. From the LabView project, open "gage_capture.vi" and move it so the plot is visible when "dmpl_meas_PmBRDF.vi" is the active window.

Data Collection: Once DMPL is set up, follow this procedure for data collection.

1. Select the appropriate file destination. This should typically be pointed to the default location in a sub-folder for the scene being collected.
2. Fire the laser. Ensure the hazard zone is clear. Ensure the beam-block is opened. Press the "Fire" button on the laser controller.
3. Run the control software. In "dmpl_meas_PmBRDF.vi", select Run.
   a. Ensure non-saturating returns. While the first data-set is collected, watch the plot window in "gage_capture.vi" to ensure the returns are not saturating the detectors. If the returns are saturating, replace a square ND filter with a stronger filter, delete the saturated data and repeat this step.
4. Run Continuous. In "dmpl_meas_PmBRDF.vi", select Run Continuous. Allow data to collect until you have taken a few samples for the scene.
   a. Single Sample P-mBRDF Characterization: If collecting data for a single sample, you will instead put the sample rotation value into the "Angle Increment" variable on the front panel and Run one at a time, rotating the sample between each collection.

Shutdown: Once the data collection is complete, follow this procedure to shutdown the DMPL.

1. Stop the Laser. Select the "Fire" button on the laser controller to stop firing.
2. Close LabView. Close all LabView windows. After closing the project, you will be prompted with another top-level window to close.
3. Shut down equipment in reverse order.
   a. Turn off the rotation controllers. Labelled {D}, located on the breadboard on the top shelf.
   b. Turn off the power strip. Labelled {B}, this switches off the detector and trigger amplifier power. *Note: The trigger power supply green light may stay lit for up to a minute as power dissipates. You do not need to wait for it to fully go out, but do wait until it's at least mostly dimmed before moving on (usually about 5 seconds).*
   c. Turn off the digitizer. Labelled {A}, the blue light on the other side should turn off.
4. Turn off the laser controller. Check to see if the laser head is still warm or if it has cooled reasonably. This usually just takes a couple minutes after the laser has stopped firing, which is typically just the time to turn everything else off and make sure data are saved to the right spot. If the laser is cool enough, turn the key on the front of the laser controller to turn it all the way off.